Fall 12-15-2010

Photoionization of the Potassium Isoelectronic Sequence: Ca+ and Transition Metal Ions

ayao m. sossah

PHOTOIONIZATION OF THE POTASSIUM ISOELECTRONIC SEQUENCE: Ca^+ AND TRANSITION METAL IONS

by

AYAO MAMERT SOSSAH

Under the Direction of Steven T. Manson

ABSTRACT

Photoionization cross section calculations are performed for the ground ($[Ne]3s^2 3p^6 3d\ ^2D^e_{3/2}$) and the first two excited ($[Ne]3s^2 3p^6 3d\ ^2D^e_{5/2}$ and $[Ne]3s^2 3p^6 4s\ ^2S^e_{1/2}$) states of potassium-like transition metal ions (Sc^{+2}, Ti^{+3}, V^{+4}, Cr^{+5}, Mn^{+6}, Fe^{+7}), along with photoionization calculations for K-like Ca^+ ions in the ground ($[Ne]3s^2 3p^6 4s\ ^2S^e_{1/2}$) state and the first two excited ($[Ne]3s^2 3p^6 3d\ ^2D^e_{3/2}$ and $[Ne]3s^2 3p^6 3d\ ^2D^e_{5/2}$) states. The discrete N-electron final state ion system orbitals are generated using the computer program AUTOSTRUCTURE; 24 configurations are included in the configuration-interaction (CI) calculation for transition metal ions, and 30 configurations for the case of Ca^+ ions. The initial and final (N+1)-electron wavefunctions are generated using *R*-matrix along with photoionization cross sections. In addition to the non-relativistic (LS-

coupling) *R*-matrix, we have used the relativistic (Breit-Pauli) *R* -matrix method to carry out these calculations to focus on relativistic effects. Relativistic and non-relativistic results are compared to demonstrate the influence of relativistic effects. The prominent $3p \rightarrow 3d$ giant resonances are analyzed and identified, and our calculated positions and widths are compared with experimental results for K-like ions such as Ca^{+}, Sc^{+2} and Ti^{+3}. In the case of lower Z ($22 \geq Z \geq 20$) ions (Ca^{+}, Sc^{+2} and Ti^{+3}), the photoionization cross section spectra are dominated by the giant ($3p \rightarrow 3d$ excitation) resonances, while in cases of higher Z ($26 \geq Z \geq 23$) ions (V^{+4}, Cr^{+5}, Mn^{+6} and Fe^{+7}), the $3p \rightarrow 3d$ resonances lie below the ionization threshold, and the cross sections are dominated by $3p^5 3d\,nd$ and $3p^5 3d\,n's$ Rydberg series of resonances. Comparison of the Ca^{+}, Sc^{+2} and Ti^{3+} results with available theoretical and experimental data shows good agreement.

INDEX WORDS: Photoionization, Cross section, Potassium-like ions, Resonance, *R*-matrix, Ca^{+}, Sc^{+2}, Ti^{+3}, V^{+4}, Cr^{+5}, Mn^{+6}, Fe^{+7}, Transition metal ions, 3*d* electron atoms and ions, AUTOSTRUCTURE, SUPERSTRUCTURE, Breit-Pauli, open *d*-shell, 3*d*-subshell atoms, 3*d*-subshell ions

PHOTOIONIZATION OF THE POTASSIUM ISOELECTRONIC SEQUENCE: Ca^+ AND TRANSITION METAL IONS

by

AYAO MAMERT SOSSAH

A Dissertation Submitted in Partial Fulfillment of the Requirements for the Degree of

Doctorate of Philosophy

in the College of Arts and Sciences

Georgia State University

2010

PHOTOIONIZATION OF THE POTASSIUM ISOELECTRONIC SEQUENCE: Ca^+ AND TRANSITION METAL IONS

by

AYAO MAMERT SOSSAH

Committee Chair: Steven T. Manson

Committee: Daniel M. Crenshaw
Xiaochun He
Mark Stockman
Brian Thoms

Electronic Version approved:

Office of Graduate Studies

College of Arts and Sciences

Georgia State University

December 2010

DEDICATION

This work is dedicated in general to all the people in the world with disabilities, and in particular to students with visual impairments.

ACKNOWLEDGEMENTS

I would like to thank A. Hibbert (Queen's University of Belfast, UK) for assistance and discussions on K-like ions target orbitals wavefunction, and I also want to express my gratitude to N. R. Badnell (University of Strathclyde, Glasgow, UK) for making available, on his very comprehensive website, all the codes on *R*-matrix used in this work. I would also like to thank A. Müller, R. Phaneuf and S. Schippers for supplying their data, on Sc^{+2} and Ti^{+3},in numerical form and for numerous discussions. The calculations were performed using the computational facilities at the National Energy Research Scientific Computing Center (NERSC).

I am grateful to my former and current research group members (Chieh-Jen Yang, Wei-Chun Chu, Prahba Padukka and Mohammed Javani) for our precious and helpful discussions on research and graduate course works. I would like to thank Dr. Hsiao-Ling Zhou for guidance and advices on running *R*-matrix codes and our numerous and fructuous discussion on different research topics. I deeply appreciate the graduate director, Dr. Unil Perera, advices and suggestions on academic and research issues, and I would like to express my gratitude to my graduate committee members (Dr. Daniel M. Crenshaw, Dr. Xiaochun He, Dr. Mark Stockman and Dr. Brian Thoms) for their helpful comments and suggestions. I deeply am thankful to my advisor, Dr. Steven T. Manson, for being patient with me and teaching me for all those years in the theoretical atomic physics research group; I really appreciate, and learned from all our discussions on various and different topics that reach far beyond physics, and have contributed to culturally enrich me and widen my horizons in terms of knowledge of the world.

I am taking this opportunity to express my gratitude to the students support service (SSS) and the Margaret A. Staton office of disability service (ODS) at Georgia State University for their material and financial supports; as a physics graduate student, I have been a frequent user of equipments (computer and CCTV) at SSS and ODS. I would like to thank the CVI in Atlanta (Georgia) for providing me with training that has been very helpful and useful as a student, and for making me understand that no dream is out of reach as long as one is determined, and ready to work hard to achieve it. I want to thank my friends and family members who have been always there for me, and have supported me in everything I have been involved in; among them are: Paul K. Agboati, Vincent K. Agboto, Edgard K. Maboudou, Armand K Dagawa, Nicole G. Dagawa, Gisele Dagawa Anato, Carlos Sarsadias, Violeta Sarsadias, Janina Archie, Anna Lonzanida, Caredad A. Grant, Faridah Sossah, Camille Djiyehoue, Francis Quashie and Abavi Assaba Alowoanou. Finally I want to thank my wife Maria Isabel Sossah for her support and for being patient with me throughout all those years at physics graduate school.

TABLE OF CONTENTS

LIST OF TABLES

LIST OF FIGURES

CHAPTER 1.

INTRODUCTION

Open-shell atoms represent more than 70% of the total number of elements in the atomic periodic table, but atomic data involving the dynamics of open-shell atoms and their ions are far fewer than their proportion in the periodic table. This lack of data is mainly due to the serious challenge that both theorists and experimentalist have faced while working on open-shell atoms. Considering the whole group of open-shells atoms, open *d*- and *f*-subshell atoms and ions have drawn much less attention so far compared to open *s*- and *p*-subshell atoms. However, during the last few decades, the advent of third generation synchrotron radiation sources [1] and the extremely rapid development of computational power have produced significant advances in the investigation of dynamical atomic processes, and open *d*- and *f*-subshell atoms and ions have been subject to increasing interest both theoretically and experimentally. Among the dynamical process of interest is the response of these atoms and ions to ionizing radiation, the photoionization process, which is of interest as a fundamental process of nature, along with applications to a number of areas of science and technology, most notably the modeling of plasmas, astrophysical and otherwise.

In this work we report on the first stage of a study of the photoionization of the 3*d*-electron atoms and ions (transition metals and Ca^+ ions). These atoms and ions hold particular interest owing to the open 3*d*-subshell which allows the possibility of giant dipole resonances [2] resulting from $3p \rightarrow 3d$ $\Delta n=0$ transitions. Our study begins with scandium, motivated by its position in the group of open 3*d*-subshell elements in the periodic table. The ground state of scandium, in fact, has a single electron in the 3*d*

subshell outside closed subshells, [Ar]3d4s^2, and is the first and simplest transition metal atom. Thus, an understanding of the photoionization of scandium, with a single electron in the open 3d subshell, can serve as a springboard to the understanding of the photoionization of all of the 3d transition metal atoms and ions generally.

However, the photoionization quite complicated, owing to the proximity of the 3d and 4s levels, so that there is significant mixing in the initial state among 3d4s^2, 3$d^2$4s and 3d^3 configurations which, in turn, leads to a plethora of final state configurations, thereby complicating the giant dipole resonances. Calculations in this energy region have been performed using various theoretical methodologies [3-5], none of which give satisfactory agreement with experiment [2,6-8]. Thus, we turn to an even simpler system, the Sc^{+2} ion for the initial investigation. The Sc^{+2} system, the simplest atomic system with an open *d*-shell, has a ground state structure given by [Ar]3d, isoelectronic to potassium, but with a valence 3d electron rather than a 4s. Another reason for the choice of doubly-ionized scandium is the existence of experimental work [9,10] to benchmark the theoretical results. Note that theoretical work using both nonrelativistic and relativistic *R*-matrix methods to study Sc^{+2} has been reported [11,12], but poor agreement with experiment was found. Clearly, further theoretical study is required to bring the calculated and measured cross sections into agreement.

In addition to Sc^{+2} phtoionization calculations, we have extended our investigation along the potassium isoelectronic sequence up to z=26 including Ti^{+3}, V^{+4}, Cr^{+5}, Mn^{+6}, Fe^{+7} and Ca^{+}; we must note here that the presence of Ca^{+} ions in our investigation with those K-like transition metals ions (Sc^{+2}, Ti^{+3}, V^{+4}, Cr^{+5}, Mn^{+6} and Fe^{+7}) is explained by the fact that the excited (metastable) state electronic structure of Ca^{+} is given by [Ar]3d;

therefore Ca^+ is a 3*d*-electron ion in its excited state. This work is to be considered as part of a broader effort (our research group project) to produce accurate data in order to understand atomic processes involving open *d*-subshell atoms.

The photoionization of an atomic system A (Ca^+, Sc^{+2}, Ti^{+3}, V^{+4}, Cr^{+5}, Mn^{+6} and Fe^{+7}) is given schematically as

$$A + h\nu \rightarrow A^+ + e, \quad (1)$$

which is the direct photoionization pathway. In addition, however, the photoionization can proceed through an intermediate resonance; this pathway is represented as

$$A + h\nu \rightarrow (A)^* \rightarrow A^+ + e. \quad (2)$$

While we are primarily interested in photoionization of those various atomic systems (Ca^+, Sc^{+2}, Ti^{+3}, V^{+4}, Cr^{+5}, Mn^{+6} and Fe^{+7}) in their ground state, in this work, the initial states of Sc^{+2} (Sc III) and Ti^{+3} (Ti IV) considered in the nonrelativistic calculations are both the ground $[Ne]3s^2 3p^6 3d\ ^2D^e$ state and the excited $[Ne]3s^2 3p^6 4s\ ^2S^e$ metastable state. This is because the measurements were performed upon a mixture of ground and metastable states in the case of Sc^{+2} ions so both cross sections are required in order to make a meaningful comparison with experiment. In the relativistic case the initial states for Sc^{+2} and Ti^{+3} are the ground $[Ne]3s^2 3p^6 3d\ ^2D^e_{3/2}$ plus the first two excited states $[Ne]3s^2 3p^6 3d\ ^2D^e_{5/2}$ and $[Ne]3s^2 3p^6 4s\ ^2S^e_{1/2}$. For the four other members of the potassium-like transition metal ions (V^{+4}, Cr^{+5}, Mn^{+6} and Fe^{+7}), the initial states in the nonrelativistic (LS coupling) calculations only contain the ground ($[Ne]3s^2 3p^6 3d\ ^2D^e$) state while in the relativistic (Breit-Pauli) calculations initial states are the ground ($[Ne]3s^2 3p^6 3d\ ^2D^e_{3/2}$) and the first excited state ($[Ne]3s^2 3p^6 3d\ ^2D^e_{5/2}$). For Ca^+ calculations, initial states in the nonrelativistic operations are both the ground

$[Ne]3s^2 3p^6 4s\ {}^2S^e$ state and the excited (metastable) $[Ne]3s^2 3p^6 3d\ {}^2D^e$ state, while in the relativistic calculations initial states are the ground state ($[Ne]3s^2 3p^6 4s\ {}^2S^e_{1/2}$) plus the first two excited states ($[Ne]3s^2 3p^6 3d\ {}^2D^e_{3/2}$ and $[Ne]3s^2 3p^6 3d\ {}^2D^e_{5/2}$).

The states of the final state ion A^+ (Ca^{+2}, Sc^{+3}, Ti^{+4}, V^{+5}, Cr^{+6}, Mn^{+7} and Fe^{+8}) are known in R-matrix language as the target states, with N=18 electrons for each of A^+ ions; those target ions are combined with the free electron to form the total final state, an N+1 = 19 electrons system. By dipole selection rules, the total final state (target state + unbound electron) can have (nonrelativistic) symmetries ${}^2P^o$, ${}^2D^o$ and ${}^2F^o$, i.e., the nonrelativistic allowed transitions are given by

$$\begin{aligned} &{}^2D^e \rightarrow {}^2P^o,\ {}^2D^o,\ {}^2F^o, \\ &{}^2S^e \rightarrow {}^2P^o. \end{aligned} \tag{3}$$

In the relativistic case, the transitions (3) become

$$\begin{aligned} &{}^2D^e_{3/2} + h\nu \rightarrow {}^2P^o_{1/2},\ {}^2P^o_{3/2},\ {}^2D^o_{3/2},\ {}^2D^o_{5/2},\ {}^2F^o_{5/2}, \\ &{}^2D^e_{5/2} + h\nu \rightarrow {}^2P^o_{3/2},\ {}^2D^o_{3/2},\ {}^2D^o_{5/2},\ {}^2F^o_{5/2},\ {}^2F^o_{7/2} \\ &{}^2S^e_{1/2} + h\nu \rightarrow {}^2P^o_{1/2},\ {}^2P^o_{3/2}. \end{aligned} \tag{4}$$

The target state A^+ (Ca^{+2}, Sc^{+3}, Ti^{+4}, V^{+5}, Cr^{+6}, Mn^{+7} and Fe^{+8}) orbitals, in the present work, are obtained by using the program AUTOSTRUCTURE [13,14]. The target state wave functions and their energy levels are determined from configuration-interaction (CI) calculations. The non-relativistic (LS-coupling scheme) and the

relativistic (Breit-Pauli) *R*-matrix methods [14,15] are employed to carry out the photoionization cross section calculations. In addition to the photoionization calculations, the resonances in the region of the giant $3p \rightarrow 3d$ excitations are analyzed (position, width and identification) using the QB code [16-18]. Theoretical photoionization cross section and resonance analysis results are compared with available experimental data [7-10,19].

The *R*-matrix method is one of the most effective and widely applied methods in studying dynamical processes involving atoms and molecules, and the atomic *R*-matrix programs have a long history; it is worth, before reporting our work, saying some words on the evolution of those programs through the last decades. As it was reported by P. G. Burke and collaborators [20,21], *R*-matrix theory was first introduced in 1946 by Wigner [22,23], then in 1947 by Wigner and Eisenbud [24] in fundamental papers describing nuclear resonance reactions. These and other early woks, applying *R*-matrix theory in nuclear physics, were comprehensively reviewed in 1958 by Lane and Thomas [25], in 1959 by Breit [26], and in 1969 by Mahaux and Weidenmüller [27]. In the early 1970s, *R* -matrix theory was introduced and developed as an *ab initio* procedure for calculating electron atom scattering cross sections, where the Coulomb interaction between the electrons and the nuclei, unlike the nuclear interactions, are known exactly [20,21,28,29], and now it is the method most frequently applied for the determination of various atomic properties [30]. The computational volume by Burke and Berrington [31] includes the major papers in *R*-matrix theory except the very recent ones, along with a comprehensive list of calculations using this method. The Opacity Project [32] and the Iron Project [33] are among the most successful worldwide projects undertaken with extensive use of the

general *R*-matrix package [34] published by Berrington *et al* in 1974. This version was subject to many modifications; many subroutines were rewritten to increase efficiency and user friendliness [35], and to include relativistic effects [36]. The suite of codes that emerged from those changes was the RMATRIX-I published in 1995 [15]. In RMATRIX-II, there were more radical changes, with particular emphasis placed on improving the efficiency of the angular-momentum package. This suite of code is now parallelized, and is published as PRMAT [37] published in 2002. Fully relativistic versions of both atomic structure (GRASP [38-40]) and collision packages (DARC [41,42]) exist, but DARC applications have been rare compared to RMATRIX-I, and mostly limited to heavy and highly ionized systems. In 2006 the *B*-Spline atomic *R*-matrix codes were published by O. Zatsarinny [30]; this package, compared to the classical (Belfast) *R*-matrix codes, has significant improvements in the way that non-orthogonal orbitals can be used to represent both the bound and continuum one-electron orbitals, and the *R*-matrix basis function are defined by a set of *B*-Splines.

In a book published in 1967 [43], Marr summarized many years of theoretical and experimental knowledge on photoionization, and described the most important applications. In 1976 Burke published a general overview [44] of different theoretical approaches to atomic photoionization including quantum defect theory, the Hartree-Fock approximation, the random phase approximation, configuration interaction theory and many body perturbation theory. Starace (1987 and 1996) presented reviews of trends and status of atomic photoionization [45,46]. In 1990, Amusia published a book devoted to the investigation of the interaction of atoms with electromagnetic radiation [47]. The

attention, in these works, is given to the low and intermediate photon energy region where the probability of photon absorption and photoionization is the largest.

This report contains, in terms of structure, six chapters and appendices beginning with chapter 1 as introduction. In chapter 2 we introduce the *R*-matrix theory and its application to photoionization; also included are all the theoretical tools used in calculations reported in this work. Chapter 3 is about the study of the photoionization of the doubly-charged scandium ions (Sc^{+2}) where we present description of calculations, results and discussion and conclusion about this specific case. In chapter 4 we study the photoionization of potassium-like transition metal ions (Ti^{+3}, V^{+4}, Cr^{+5}, Mn^{+6} and Fe^{+7}). Chapter 5 presents the photoionization study of ground and excited states of Ca^{+} ions (calculations, results and discussion and conclusion); with emphasis on the physical meaning of those results in terms of this specific dynamical process (photoionization) involving 3*d* electron atoms and ions. The concluding remarks and observations are reported in chapter 6, and the appendices contain brief description of the structure of the *R*-matrix package and sample input files for atomic structure (AUTOSTRUCTURE) and *R*-matrix codes for some cases treated in this work.

CHAPTER 2.

THEORY

2.1. Units

As was reported by Berrington *et al* [15], most of the equations are expressed in atomic units (a.u.). The unit of length is the Bohr radius $a_0 = 5.29177 \times 10^{-11}$ m, and the unit of energy is the Hartree energy $E_h = 4.35975 \times 10^{-18}$ J. Others units of energy frequently used are Rydberg (Ry) and electron-Volt (eV), and 1 E_h = 2 Ry $\approx$ 27.2114 eV. By considering Ry as the unit of energy, the energy levels of hydrogen atom are $E_n = -1/n^2$, and the energy of a free electron is k^2 where k is the wave number in a.u.. For temperature T in K, the Boltzmann's constant K_B is such that $K_BT \approx (T/157890)$ Ry. The speed of light, in a.u., has the value of 137.036 which is the reciprocal of Sommerfeld's fine structure constant α. Cross sections have the units of area, and photoionization cross sections are usually given in Megabarns (Mb) with $1\text{Mb} = 10^{-22}$ m^2.

2.2. Non-relativistic *R*-matrix Theory

2.2.1. Equation of Motion

Here we consider a system that consists of an N-electron atomic target plus one electron that is initially bound and finally free in the case of photoionization [48,49], and represents the colliding electron in a scattering process. The electromagnetic interaction between those charges particle is assumed to be the only phenomenon determining the behavior of the system. Since all information on the system is contained in the wavefunction, we are required to solve the time-independent Schrödinger equation with appropriate boundary conditions.

$$H^{N+1}\Psi = E\Psi, \tag{5}$$

where Ψ is the wavefunction, E the total energy, and H^{N+1} the Hamiltonian of the (N+1)-electrons system.

The non-relativistic (N+1)-electrons Hamiltonian in a.u. can be written as:

$$H^{N+1} = \sum_{n=1}^{N+1}\left(-\frac{1}{2}\nabla_n^2 - \frac{Z}{r_n} + \sum_{m>n}^{N+1}\frac{1}{r_{nm}} \right), \tag{6}$$

where $\mathbf{r}_n$ is the electronic radius vector drawn from the atomic nucleus with atomic number Z, and $r_{nm} = |\mathbf{r}_n - \mathbf{r}_m|$ the inter-electronic distance. We assume that the nucleus is infinitely heavy, and can be considered as point charge. The first two terms of this Hamiltonian are the one-electron terms, and represent the sum over the electron kinetic energy and the electron-nucleus Coulomb attraction. The last term is called the two-electron term, and represents the Coulomb repulsion between pairs of electrons. The expansion of $1/r_{nm}$ in spherical harmonics is written as the following:

$$\frac{1}{r_{nm}} = \sum_{\lambda\mu}\left(\frac{4\pi}{2\lambda+1} \right) Y_\lambda^{\mu *}(\hat{r}_n) Y_\lambda^{\mu}(\hat{r}_m) \frac{r_<^\lambda}{r_>^{\lambda+1}}, \tag{7}$$

where $r_<$ and $r_>$ = min and max (r_n, r_m), and standard techniques are used to evaluate the angular integrals. The wavefunction Ψ, that are solutions of equation (5), are built as linear combination of antisymmetric products of one–electron functions in spherical polar coordinates.

2.2.2. Target States

To consider the photoionization of an N + 1 electron system, we start with the wave functions of the states of the N-electron final state system (known as target states for historical reasons) [15], constructed by introducing a set of N-electron states, and possibly pseudo-states, Φ_i, that are eigenfunctions of the equation

$$H^N \Phi_i = E_i^N \Phi_i \,, \tag{8}$$

with energies E_i^N given by

$$\left\langle \Phi_i \left| H^N \right| \Phi_j \right\rangle = E_i^N \delta_{ij} \,. \tag{9}$$

Φ_i is usually written as a configuration-interaction (CI) expansion in terms of some basis configuration functions ϕ_i,

$$\Phi_i(x_1, x_2, ..., x_N) = \sum_k b_{ik} \phi_k(x_1, x_2, ..., x_N) \,, \tag{10}$$

where $x_j = r_j \sigma_j$ stands for the spatial position and spin of the jth electron, and b_{ik} are the ϕ_i configuration mixing coefficients found by diagonalizing the target Hamiltonian matrix. The configuration functions ϕ_i are constructed from a bound orbital basis set consisting of self-consistent field (SCF) orbitals plus some additional pseudo-orbitals included to model electron correlation effects. For a given ϕ_i configuration function, each one-electron orbital is a product of a radial function, a spherical harmonic and a spin function:

$$o_{nlm_l}(r, m_s) = \frac{1}{r} P_{nl}(r) Y_l^{m_l}(\theta, \phi) X(m_s) \,. \tag{11}$$

Those orbitals form an orthonormal set, and their radial parts $P_{nl}(r)$ satisfy the orthonormality relations,

$$\left\langle P_{n_i l} \left| P_{n_j l} \right\rangle = \int_0^\infty P_{n_i l}(r) P_{n_j l}(r) dr = \delta_{n_i n_j} \,. \tag{12}$$

The radial functions $P_{nl}(r)$ must be input to the R-matrix programs, and are obtained from atomic structure packages such as CIV3 [50], SUPERSTRUCTURE [13,53], or AUTOSTRUCTURE [14,51,52].

2.2.3. Channels, symmetries and selection rules

There are some constraints involved in combining the scattering or bound electron with the target or core, and more constraints come from the selection rules for an electric dipole transition where the system absorbs a photon.

2.2.3.1. Conservation of Total Angular Momentum and Parity

Target N-electrons states are labeled by orbital angular momentum L^t, spin angular momentum S^t and parity π^t. These states are constructed from linear combinations of configuration state functions which have the same (orbital and spin) angular momenta and parity. A target state can be distinguished by the CSF (configuration state function) mixing coefficients, and it has a particular energy. The (N+1)-electron or target + electron system is also characterized by total orbital angular momentum L, total spin angular momentum S, and overall parity π. L is obtained by coupling vectorially L^t and l^e, the orbital angular momentum of the additional electron; S is formed by coupling S^t and s^e, the spin angular momentum (1/2) of the additional electron. One way of doing the above vectorial coupling is to apply the usual triangular relation: $|L^t - l^e| \leq L \leq L^t + l^e$, where the difference between each L is 1. Each triplet of quantum numbers L, S and π are referred to as a "'symmetry". Thus the symmetry of the (N+1)-electron system is composed of possible "channels" which are the different ways of coupling $L^tS^t\pi^t$ and $l^es^e\pi^e$ to obtain $LS\pi$.

In a scattering process, the symmetry is conserved; the channel will change for an inelastic scattering, but will not for an elastic scattering. In a photoionization phenomenon, the dipole transition process involves absorption of a photon of angular

momentum 1 and a change of parity; the symmetry (LSπ) is not conserved, but the total spin S is conserved. Consequently photoionization from a specific bound state limits the number of symmetries in the calculation to two or three.

2.2.3.2. Conservation of Energy

Considering E as the total energy and E_i^N the energy of the target state coupled to the *ith* channel in a.u. The scattering electron channel energy k_i^2, in Ry, is given by k_i^2 = 2(E - E_i^N). An open channel has $k_i^2 > 0$, a closed channel has $k_i^2 < 0$, and at the channel threshold $k_i^2 = 0$. In a photoionization process with photon energy ω in Ry and an initial state energy E_0^{N+1} in a.u., then the photoelectron energy k_i^2 in Ry is given by $k_i^2 = 2\omega +$ 2(E_0^{N+1} - E_i^N), where ω is the photon energy in a.u..

2.2.4. Partition of Configuration Space

The *R*-matrix theory is based on partitioning the configuration space describing the photoionization process into two regions (internal and external regions) by a sphere of radius a centered on the target nucleus [24]; in each of these two regions, the process has distinctively different physical properties; therefore the wavefunction describing the process have region-dependent representation. In the internal region ($r \leq a$), with r representing the relative coordinate of the photoelectron and the target nucleus, electron exchange and correlation between the photoelectron and the N-electron target are important, and the (N+1)-electron collision complex has the same behavior as a bound state. As a consequence, a configuration interaction (CI) expansion of this complex, similar to that used in bound state calculations, is adopted. In the external region ($r > a$), with a chosen large enough so that the charge distribution of the target is contained inside

the sphere, electron exchange between the photoelectron and the target is negligible; the photoelectron moves in a simple long-range potential of the target. On the boundary the *R*-matrix links those two regions. The N-electron target orbitals equation (11) must vanish in the external region; in practice this means, for all bound orbitals included in the calculations, the radius a is chosen such that $| P_{nl}(r=a) | < \delta$, where δ is some small number.

2.2.5. Internal Region

In the internal region, the (N+1)*th* electron is considered, in quantum mechanics, as undistinguishable from the N target electrons. Since, in this region, the (N+1)-electron complex behaves in a similar way to a bound state, the total wavefunction that is solution to equation (5) is expanded in a configuration interaction basis which takes the following general form:

$$\psi_k(x_1, x_2, ..., x_{N+1}) = A\sum_{ij} c_{ijk}\,\overline{\Phi}_i(x_1, ..., x_N; \hat{r}_{N+1}\sigma_{N+1})\frac{1}{r_{N+1}}u_{ij}(r_{N+1}) + \sum_j d_{jk}\chi_j(x_1, ..., x_{N+1}) \quad (13)$$

for each set of quantum numbers S, L and π. In equation (13), *j* is the continuum basis index for a particular *k*, *i* is the channel index indicating a pair ($L^tS^t\pi^t$, $l^es^e\pi^e$) coupled to get the total orbital and spin angular momenta S, L and parity π. The x_i denote the spatial $\hat{r}_i$ and the spin σ_i coordinates of the *i*th electron. A is the antisymmetrization operator ($N+1^{-\frac{1}{2}}\sum_{n=1}^{N+1}-1^{n}$) which takes account of the exchange effects between the target electrons and the free electron, and the $\overline{\Phi}_i$ are the channel functions obtained by coupling the target state Φ_i defined by equations (9) and (10) and the angular and spin functions of the continuum electron to form states of the same total angular momentum

and parity. The functions u_{ij} (the only non-zero functions in equation (13) at the surface boundary r = a) are the radial continuum basis orbitals representing the unbound electron. Finally the χ_i represent the quadratically integrable (L^2) functions, formed from the bound orbitals, and included to ensure completeness of the total wavefunction and to allow for electron correlation effects. The parameters c_{ijk} and d_{jk} are calculated by diagonalizing the (N+1)-electron Hamiltonian within the inner region of the R-matrix box:

$$\psi_k \left| H^{N+1} \right| \psi_{k'} = E_k \delta_{kk'} . \tag{14}$$

The finite range of this integration (from r = 0 to r = a) is indicated by the use of round brackets in equation (14). The (N+1)-electron Hamiltonian operator H^{N+1} is now projected onto the space of the functions ψ_k. If we write equation (13) in a more convenient form [15,48]

$$\psi_k = \sum_{\lambda} \varphi_\lambda V_{k\lambda} , \tag{15}$$

where φ_λ denote collectively the basis functions $A\overline{\Phi}_i u_{ij}$ and χ_j, and the $V_{k\lambda}$ denote collectively the coefficients c_{ijk} and d_{jk}; then the Hamiltonian matrix elements are determined by

$$H_{\lambda\lambda'} = \varphi_\chi \left| H^{N+1} \right| \varphi_{\chi'} . \tag{16}$$

To evaluate the above matrix elements, we proceed as in equation (9), except that now all radial integrals involving continuum orbitals are taken over the finite range of r (inside the internal region). The diagonalization of this matrix leads to the eigenvector

$V_{k\chi}$ (i.e. the coefficients c_{ijk} and d_{jk} in equation (13)), together with the eigenvalues E_k in equation (14).

2.2.6. Continuum Orbitals

We now consider the form adopted for the radial continuum basis orbitals u_{ij}(r) in expression (13). For each angular momentum l_i, the u_{ij}(r) generally are chosen to be solutions of the zero-order radial differential equation that follows

$$\left(\frac{\mathrm{d}^2}{\mathrm{dr}^2} - \frac{l_i(l_i+1)}{r^2} + V_0(r) + k_{ij}^2\right) u_{ij}(r) = \sum_n \Lambda_{ijn} P_{nl_i}(r), \tag{17}$$

and satisfying the fixed (homogeneous) boundary conditions

$$u_{ij}(0) = 0, \qquad \left(\frac{a}{u_{ij}(a)}\right)\left(\frac{du_{ij}}{dr}\right)_{r=a} = b; \tag{18}$$

where b is an arbitrary constant which is usually taken to be zero, a is the radius of the sphere defining the internal region, and k_{ij}^2 are the eigenvalues in Rydberg. The summation index n, in equation (17), goes over the reduced radial physical orbitals $P_{nl_i}(r)$ used to construct the target states included in expansion (13) for the given l_i. $V_0(r)$ is a zero-order potential which, near the nucleus, behaves like 2Z/r; it is normally chosen to be the static potential of the target. The Lagrange multipliers, Λ_{ijn}, ensure that the continuum orbitals are orthogonal to bound orbitals $P_{nl_i}(r)$ of the same angular symmetry; they are chosen so that the orthogonality constraints

$$\int_0^a u_{ij}(r) P_{nl_i}(r) dr = 0 \tag{19}$$

are satisfied for all j and n. It follows that the radial continuum basis orbitals u_{ij} generated that way are mutually orthogonal, and can be normalized so that

$$\int_0^a u_{ij}(r)u_{ij'}(r)dr = \delta_{jj'} . \tag{20}$$

It follows, from this and equation (12), that orbitals

$$P_{n_{\min}l_i}, ..., P_{n_{\max}l_i}, u_{i1}, u_{i2}, ... \qquad \text{with } n_{\min} = l_i + 1 \tag{21}$$

form a complete set of functions over the range r = 0 to r = a for each l_i. The bound and continuum orbitals defined in this way, as well as the ψ_k basis expansion in equation (13), are all independent of the total (N+1)-electron energy. A detailed discussion of the equation (17) has been given by W. D. Robb [54].

2.2.7. Derivation of the *R*-matrix

For any total (N+1)-electron system energy *E*, the total wavefunction Ψ, that satisfies equations (5), in the internal region and the *R*-matrix on the boundary, can be established using a theory developed by Burke et al [20,21,28]. Ψ is expanded in terms of the basis ψ_k in equation (13) as

$$\Psi = \sum_k A_{Ek}\psi_k , \tag{22}$$

where the energy dependence is carried through coefficients A_{Ek} knowing that ψ_k are energy independent.

In order to determine the A_{Ek}, we start from the relation

$$\psi_k \left| H^{N+1} \right| \psi \; - \; \psi \left| H^{N+1} \right| \psi_k \; = \; E - E_k \quad \psi_k \,|\, \psi \;\; , \tag{23}$$

which follows from equations (5), (14) and (22). Only the kinetic energy operator contributes to the left hand side of this equation, and so we obtain

$$-\frac{1}{2}\; N+1 \left[\; \psi_k \left| \nabla^2_{N+1} \right| \psi \; - \; \psi \left| \nabla^2_{N+1} \right| \psi_k \; \right] = \; E - E_k \quad \psi_k \,|\, \psi \;\; . \tag{24}$$

We can simplify equation (24) by noting that the only non-zero contribution occurs when the operator ∇^2_{N+1} acts on the continuum orbitals. Using equation (22), we obtain

$$-\frac{1}{2}\sum_{ijk'} A_{Ek'}\left[\ \overline{\Phi}_i w_{ik}\ \ r_{N+1}\ \left|\nabla^2_{N+1}\right|\overline{\Phi}_j w_{jk'}\ \ r_{N+1}\ \ -\ \overline{\Phi}_j w_{jk'}\ \ r_{N+1}\ \left|\nabla^2_{N+1}\right|\overline{\Phi}_i w_{ik}\ \ r_{N+1}\ \right]$$

$$=\ E-E_k\ \ \psi_k\,|\psi\ \ , \tag{25}$$

where w_{ik} is defined by

$$\frac{1}{r}w_{ik}(r)=\frac{1}{r}\sum_j c_{ijk}u_{ij}(r)=\ \overline{\Phi}_i\,|\psi_k\ \ . \tag{26}$$

We also define the reduced radial wavefunction of the scattered electron in channel *i* at energy *E*:

$$\frac{1}{r}F_i(r)=\frac{1}{r}\sum_k A_{Ek}w_{ik}(r)=\ \overline{\Phi}_i\,|\psi\ \ . \tag{27}$$

In equations (26) and (27) the integration is carried out over all electron space and spin coordinates except the radial coordinate r of the scattered electron. Using the orthonormality condition on the Φ_i, we obtain

$$-\frac{1}{2}\sum_i\left[\left(w_{ik}\left|\frac{\mathrm{d}^2}{\mathrm{dr}^2}\right|F_i\right)-\left(F_i\left|\frac{\mathrm{d}^2}{\mathrm{dr}^2}\right|w_{ik}\right)\right]=\ E-E_k\ \ A_{Ek}\,. \tag{28}$$

Applying the Green's theorem, and using the boundary conditions in equation (18), we obtain

$$-\frac{1}{2}\sum_i w_{ik}(a)\left(\frac{\mathrm{d}F_i}{\mathrm{d}r}-\frac{b}{a}F_i\right)_{r=a}=\ E-E_k\ \ A_{Ek}\,. \tag{29}$$

This allows us to extract the A_{Ek} coefficients:

$$A_{Ek} = \frac{1}{2a}\ \left[E_k - E\right]^{-1} \sum_i w_{ik}(a)\left(a\frac{\mathrm{d}F_i}{\mathrm{d}r} - bF_i \right)_{r=a} . \tag{30}$$

Multiplying by w_{jk}, and summing over *k* we obtain, using equation (27),

$$F_i(a) = \sum_j R_{ij}(E)\left(a\frac{\mathrm{d}F_j}{\mathrm{d}r} - bF_j \right)_{r=a}, \tag{31}$$

where we have introduced the *R*-matrix, whose elements are defined by

$$R_{ij}(E) = \frac{1}{2a}\sum_k \frac{w_{ik}(a)w_{jk}(a)}{E_k - E} . \tag{32}$$

Equations (31) and (32) are the basic equations describing the solution of the (N+1)-electron (electron-target) problem in the internal region. The surface amplitudes $w_{ik}(a)$ and the poles E_k of the *R*-matrix are obtained directly from the eigenvectors and eigenvalues of the Hamiltonian matrix defined by equation (14). The *R*-matrix is obtained for all energies by diagonalizing H^{N+1} once for each set of quantum number L S and parity π of the electron-target system. The logarithmic derivative of the reduced radial wavefunction of the scattered electron on the boundary of the internal region is given by equation (30), and is to be matched across the boundary to the external region.

2.2.8. Buttle Correction

Since the radial continuum basis orbitals $u_{ij}(r)$ satisfy homogeneous boundary condition in equation (18), it is necessary to add a "Buttle correction" to the *R*-matrix expansion (32) in order to obtain accurate results. This correction, first introduced by Buttle [55], rectifies the omission of high-lying pole terms in expansion (32). In practice, it is only necessary to correct the diagonal elements of the *R*-matrix since the off-diagonal elements oscillate in sign, and converge rapidly. If n_c radial continuum basis orbitals are

included for a given orbital angular momentum l_i, then the Buttle correction to the diagonal elements of the *R*-matrix at the energy k_i^2 is given by

$$R_{ii}^c(n_c,k_i^2)=\frac{1}{a}\sum_{j=n_c+1}^{\infty}\frac{\left[u_{ij}(a)\right]^2}{k_{ij}^2-k_i^2}=\left[\frac{a}{u_i^0(a)}\left(\frac{\mathrm{d}u_i^0}{\mathrm{d}r}\right)_{r=a}-b\right]^{-1}-\frac{1}{a}\sum_{j=1}^{n_c}\frac{\left[u_{ij}(a)\right]^2}{k_{ij}^2-k_i^2}, \qquad (33)$$

where $u_{ij}(r)$ and k_{ij} refer to the *j*th eigensolution of equation (17), and u_i^0 is the solution to the zero-order differential equation (17) at the channel energy k_i^2 of interest without applying the boundary condition in equation (18); in those conditions, equation (17) becomes

$$\left(\frac{\mathrm{d}^2}{\mathrm{d}r^2}-\frac{l_i(l_i+1)}{r^2}+V_0(r)+k_{ij}^2\right)u_i^0(r)=\sum_k\Lambda_{ijk}P_{kl_i}(r)\,. \qquad (34)$$

In place of equation (32), we therefore use the Buttle corrected *R*-matrix:

$$R_{ij}(E)=\frac{1}{2a}\sum_k\frac{w_{ik}(a)w_{jk}(a)}{E_k-E}+R_{ii}^c(n_c,k_i^2)\delta_{ij}\,. \qquad (35)$$

2.2.9. External Region Solution

In the external region, electron exchange and correlation effects between colliding electron and target electrons are negligible, and the scattered electron is outside the atom or ion, and can be considered distinct from the N target electrons. The total wavefunction is expanded in the form

$$\psi(x_1,x_2,...,x_{N+1})=\sum_{i=1}^{n}\overline{\Phi}_i(x_1,...,x_N;\hat{r}_{N+1}\sigma_{N+1})\frac{1}{r_{N+1}}F_i(r_{N+1})\,,\qquad r\geq a\,, \qquad (36)$$

where n is the number of channel functions $\overline{\Phi}_i$ retained in equation (13), but no antisymmetrisation is required. Substituting this expansion into the Schrödinger equation (5), and projecting onto the channel functions $\overline{\Phi}_i$ then yields the following set of coupled

second-order differential equations, satisfied by the reduced radial functions $F_i(r)$ of the form

$$\left(\frac{\mathrm{d}^2}{\mathrm{d}r^2} - \frac{l_i(l_i+1)}{r^2} + \frac{2z}{r} + k_i^2\right) F_i(r) = 2\sum_{j=1}^{n} V_{ij}(r) F_j(r), \qquad i = 1, n \ (r \geq a), \tag{37}$$

Here l_i and k_i^2 are the channel angular momenta and energies, and the potential matrix V_{ij} is given by

$$V_{ij}(r) = \left\langle \overline{\Phi}_i \left| \sum_{m=1}^{N} r_{m,N+1}^{-1} \right| \overline{\Phi}_j \right\rangle = \left\langle \overline{\Phi}_i \left| \sum_{m=1}^{N} \sum_{\chi\mu} \left(\frac{4\pi}{2\lambda+1} \right) Y_\chi^{\mu^*} \ \hat{r}_m \ \ Y_\chi^{\mu} \ \ \hat{r}_{N+1} \ \ r_m^\chi \right| \overline{\Phi}_j \right\rangle \frac{1}{r^{\chi+1}}, \tag{38}$$

where we have expanded $r_{m,N+1}^{-1}$ using equation (7) with $r_m < r_{N+1} \equiv r$. Defining the long range potential coefficients a_{ij}^χ in terms of Legendre polynomials as

$$a_{ij}^\chi = \left\langle \overline{\Phi}_i \left| \sum_{m=1}^{N} r_m^\chi P_\chi \ \ \cos\theta_{m,N+1} \ \right| \overline{\Phi}_j \right\rangle, \tag{39}$$

and noting that $a_{ij}^0 = N\delta_{ij}$ because of the orthonormality of the $\overline{\Phi}_i$, the differential equations (37) reduce to

$$\left(\frac{\mathrm{d}^2}{\mathrm{d}r^2} - \frac{l_i(l_i+1)}{r^2} + \frac{z}{r} + k_i^2\right) F_i(r) = 2\sum_{\chi=1}^{\chi_{\max}} \sum_{j=1}^{n} \frac{a_{ij}^\chi}{r^{\chi+1}} F_j(r), \tag{40}$$

where $z = Z - N$ is the residual target charge, and the multipole expansion of the long-range potential is limited to $\chi_{\max}$ terms since the range of χ for which $a_{ij}^\chi \neq 0$ is determined by the angular momenta of the channels *i* and *j*. In practice we include only contributions from $\chi = 1$ and $\chi = 2$; from the fact that the function χ_i are small for $r \geq a$ [56,57]. From this we can write

$$\left|V_{ij}(r)\right| << \frac{2z}{r} \qquad \text{for} \qquad r \geq a. \tag{41}$$

The multipole potentials are therefore small perturbations.

2.2.9.1. Asymptotic Form of the Scattered Electron Wavefunction

Equation (40) can be integrated outwards using the *R*-matrix boundary conditions of equation (31) at r = a, and then fitting to an asymptotic expansion which can accurately represent solutions to equation (40) [58,61]. In the asymptotic region ($r \to \infty$), the reactance *K*-matrix, which is a real symmetric matrix, describes the asymptotic form of the wavefunction for the scattered electron; the boundary conditions at infinity [55] are

$$F_{ij}(r) \underset{r\to\infty}{\sim} \begin{cases} k_i^{-\frac{1}{2}} \sin\theta_i \delta_{ij} + \cos\theta_i K_{ij} & \text{open channels} \\ \exp(-\phi_i)\,\delta_{ij} & \text{closed channels} \end{cases}, \tag{42}$$

where the second index *j* on F_{ij} distinguishes the n_a linearly independent solutions of equation (40); n_a is the number of open channels, and

$$\begin{aligned} \theta_i &= k_i r - \frac{1}{2} l_i \pi - \eta_i \ln 2k_i r + \arg\Gamma(l_i + 1 + i\eta_i) \\ \eta_i &= -\frac{z}{k_i} \\ \phi_i &= |k_i| r - \frac{z}{|k_i|} \ln(2|k_i| r) \end{aligned} \quad . \tag{43}$$

2.2.9.2. Asymptotic Form of the Photoelectron Wavefunction

The asymptotic boundary conditions for photoionization are that the continuum wavefunction must have the asymptotic form corresponding to a Coulomb modified plane wave in the final state channel and to ingoing-waves in all open channels. It was first explained by Breit and Bethe [62], and was used by Henry and Lipsky [63] and Burke [44]. The photoelectron wavefunction boundary conditions at infinity can be written in terms of the matrix ***K*** in matrix notation as

$$\boldsymbol{F}(r) \underset{r\to\infty}{\sim} (2/\pi\boldsymbol{k})^{1/2}(\sin\theta + \cos\theta\,\boldsymbol{K})(\boldsymbol{I} + \mathrm{i}\boldsymbol{K})^{-1}. \tag{44}$$

The wavefunction in the external region can only be calculated with a full determination of the reactance matrix $\boldsymbol{K}$ that appears in equation (42); to do so we need to find the wave function at the boundary (r = a).

2.2.10. Matching of Solutions - with open channels

In previous sections (2.2.7 and 2.2.9) the wavefunction in each of both internal and external regions has been specified; now we need to link these two regions to complete the solution. In matrix formulation, the internal region wavefunction in equation (31) becomes, with the prime to specify (d/dr):

$$\boldsymbol{F} = a\boldsymbol{R}.\boldsymbol{F}' - b\boldsymbol{R}.\boldsymbol{F} \qquad (r \le a). \tag{45}$$

To relate the $n\times n$ dimensional R-matrix with the $n_a\times n_a$ dimensional K-matrix defined in equation (42), we introduce $n + n_a$ linearly independent solutions $s_{ij}(r)$ and $c_{ij}(r)$ of equation (40) satisfying the boundary conditions

$$\left.\begin{matrix} s_{ij}(r) \\ c_{ij}(r) \\ c_{ij}(r) \end{matrix}\right\} \underset{r\to\infty}{\sim} \begin{cases} \sin\theta_i\delta_{ij} & i = 1,n \quad j = 1,n_a \\ \cos\theta_i\delta_{i,j\to n_a} & i = 1,n \quad j = 1,n_a \\ \exp\ -\phi_i \ \ \delta_{i,j\to n_a} & i = 1,n \quad j = n_a+1,n \end{cases}, \tag{46}$$

where θ_i and ϕ_i are given by equation (43). We expand the reduced radial wavefunction $F_{ij}(r)$ as a linear combination of these asymptotic solutions:

$$\boldsymbol{F} = \boldsymbol{s} + \boldsymbol{c}\boldsymbol{K} \qquad (\mathrm{r} \ge \mathrm{a}). \tag{47}$$

Differentiating:

$$\boldsymbol{F}' = \boldsymbol{s}' + \boldsymbol{c}'\boldsymbol{K}, \tag{48}$$

and substituting this into equation (45) to match the internal and external region solutions on the boundary so we can eliminate $\boldsymbol{F}$ and $\boldsymbol{F}'$:

$$\boldsymbol{s} + \boldsymbol{cK} = a\boldsymbol{R}(\boldsymbol{s}' + \boldsymbol{c}'\boldsymbol{K}) - b\boldsymbol{R}\,(\boldsymbol{s} + \boldsymbol{cK}). \tag{49}$$

Solving for $\boldsymbol{K}$ let:

$$\boldsymbol{A} = -\boldsymbol{s} + a\boldsymbol{R}(\boldsymbol{s}' - \frac{b}{a}\boldsymbol{s}), \qquad \boldsymbol{B} = +\boldsymbol{c} - a\boldsymbol{R}(\boldsymbol{c}' - \frac{b}{a}\boldsymbol{c}), \tag{50}$$

then

$$\boldsymbol{BK} = \boldsymbol{A} \qquad \text{or} \qquad \boldsymbol{K} = \boldsymbol{B}^{-1}\boldsymbol{A}, \tag{51}$$

which completes the evaluation of the reactance matrix $\boldsymbol{K}$; it represents the asymptotic form of the wavefunction, and contains information for internal and external regions.

2.2.11. Electron Collision Cross Section

From the reactance matrix $\boldsymbol{K}$ scattering observables can be determined. We can then define the $n_a \times n_a$ dimensional S-matrix and T-matrix in terms of K-matrix by:

$$\boldsymbol{S} = (\boldsymbol{1} + \mathrm{i}\boldsymbol{K})(\boldsymbol{1} - \mathrm{i}\boldsymbol{K})^{-1} \text{ and } \boldsymbol{T} = 2\mathrm{i}\boldsymbol{K}(\boldsymbol{1} - \mathrm{i}\boldsymbol{K})^{-1}. \tag{52}$$

The total electron collision cross section for a transition from an initial state i to final state j is given, in atomic units, by

$$\sigma(i,j) = \frac{\pi}{2k_i^2(2L_i+1)(2S_i+1)} \sum_{LS\pi} \sum_{l_i l j} (2L+1)(2S+1) \left| T_{ji}^{LS\pi} \right|^2 . \tag{53}$$

In this equation, L_i and S_i are the target orbital and spin angular momenta, and l_i and l_j are the incident and scattered electron orbital angular momenta. The whole calculation has to be repeated in the internal, external and asymptotic regions for all significant L, S and π values that are conserved in the collision.

2.3. R-matrix Theory of Photoionization

The extension of the R-matrix theory of electron-atom scattering to treat atomic photoionization was first make by Burke and Taylor [48], and developed further by Berrington et al [15,35,56].

2.3.1. Matching of Solutions – all channels closed

The internal region wavefunction and the external region equations for closed channels are exactly as described in Sections 2.2.7 and 2.2.9. However, in the bound state problem, the wavefuncton satisfies different asymptotic boundary conditions from the free-state solutions discussed in Section 2.2.10, and this leads to a different matching condition.

When all of the channels are closed, we can define *n* linearly independent solutions of the external region equation (40). These satisfy the boundary conditions in equation (46):

$$c_{ij}(r) \underset{r\to\infty}{\sim} \exp\ -\phi_i\ \ \delta_{i,j} \qquad i=1,n \quad j=1,n\,, \tag{54}$$

where ϕ is given by equation (43). We can expand the required solutions in terms of these solutions [cf. equation (47)]:

$$F_i(r) = \boldsymbol{cx} = \sum_{j=1}^{n} c_{ij}(r)x_j \qquad i=1,n \qquad (r \ge a)\,. \tag{55}$$

The coefficient x_j can then be determined by substituting this expression for F_i into equation (45), which leads to the following *n* homogeneous equations [cf. equation (51)]:

$$\boldsymbol{cx} = a\boldsymbol{Rc'x} - b\boldsymbol{Rcx}. \tag{56}$$

Solving for $\boldsymbol{x}$ let

$$\boldsymbol{B} = \boldsymbol{c} - a\boldsymbol{R}(\boldsymbol{c'} - \frac{b}{a}\boldsymbol{c}), \tag{57}$$

which implies $\boldsymbol{Bx} = 0 = \sum_{j=1}^{n} B_{ij} r x_j \qquad i=1,n\ .$ (58)

These equations have only nontrivial solutions at the negative energy eigenvalues corresponding to the bound states of the electron-atom system. The condition for a

solution is det $\boldsymbol{B}$ = 0. An iterative procedure for the energy has to be adopted to achieve this matching which involves the use of successive linearisations [57,64] to carry out the calculation in the vicinity of the *R*-matrix poles.

2.3.2. Differential Cross Section

The differential cross section for initial state *i* to final state *f*, with photoelectron ejected into solid angle $\mathrm{d}\Omega$ in direction $\hat{\boldsymbol{k}}$, is defined by

$$\frac{\mathrm{d}\sigma_{if}}{\mathrm{d}\Omega} = \frac{1}{F} W_{if}, \tag{59}$$

where *F* is the incident photon flux and *W* the transition probability per unit time into a group of states with energies in the region $E \pm dE$. From Fermi's golden rule we have

$$W_{if} = \frac{2\pi}{\hbar} \left| T_{fi} \right|^2 \rho_f, \tag{60}$$

where ρ_f is the density of states at energy *E*. Here we are using the S.I. units. Note that this is first order perturbation theory, and it is valid as long as the time *t*, during which the perturbation T_{fi} acts, satisfies the conditions $W_{if} t << 1$ and $dEt >> 2\pi\hbar$.

The transition amplitude T_{fi} for photoionization to a final state with total energy *E* is

$$T_{fi} = \left\langle \Psi^-_{fE} \left| H_{\mathrm{int}} \right| \Psi_i \right\rangle, \tag{61}$$

where the final state wavefunction is Ψ^-_{fE}, and the initial bound state wavefunction is Ψ_i with energy E_i.

The interaction part of the Hamiltonian H_{int} in equation (61) is an additional term in the expression of the (N+1)-electron system Hamiltonian (6) characterizing the interaction between the atomic system and the electromagnetic field described by the

vector potential $\boldsymbol{A}(\boldsymbol{r}_n, t)$. H_{int} can be expressed in terms of the vector potential $\vec{A}(\vec{r}_n, t)$ as

$$H_{\text{int}} = \frac{ie\hbar}{mc}\sum_{n=1}^{N+1}\boldsymbol{A}(\boldsymbol{r}_n, t).\nabla_n , \tag{62}$$

where there are N+1 electrons in the system. We now write

$$\boldsymbol{A}(\boldsymbol{r}_n, t) = A_0\hat{\boldsymbol{\varepsilon}}e^{i(\boldsymbol{k}.\boldsymbol{r}_n-\omega t)} + \text{complex conjugate}, \tag{63}$$

where $\hat{\boldsymbol{\varepsilon}}$ is the polarization vector of the photon beam, and where the first term in equation (63) corresponds to photon absorption and the second term (complex conjugate) to photon emission. A_0 is the complex amplitude. The incident flux *F* can be expressed [65] in terms of the Poynting vector ***P*** and the complex amplitude A_0 by

$$F = \frac{1}{h\nu}P = \frac{\nu}{\hbar c}\left|A_0\right|^2 . \tag{64}$$

We need to normalize wavefunctions in expression (61); the normalization of the initial state wavefunction Ψ_i is obtained according to

$$\left\langle \Psi_i \middle| \Psi_i \right\rangle = 1, \tag{65}$$

and we define the finale state continuum wavefunction Ψ^-_{fE} normalization by

$$\left\langle \Psi^-_{fE} \middle| \Psi^-_{f'E'} \right\rangle = \delta_{ff'}\delta(E - E'), \tag{66}$$

corresponding to the density of states factor ρ_f = 1 in equation (60).

For wavelengths of interest, $\boldsymbol{k}.\boldsymbol{r}_n << 1$, this is known as the dipole approximation; therefore the exponential in equation (63) can be replaced by unity. Combining previous equations, we obtain the velocity form of the differential cross section for photoionization:

$$\frac{\mathrm{d}\sigma_{if}^{\mathrm{V}}}{\mathrm{d}\Omega} = \frac{2\pi\hbar^2 e^2}{m^2 c\nu}\left|\left\langle \Psi_{fE}^{-}\left|\hat{\boldsymbol{\varepsilon}}.\boldsymbol{D}_V\right|\Psi_i\right\rangle\right|^2, \tag{67}$$

where we use the dipole velocity operator

$$\boldsymbol{D}_V = \sum_{n=1}^{N+1}\nabla_n . \tag{68}$$

We can derive the dipole length form of the cross section using the operator identity

$$\frac{\boldsymbol{p}_n}{m} = \frac{\mathrm{d}\boldsymbol{r}_n}{\mathrm{d}t} = \frac{1}{\mathrm{i}\hbar}\left[\boldsymbol{r}_n, H\right] \tag{69}$$

to give

$$\frac{\mathrm{d}\sigma_{if}^{L}}{\mathrm{d}\Omega} = \frac{8\pi^3\nu}{c}\left|\left\langle \Psi_{fE}^{-}\left|\hat{\boldsymbol{\varepsilon}}.\boldsymbol{D}_L\right|\Psi_i\right\rangle\right|^2, \tag{70}$$

where $\boldsymbol{D}_L$ is the dipole length operator;

$$\boldsymbol{D}_L = \sum_{n=1}^{N+1}\boldsymbol{r}_n . \tag{71}$$

Working now in atomic units, and using ω as photon energy expressed in a.u., the expressions for differential cross section in both forms (length and velocity) become

$$\frac{\mathrm{d}\sigma_{if}^{L}}{\mathrm{d}\Omega} = 4\pi^2\alpha a_0^2\omega\left|\left\langle \Psi_{fE}^{-}\left|\hat{\boldsymbol{\varepsilon}}.\boldsymbol{D}_L\right|\Psi_i\right\rangle\right|^2, \tag{72}$$

and

$$\frac{\mathrm{d}\sigma_{if}^{\mathrm{V}}}{\mathrm{d}\Omega} = \frac{4\pi^2\alpha a_0^2}{\omega}\left|\left\langle \Psi_{fE}^{-}\left|\hat{\boldsymbol{\varepsilon}}.\boldsymbol{D}_V\right|\Psi_i\right\rangle\right|^2, \tag{73}$$

where a_0 is the Bohr radius of the hydrogen atom, and α the fine-structure constant.

We must note that if exact wavefunctions are used, the dipole length and dipole velocity cross sections are identical. However, equations (72) and (73), in general, give different results, and the magnitude in the difference is often considered as an indication

of the accuracy of the approximation. In addition to these two approximations, there is a third one defined by Chandrasekhar in 1945 [66] using the acceleration form of the dipole operator. The acceleration form emphasizes on the wavefunction in the vicinity of the nucleus, and usually gives less accurate results than the first two also the dipole velocity and acceleration forms involve derivative of approximate functions therefore their accuracy might be lower than the length form. Detailed discussion about length and velocity formulas has been carried out by Starace [67,68] who argued for choosing length results over velocity results in certain model Hamiltonians. This discussion continued with Grant [69], and then with Grant and Starace [70] who resolved their difference. In general, the dipole length matrix elements have their important contribution from relatively large *r* in the asymptotic region of the wavefunction, dipole velocity matrix elements from intermediate *r*, and dipole acceleration from near the nucleus.

2.3.3. Reduced Matrix Elements

The reduced dipole matrix $a\|D\|b$ between states *a* and *b* is expressed by the Wigner-Eckart theorem [71,72] (using convention of Fano and Racah [73]) as

$$L_a \|D_1\| L_b = \frac{(2L_a+1)^{1/2}}{C(L_b l L_a; M_{L_\mu}\mu)} \left\langle L_a M_{L_a} \left| D_1^{\mu} \right| L_b M_{L_b} \right\rangle, \tag{74}$$

where μ identifies a component of the dipole vector. When μ =0, the operator on the right hand side of equation (74) represents the dipole length or the dipole velocity operator from equations (68) and (71) multiplied by the photon polarization vector $\hat{\varepsilon}$ with projection μ. The reduced dipole matrix element is the sum of two contributions: $D^{(\mathrm{I})}$ from the internal region ($r \le a$) and $D^{(\mathrm{O})}$ from the external region ($r \ge a$), and can be written as

$$D(a,b) = \langle a \| \boldsymbol{D} \| b \rangle = D^{(\mathrm{I})} + D^{(\mathrm{O})}. \tag{75}$$

To evaluate each of those two contributions, we need to consider two physical states Ψ_a and Ψ_b with expansion coefficients A_{ak} and $A_{bk'}$ as shown in equation (22).

2.3.3.1. Internal Region Contribution

The internal region contribution to equation (75) is defined as

$$D^{(\mathrm{I})}(a,b) = \langle \Psi_a \| \boldsymbol{D}^{(I)} \| \Psi_b \rangle = \sum_{kk'} A_{ak} M(k,k') A_{bk'}, \tag{76}$$

where

$$M(k,k') = \langle \psi_k \| \boldsymbol{D}^{(\mathrm{I})} \| \psi_{k'} \rangle . \tag{77}$$

To evaluate this, let φ_λ denote collectively the basis functions, and the $V_{k\lambda}$ denote collectively the coefficients c_{ijk} and d_{jk} in equation (13). Then we define a reduced matrix $\boldsymbol{D}$ with elements

$$D_{\chi\lambda'} = \langle \varphi_\lambda \| \boldsymbol{D}^{(\mathrm{I})} \| \varphi_{\lambda'} \rangle . \tag{78}$$

We can thus write equation (77) in the following matrix form:

$$M(k,k') = \boldsymbol{V}_k^{\mathrm{T}} \boldsymbol{D} \boldsymbol{V}_{k'}. \tag{79}$$

The A_{Ek} coefficients in equation (76) are given by equation (30), which, with b=0 (its usual value in practice) can be written as

$$A_{Ek} = \frac{1}{2} \langle E_k - E \rangle^{-1} \sum_i w_{ik}(a) \left(\frac{\mathrm{d}F_i}{\mathrm{d}r} \right)_{r=a} \tag{80}$$

$$= \frac{1}{2a} \langle E_k - E \rangle^{-1} \boldsymbol{w}^{\mathrm{T}} \boldsymbol{R}^{-1} \boldsymbol{F},$$

where we have used equation (31), and where the $\boldsymbol{w}$ and $\boldsymbol{R}$ matrices are given by equations (26) and (35). Defining diagonal matrices $\boldsymbol{G}_{\mathrm{a}}$ and $\boldsymbol{G}_{\mathrm{b}}$ with diagonal elements

$$G_{Ek} = \frac{1}{2a}\ E_k - E\ ^{-1}, \tag{81}$$

equation (75) becomes

$$D^{(\mathrm{I})}(a,b) = \boldsymbol{F}_a^{*T}\boldsymbol{R}_a^{-1}\boldsymbol{w}_a\boldsymbol{G}_a\boldsymbol{M}\boldsymbol{G}_b\boldsymbol{w}_b^{T}\boldsymbol{R}_b^{-1}\boldsymbol{F}_b\,. \tag{82}$$

The ***F*** matrices are given by equations (47) and (55) depending on whether free states or bound states are involved, and are considered in more detail in following subsections.

2.3.3.2. External Region Contribution

In the external region, we neglect the antisymmetrisation, and using the length operator, we can put:

$$\boldsymbol{D} = \mathbf{R} + \boldsymbol{r}, \tag{83}$$

where **R** is the operator for a transition in the target, and ***r*** that for a transition by the outer electron. We then obtain the external region contribution as

$$\boldsymbol{D}^{(\mathrm{O})}(a,b) = \sum_{ii'}\Big[\alpha_{ii'}\ F_{ia}\,|\,F_{i'b}\ + \beta_{ii'}\ F_{ia}\,\big|\boldsymbol{r}\big|\,F_{i'b}\ \Big], \tag{84}$$

where

$$\alpha_{ii'} = \ \bar{\Phi}_i\,\|\boldsymbol{R}\|\,\bar{\Phi}_{i'}\ \ \textit{and}\ \ \beta_{ii'} = \ \bar{\Phi}_i\,\|\hat{\boldsymbol{r}}\|\,\bar{\Phi}_{i'}\ . \tag{85}$$

In equation (85), $\bar{\Phi}_i$ represents the channel function in expansion (13). The coefficient $\alpha_{ii'}$ is non-zero only if there is an optically allowed transition between the target states belonging to channels *i* and i', and if $l_i = l_{i'}$; the coefficient $\beta_{ii'}$ is purely algebraic, and is non-zero only if the channels *i* and i' belong to the same target state, and if $l_i = l_{i'} \pm 1$.

In the case where the initial states are strongly bound, and can be neglected for r > a, the significant contribution comes from the internal region. However, in the case of

photoionization of excited states and photodetachment of negative ions, a significant contribution to the dipole matrix elements will come from the external region [48].

2.3.4. Oscillator Strengths

From calculations of dipole matrix elements, we can now define the line-strength for a dipole transition between state a and state b with respective energies (Ry) E_a and E_b in the length and velocity formulations:

$$\begin{aligned} S_{\mathrm{L}}(b,a) &= \left| \; b \left\| D_{\mathrm{L}} \right\| a \; \right|^2 \\ S_{\mathrm{V}}(b,a) &= 4 \; \left| E_b - E_a \right|^{-2} \left| \; b \left\| D_{\mathrm{V}} \right\| a \; \right|^2 \end{aligned} \; . \tag{86}$$

The oscillator strength is a dimensionless quantity $f(b,a)$ defined by

$$g_a f(b,a) = \frac{1}{3} \; \left| E_b - E_a \right| \; S(b,a) \, , \tag{87}$$

where g_a is the statistical weight or degeneracy of the initial state: $(2S_a+1)(2L_a+1)$ or $(2J_a+1)$ according to which coupling scheme we are using. The wavefunction appearing in the expression for reduced dipole matrix elements in equation (86) must satisfy boundary conditions in equation (54).

2.3.5. Photoionization Cross Section

2.3.5.1. Initial State Wavefunction

The boundary conditions satisfied by Ψ_i correspond to an asymptotically decaying wave in all channels, and it can be expanded in terms of the *R*-matrix basis in the internal region defined by equation (13). The appropriate expansion follows from equation (22); and this leads to

$$\Psi_i = \sum_k \psi_k A_{ki} \, , \tag{88}$$

where the coefficients A_{ki} are determined by solving the differential equation in the external region, subject to the bound state boundary conditions discussed above [equation (54)], and matching to the R-matrix boundary condition at r = a as in equation (80). The basis functions ψ_k are defined by equation (13), and the initial bound state Ψ_i is an eigenstate of the total orbital angular momentum L, the total spin angular momentum S and the parity π.

2.3.5.2. Final State Wavefunction

The boundary conditions satisfied by the final state wavefunction $\Psi^-_{fE}(\hat{\boldsymbol{k}})$ correspond to a plane wave in the direction of the ejected electron momentum $\hat{\boldsymbol{k}}$, and ingoing waves in all open channels. In the non-relativistic case (LS coupling), $\Psi^-_{fE}(\hat{\boldsymbol{k}})$ can be expanded in the form

$$\Psi^-_{fE}(\hat{\boldsymbol{k}}) = \sum_{l_f m_{l_f} L} \mathrm{i}^{l_f} \exp(-\mathrm{i}\sigma_{l_f}) Y^{m_{l_f}*}_{l_f}(\hat{\boldsymbol{k}}) \boldsymbol{C}_{L_f l_f}(LM_L; M_{L_f} m_{l_f}) \boldsymbol{C}_{S_f 1/2}(SM_S; M_{S_f} 1/2) \Psi^-_f , \qquad (89)$$

where Ψ^-_f is an eigenstate of total orbital angular momentum L and total spin angular momentum S, the $\boldsymbol{C}_{j_1 j_2}(j_{12} m_{12}; m_1 m_2)$ are Clebsch-Gordan coefficients, $L_f S_f M_{L_f} M_{S_f}$ are the quantum numbers defining the final state of the ion, $Y^{m_{l_f}}_{l_f}(\hat{\boldsymbol{k}})$ is the spherical harmonic [74] describing the ejected electron, and $\sigma_{l_f} = \arg\Gamma(l_f + 1 + \mathrm{i}\eta_f)$ with $\eta_f = (Z - N)/k_f$.

We can then expand Ψ^-_f in the form

$$\Psi^-_f = \sum_k \psi_k A^-_{kf} , \qquad (90)$$

where the coefficients A^{-}_{kf} are determined by solving the differential equation in the external region, subject to the free state boundary conditions discussed above [equation (44)], and matching to the R-matrix boundary condition at r = a as in equation (80).

The final continuum state wavefunction $\Psi^{-}_{fE}(\hat{\boldsymbol{k}})$ involves a summation over all L and π values which give a significant contribution to the photoionization cross section defined by equations (72) and (72), where the total spin S is conserved by the dipole operators in those equations.

2.3.5.3. Expression of the Total Cross Section

Let us consider a transition from an initial bound state i with energy E_i to a final free state *f* of energy $E_f = E_i + \omega$ (ω is the photon energy in Rydbergs), and leaving the final ion in a state defined by $L_f S_f$; the differential cross section for photoionization is obtained by substituting equations (89) into either equation (72) or (73), and using equation (74) with Fano and Racah notation. After averaging over the initial magnetic quantum numbers, and summing over the final magnetic quantum numbers, we find

$$\begin{aligned}\frac{d\sigma_{if}}{d\Omega} = \frac{4\pi^2 \alpha a_0^2 q}{2L_i+1} \sum_{l_f l_{f'} L L' l} & i^{l_f - l_{f'}} (-1)^{L_f + L_{f'} + \mu} \exp(-i\sigma_{l_f} + i\sigma_{l_{f'}} \\ & \times \left(\frac{2l_f+1 \quad 2l_{f'}+1 \quad 2L+1 \quad 2L'+1}{4\pi(2l+1)} \right)^{1/2} \\ & \times C_{l_f l_{f'}}(l0;00) C_{11}(l0;-\mu\mu) W(L l_f; L' l_{f'}) W(1L1L'; L_i l) \\ & \times \left\langle \Psi_i \left\| \boldsymbol{D}_1 \right\| \Psi^{-}_f \right\rangle \left\langle \Psi^{-}_f \left\| \boldsymbol{D}_1 \right\| \Psi_i \right\rangle Y^0_l(\hat{\boldsymbol{k}})\end{aligned} \quad , \qquad (91)$$

where q = ω in the length approximation, and q = 1/ω in the velocity approximation.

In the case of photoionization by an umpolarized light, the total cross section can be obtained by integrating equation (91) over all ejected electron angles, and averaging

over photon polarization μ. In this case, only l = 0 contributes, and we obtain the total cross section as

$$\sigma_{if} = \frac{4\pi^2 \alpha a_0^2 q}{3\ 2L_i + 1} \sum_{l_f L} \left| \left\langle \Psi_f^- \left\| \boldsymbol{D}_1 \right\| \Psi_i \right\rangle \right|^2 . \tag{92}$$

The approach of Berrington *et al* [15] consists of using the dipole matrix elements to define a generalized line strength similar to equation (86) for transition from an initial bound state i with energy E_i to a final free state f of energy $E_f = E_i + \omega$ (ω is the photon energy in Rydbergs):

$$\begin{aligned} S_{\mathrm{L}}(E_f, i) &= \sum_{L l_f} \left| \ L l_f E_f \left\| D_{\mathrm{L}} \right\| i \ \right|^2 \\ S_{\mathrm{V}}(E_f, i) &= 4\omega^{-2} \sum_{L l_f} \left| \ L l_f E_f \left\| D_{\mathrm{V}} \right\| i \ \right|^2 \end{aligned} . \tag{93}$$

The photoionization cross section is then obtained (length or velocity form) as

$$\sigma_{if} = \frac{4\pi^2 \alpha a_0^2 \omega}{3g} S , \tag{94}$$

where g is the statistical weight of the initial bound state, and the generalized line-strength is calculated using final state wavefunctions normalized per unit energy in Ryd. The constant part in equation (94) is $4\pi^2 \alpha a_0^2 / 3 = 2.689 \ldots\ldots \mathrm{Mb}$.

2.3.6. The Thomas-Reiche-Kuhn Sum Rule

An interesting rule about the oscillator strength distribution [75] is the Thomas-Reiche-Kuhn [76,77] sum rule given by

$$\mathrm{S}(0) = \sum_n f_n + \int_{E_n}^{\infty} \frac{\mathrm{d}f}{\mathrm{d}E} \mathrm{d}E = N + 1 , \tag{95}$$

where $\sum_n$ is the sum over the discrete states with oscillator strength f_n, and N+1 is the number of electrons in the initial state. We note that the summation appearing in equation (95) can be broken down into partial sums over excitations out of each subshell, and is to be carried out over all energy levels of the atom or ion (all the eigenstates of the Hamiltonian of the atom or ion), including continuum states [72].

2.4. Relativistic *R*-matrix Theory

Relativistic effects become important in both the target wavefunction and the scattered electron (photoelectron) wavefunction as the charge of the nucleus increases, even for low energy electron scattering (photoionization).

For electrons with kinetic energies far below the rest energy $mc^2 = 511\text{KeV}$, the Breit-Pauli Hamiltonian

$$H_{\text{BP}}^{N+1} = H^{N+1} + H_{\text{REL}}^{N+1}, \tag{96}$$

introduced by Bethe and Salpeter [78] for the case of one- and two-electrons, is sufficient to determine the equation of motion. In equation (96), H^{N+1} is the non-relativistic Hamiltonian given by equation (6), and H_{REL}^{N+1} gives rise to perturbative contributions whose relative magnitudes are low powers of α. In the expression of H_{REL}^{N+1}, we only retain the one-electron terms resulting from the reduction of the Dirac equation to Breit-Pauli form up to order $\alpha^2 Z^4$, i.e. the mass-correction term, the one-electron Darwin term and the spin-orbit term.

The low-Z Breit-Pauli Hamiltonian for an (N+1)-electron system can then be written as

$$H_{\text{BP}}^{N+1} = H^{N+1} + H_{\text{mass}}^{N+1} + H_{\text{D}}^{N+1} + H_{\text{SO}}^{N+1}, \tag{97}$$

where each of the one-electron Breit-Pauli terms can optionally be included:

$$H_{\rm mass}^{N+1} = -\frac{\alpha^2}{8}\sum_{n=1}^{N+1}\nabla_n^4 \qquad \text{(mass-correction)} \tag{98}$$

$$H_{\rm D}^{N+1} = -\frac{\alpha^2 Z}{8}\sum_{n=1}^{N+1}\nabla_n^2\left(\frac{1}{r_n}\right) \qquad \text{(Darwin)} \tag{99}$$

$$H_{\rm SO}^{N+1} = \frac{\alpha^2 Z}{2}\sum_{n=1}^{N+1}\frac{\boldsymbol{l}_n.\boldsymbol{s}_n}{r_n^3} \qquad \text{(spin-orbit)} \tag{100}$$

We note that the non-fine-structure part of the Hamiltonian

$$H_{\rm nfs}^{N+1} = H^{N+1} + H_{\rm mass}^{N+1} + H_{\rm D}^{N+1} \tag{101}$$

commutes with $\boldsymbol{L}^2$, $\boldsymbol{S}^2$, $\boldsymbol{L}_{\rm z}$, $\boldsymbol{S}_{\rm z}$ and parity, whereas $H_{\rm BP}^{N+1}$ and $H_{\rm SO}^{N+1}$ only commute with $\boldsymbol{J}^2$, $\boldsymbol{J}_{\rm z}$ and parity.

By including the spin-orbit interaction, the (N+1)-electron *R*-matrix basis functions are defined as in equation (13), but for each total angular momentum $\boldsymbol{J}$ and parity. A pair-coupling scheme

$$\boldsymbol{J}_i + \boldsymbol{l} = \boldsymbol{K} \quad \text{and} \quad \boldsymbol{K} + \boldsymbol{1/2} = \boldsymbol{J} \tag{102}$$

is used to evaluate the matrix elements [79,80], where $\boldsymbol{J}_i$ is the total angular momentum of the target state, $\boldsymbol{l}$ is the orbital angular momentum of the incident electron and ½ the spin of the incident electron. In this approach, Hamiltonian matrices and dipole matrices are first determined in LS-coupling, and then transformed using a unitary transformation to pair-coupling.

2.5. Quantum Defect and Rydberg Series

Atomic spectra often reveal phenomena associated with a Rydberg series [75]; those are states where one of the electrons is in an *nl* orbital, with *n* describing a sequence of values. For such a series, a useful concept is that of quantum defect parameter ν. In atomic hydrogen the ionization energy (IE) is $1/(2n^2)$ au. In complex neutral systems, the effective charge would be the same as in hydrogen at large r. As n increases, the mean radius becomes larger, and the probability of the electron being in the hydrogen-like potential increases. Thus, an effective quantum number n* = n - ν could be defined such that

$$\mathrm{IE}(nl) = \frac{1}{2(n-\nu)^2}. \tag{103}$$

In general, when we are not dealing with neutral systems, equation (103) must be modified to

$$\mathrm{IE}(nl) = \frac{1}{2}\left[\frac{Z-N+1}{n-\nu}\right]^2. \tag{104}$$

Quantum defect theory (QDT) has been developed to use in collision problems, and has been used for photoionization calculations. From one-channel the QDT was extended to many-channel problem (MQDT) [81]. For non-relativistic MQDT, if a level with principal quantum number *n* has total energy *E*, and has a core state with energy E_i for channel *i* and residual charge z, then the effective quantum number q_i are related to those previous quantities by

$$E = E_i - \frac{1}{2}\left[\frac{z}{q_i}\right]^2, \tag{105}$$

and the quantum defects ν_i for this level are defined as

$$\nu_i = n - q_i . \tag{106}$$

2.6. Resonance Analysis Theory with the QB Program

2.6.1. The Role of Resonances

In many cases, photoionization cross sections are dominated by resonances (autoionizing states) in certain energy ranges. As we have schematically shown it in equations (1) and (2), the photoionization process can proceed through either the direct pathway (1) or through an intermediate resonance state (2), and interference between these two routes occurs, giving rise to well-known absorption line profile which is represented [82,83] by the formula

$$\sigma=\sigma_a \frac{q+\varepsilon^{2}}{1+\varepsilon^{2}} + \sigma_b . \tag{107}$$

In equation (107), $\varepsilon=2(E-E_r)/\Gamma$, E_r is the resonance energy, Γ is the resonance width, q is the line profile index that defines the line shape, and σ_a and σ_b are background cross sections which are slowly varying with energy.

Resonances are built automatically into photoionization cross section through the behavior of the final state wavefunction $\Psi^{-}_{fE}(\hat{\boldsymbol{k}})$ which must have sufficiently versatile description to allow both routes in equations (1) and (2) to be adequately represented. This means, in practice, the final state wavefunction must contain both the open channels into which the resonance decays and the closed channels corresponding to the appropriate Rydberg series or resonance [44].

Let us consider resonance transitions from initial state a characterized by total angular momentum J_a and parity π_a to a final continuum state b characterized by total angular momentum J_b and parity π_b. The oscillator strength for these resonance transitions can be obtained from photoionization cross section σ_{ab} by

$$f(\mathrm{a} \to \mathrm{b}) = \left(\frac{1}{4\pi^2 \alpha a_0^2} \right) \int_{\Delta E_r} \sigma_{ab} dE , \tag{108}$$

where transitions ($\mathrm{a} \to \mathrm{b}$) are governed by the dipole selection rules.

2.6.2. The QB Program: Theory

The QB method [16-18] is based on the eigenphase fitting procedure that uses *R*-matrix theory to determine the energy variation of the reactance *K*-matrix or its eigenphases analytically rather than numerically. From *R*-matrix theory described above, we know that the connection between the internal region and the external region is made *via* the matrix $\boldsymbol{R}$ [32,35] which has dimension $n \times n$, with *n* representing the total number of channels retained in the close-coupling expansion (13). We also described in previous sections how other quantities such as the reactance matrix $\boldsymbol{K}$ and the scattering matrices ($\boldsymbol{S}$ and $\boldsymbol{T}$) are obtained: see equations (51) and (52). The *K*-matrix is a real symmetric matrix of dimension $n_a \times n_a$, with n_a being the number of open channels.

By diagonalizing the matrix $\boldsymbol{K}$ in the space of n_a open channels, we obtained $\boldsymbol{K}_{aa}$ with eigenvalues λ_i, then

$$\boldsymbol{K}_{aa}\boldsymbol{X} = \boldsymbol{X}\boldsymbol{\lambda}, \qquad \text{where } \boldsymbol{X}^{\mathrm{T}}\boldsymbol{X} = 1, \tag{109}$$

where $\boldsymbol{\lambda}$ is diagonal with elements λ_i. The eigenphase in each channel is then defined as

$$\delta_i = \tan^{-1} \lambda_i, \quad i = 1, n_a , \tag{110}$$

and the eigenphase sum δ is the sum over equation (110). In theoretical calculations, a resonance manifests itself by a rapid increase by π rad in the total eigenphase sum, superimposed on a background [16,17]. Since a resonance has a finite width, the change in eigenphase sum may not be exactly π because of the background variation. Therefore a resonance position is identified as the energy at which the eigenphase sum increases most rapidly, i.e. has maximum gradient $d\delta/dE=\delta'$, and this is how the QB method locates resonances.

To calculate the resonance width with the QB method, we consider the Breit-Wigner [84] form of the eigenphase sum

$$\delta(\mathrm{E}) = \bar{\delta}(\mathrm{E}) + \tan^{-1}\frac{\Gamma/2}{\mathrm{E}_\mathrm{r} - \mathrm{E}} \ , \tag{111}$$

where $\mathrm{E_r}$ is the resonance energy, Γ the resonance width and $\bar{\delta}$ is the background eigenphase. Differentiating twice, evaluating at $\mathrm{E}=\mathrm{E_r}$ and assuming the background varies slowly over the resonance profile, i.e. $\bar{\delta}' << \Gamma^{-1}$, we get the width as

$$\Gamma = 2/\delta'(\mathrm{E_r}) \, , \tag{112}$$

which means at resonance the width is related to the inverse of the eigenphase derivative.

The QB method requires an analysis of $\delta'(\mathrm{E})$, and exploits the analytic properties of *R*-matrix theory. Using matrix notation, equation (35) defining R-matrix elements with the Buttle correction is written

$$\boldsymbol{R}(\mathrm{E}) = \boldsymbol{w}\boldsymbol{\varepsilon}^{-1}\boldsymbol{w}^{\mathrm{T}} + \boldsymbol{R}_{\mathrm{Buttle}}(\mathrm{E}) \, , \tag{113}$$

where $\boldsymbol{\varepsilon}$ is a diagonal matrix with elements $\mathrm{E_k} - \mathrm{E}$. The energy derivative of the *R*-matrix is obtained analytically by differentiating equation (113), and this leads to

$$\boldsymbol{R}'(\mathrm{E}) = \boldsymbol{W}\boldsymbol{\varepsilon}^{-2}\boldsymbol{W}^{\mathrm{T}} + \boldsymbol{R}'_{\mathrm{Buttle}}(\mathrm{E}) . \tag{114}$$

The derivative $\boldsymbol{R}'$ is required in the definition of the derivative of the $\boldsymbol{K}$-matrix $\boldsymbol{K}'$, which is obtained by differentiating equation (51), and substituting for $\boldsymbol{A}$ and $\boldsymbol{B}$ from equation (50); this suggests defining an $n \times n_a$ matrix $\boldsymbol{Q}$ as follows:

$$\boldsymbol{Q}(\mathrm{E}) = (-\boldsymbol{s}' + \boldsymbol{R}'\dot{\boldsymbol{s}} + \boldsymbol{R}\dot{\boldsymbol{s}}') + (-\boldsymbol{c}' + \boldsymbol{R}'\dot{\boldsymbol{c}} + \boldsymbol{R}\dot{\boldsymbol{c}}')\boldsymbol{K} , \tag{115}$$

where the dot mean d/dr, and the prime d/dE; this implies

$$\boldsymbol{K}'(\mathrm{E}) = \boldsymbol{B}^{-1}\boldsymbol{Q} . \tag{116}$$

$\boldsymbol{K}'_{aa}$ is required in the definition of the eigenphase sum derivatives, which are given by differentiating equations (109) and (110).

$$\boldsymbol{\lambda}'(\mathrm{E}) = \boldsymbol{X}^{\mathrm{T}}\boldsymbol{K}'_{aa}\boldsymbol{X} , \tag{117}$$

$$\delta'(\mathrm{E}) = \sum_{i=1}^{n_a} (1+\lambda_i^2)^{-1}\lambda_i' . \tag{118}$$

From those equations, it is clear that the evaluation of $\delta'(\mathrm{E})$ requires data from *R*-matrix calculations.

2.7. Photoelectron Angular Distributions

For low energy photoionization, where the electric dipole approximation is excellent, it has been shown [85,86] from very general principles, conservation of angular momentum and parity, that for linearly polarized light acting upon an umpolarized target atom, the photoelectron angular distributions can be expressed as a linear combination of the Legendre polynomials $P_0(\cos(\theta)) = 1$ and $P_2(\cos(\theta)) = (3\cos^2(\theta) - 1)/2$, where c is the angle between the photoelectron propagation and the photon polarization directions. Accordingly, the differential cross section for photoionization of the *i*th shbshell of an umpolarized target by linearly polarized photon can be written [87] as

$$\frac{d\sigma_i}{d\Omega} = \frac{\sigma_i}{4\pi}\left[1 + \beta_i P_2(\cos(\theta))\right] , \tag{119}$$

where σ_i is the total subshell cross section, and β_i, which contains all of the dynamical angular distribution information, is known as the asymmetry parameter. From equation (119), it is clear that σ_i determines the overall intensity of the process. Equation (119) also shows that, since $-1/2 \le P_2(\cos(\theta)) \le 1$, then β_i is limited to the range $-1 \le \beta_i \le 2$ for all cases, since the differential crass section cannot be negative for any value of θ.

But linearly polarized incident light is not the only possibility. For example, unpolarized light may be considered as equivalent to a linear superposition of incoherent equal intensity linearly polarized beams oscillating along perpendicular x and y axes [88]. In this case, and taking the photon beam along the z-axis, the differential cross section can now be written

$$\frac{d\sigma_i}{d\Omega} = \frac{\sigma_i}{4\pi}\left[1 - \beta_i P_2(\cos(\theta_z))\right] \tag{120}$$

for unpolarized photons where θ_2 is the angle between photon and photoelectron directions. This same result is true for circularly polarized light.

Note that, in both equation (119) and (120), the dependence of the differential cross section on the asymmetry parameter β_i vanishes at the angle θ at which $P_2(\cos(\theta_z))$ vanishes, *i.e.*, where $\cos^2(\theta)=1/3$. At this angle, known as the "magic" angle (roughly 54°), the differential cross section of equation (119) or equation (120) is given by $\sigma_i / 4\pi$. Thus, measurements at this "magic" angle provide a method of measuring total cross sections using photoelectron spectroscopy without collecting the electrons with 4π geometry.

Both the subshell cross section, σ_i, and the asymmetry parameter, β_i, are generally energy- dependent [85]. The cross section, σ_i, which is proportional to the sum of the absolute squares of the dipole matrix elements for transitions from the initial state to the various allowed final states, derives its energy dependence from the dependence of the dipole matrix elements on energy. The asymmetry parameter, β_i, is expressed as a ratio, and is more complicated; the energy dependence comes about from interference of the matrix elements of the alternative possible photoionization channels so that the details of the relative magnitudes and phases of the various dipole matrix elements are crucial. An obvious corollary is that for a photoionization process consisting of only a single possible channel, β_i must be energy-independent and determined only by geometrical factors: angular momentum geometry.

2.8. Model Potentials

In target containing a large number of electrons, an appreciable saving of computational effort can be achieved by replacing the interaction of the valence and continuum electrons with the closed shell core by a model potential [15]. This allows the calculation to proceed solely in terms of the valence and continuum electrons.

Consider the case of N-electron atom. If there are N_c-electrons in the closed shell core, then there are $M = N - N_c$ valence electrons. The Hamiltonian equation (6) becomes

$$H^{N+1} = \sum_{n=1}^{M+1}\left(-\frac{1}{2}\nabla_n^2 - V(r_n) + \sum_{m>n}^{M+1}\frac{1}{r_{nm}} \right), \tag{121}$$

where $V(r)$ is the model potential with specific form left to the user, but limits at zero and infinity are well known:

$$V(r) \underset{r\to 0}{\sim} -Z/r \quad \text{and} \quad V(r) \underset{r\to\infty}{\sim} -z/r\,, \tag{122}$$

where, as usual, Z is the nuclear change, and $z = Z\text{-}N$ is the residual target charge. The basis states ψ_k of expansion (13) are now $(M+1)$-electrons functions, where Φ are built from the valence orbitals. However, it should be noted that for the purpose of orthogonalisation, in the determination of the continuum orbitals, the complete set of one-electron bound orbitals (including core functions) are required to be read into the code at the first stage.

CHAPTER 3.

PHOTOIONIZATION OF DOUBLY CHARGED SCANDIUM IONS

3.1. Description of the Calculations

The target states of Sc IV (Sc^{+3}) orbitals were generated using the code AUTOSTRUCTURE [13,14,51,52]. Each of the single-particle spectroscopic orbitals (1*s*, 2*s*, 2*p*, 3*s*, 3*p*, 3*d*, 4*s*, 4*p*) and the pseudo-orbitals ($4\bar{d}, 4\bar{f}, 5\bar{s}, 5\bar{p}, 5\bar{d}$) radial wave functions was determined using the Thomas-Fermi statistical model radial functions calculated within the program. Using these orbitals, a configuration-interaction (CI) expansion of the Sc IV configuration functions to obtain the N-electron target states was performed. The set of configuration functions included five spectroscopic configurations, $3s^2 3p^6$, $3s^2 3p^5 3d$, $3s^2 3p^5 4s$, $3s^2 3p^5 4p$ and $3s 3p^6 3d$, and correlation configurations that, to begin with, included all one- and two-electron replacements of the n = 3 orbitals of the ground state of Sc^{+3}. To make the subsequent photoionization calculation more tractable, correlation configurations with very small coefficients in the CI expansions were removed, leaving us with 19 correlation configurations. Specifically, the correlation configurations included are $3s^2 3p^5 4d$, $3s^2 3p^5 4f$, $3s^2 3p^5 5s$, $3s^2 3p^5 5p$, $3s^2 3p^5 5d$, $3s^2 3p^4 3d^2$, $3s^2 3p^4 3d 4p$, $3s^2 3p^4 4s 4p$, $3s^2 3p^4 4p 4d$, $3s^2 3p^4 3d 4f$, $3s^2 3p^4 4s 4f$, $3s^2 3p^4 4p 4f$, $3s^2 3p^3 3d^3$, $3s^2 3p^3 3d^2 4s$, $3s^2 3p^3 4s 4p^2$, $3s 3p^5 3d^2$, $3s 3p^5 3d 4s$, $3s 3p^5 3d 4p$, $3s 3p^4 3d^3$. Thus, a total of 24 configurations corresponding to 558 LS terms were included in the nonrelativistic calculation; for the relativistic (BP) calculation, the relativistic spin-orbit, Darwin and mass correction terms were added to the Hamiltonian and the resulting CI yielded LSJ terms constructed from the LS terms.

To get some idea of the accuracy of the N-electron target state energies, the calculated and (J-averaged) experimental (NIST) [89] energy levels relative to the ground state of Sc^{+3} states are shown in table 3.1, and reasonable agreement with experiment is seen.

Table 3.1: Calculated and experimental (NIST) [89] energy levels in Rydbergs f6r states of Sc IV (Sc^{+3}) relative to the ground state.

Sc IV state	Cal. energy level	Exp. energy level
$3s^2 3p^6\ {}^1S^e$	0.00000	0.00000
$3s^2 3p^5 3d\ {}^3P^o$	2.18292	2.18451
$3s^2 3p^5 3d\ {}^3F^o$	2.30121	2.29462
$3s^2 3p^5 3d\ {}^1D^o$	2.44422	2.43695
$3s^2 3p^5 3d\ {}^3D^o$	2.45179	2.44940
$3s^2 3p^5 3d\ {}^1F^o$	2.46904	2.47003
$3s^2 3p^5 4s\ {}^3P^o$	3.05900	3.04732
$3s^2 3p^5 4s\ {}^1P^o$	3.09385	3.07537
$3s^2 3p^5 3d\ {}^1P^o$	3.18474	3.14392
$3s^2 3p^5 4p\ {}^3S^e$	3.35462	3.38750
$3s^2 3p^5 4p\ {}^3D^e$	3.42229	3.45029
$3s^2 3p^5 4p\ {}^3P^e$	3.46903	3.49331
$3s^2 3p^5 4p\ {}^1P^e$	3.46290	3.49495
$3s^2 3p^5 4p\ {}^1D^e$	3.45571	3.50529
$3s^2 3p^5 4p\ {}^1S^e$	3.69386	3.62238
$3s3p^6 3d\ {}^3D^e$	3.95760	3.91567
$3s3p^6 3d\ {}^1D^e$	4.08921	4.02822

Two separate photoionization cross section calculations were performed. In the first, relativistic effects were neglected, and the calculation was carried out with the LS-coupling non-relativistic *R*-matrix codes [14,15]. In the first sum in equation (13), only the terms arising from the spectroscopic configurations are included which abnegates the possibility of pseudo-resonances. In the (purely discrete) second sum, however, all of the terms from the 24 N-electron configurations, coupled to all of the single-particle orbitals, both spectroscopic and correlation, are included in the set of χ_i.

The initial state wave function, in each case, was constructed from the N-electron target states to include the main configuration, $3s^2 3p^6 3d$ or $3s^2 3p^6 4s$, along with all single electron promotions out the 3*s*, 3*p* and the outer shell (3*d* or 4*s*), along with all double promotions of the type $3s^2 3p^5 nln'l'$, and the important double promotions of the $3s^2 3p^4 3d^2 nl$ variety. Other possible two-electron promotions were omitted to insure that the ground state was not overcorrelated as compared to the target states, i.e., to balance the calculation. The terms arising from these states formed the basis of a large CI calculation to obtain the initial state wave function. In table 3.2 are presented the threshold energies of the two nonrelativistic states of doubly-ionized scandium (Sc^{+2}), the $[Ne]3s^2 3p^6 3d\ ^2D^e$ state and the excited $[Ne]3s^2 3p^6 4s\ ^2S^e$ metastable state, along with the corresponding three relativistic initial states, the ground state $[Ne]3s^2 3p^6 3d\ ^2D^e_{3/2}$ plus the first two (metastable) excited states $[Ne]3s^2 3p^6 3d\ ^2D^e_{5/2}$ and $[Ne]3s^2 3p^6 4s\ ^2S^e_{1/2}$. Comparing our theoretical ionization potentials with experimental data [9,10], also shown in the table 3.2, it is evident that agreement between theory and experiment is rather good.

Table 3.2: Sc III (Sc^{+2}) states threshold energy in eV compared to experiment [9,10].

State	Calculation	Experiment	Error (%)	Abundance (%)
$^2D^e$	24.71	24.74	0.12	75.3
$^2S^e$	21.86	21.59	1.23	24.7
$^2D^e_{3/2}$	24.73	24.75	0.08	20.7
$^2D^e_{5/2}$	24.70	24.73	0.12	54.6
$^2S^e_{1/2}$	21.86	21.59	1.25	24.7

In both LS and BP calculations, the R-matrix box radius was 21.81 au, and 34 basis orbitals were used to represent the continuum for each value of the angular momentum. The QB method [16-18] is adopted in this work to determine the resonance energies and widths. The QB method works in the *R*-matrix environment (see subsection 2.6 above).

3.2. Results and Discussion

3.2.1. Non-relativistic (LS coupling) Calculations

The experimental Sc^{+2} sample contains 75.3 % of $^2D^e$ (ground level) and 24.7 % of $^2S^e$ (excited level) [9, 10], and those state fractions are used in determining the total photoionization cross sections of Sc^{+2} to compare with experiment. We present the total photoionization cross sections of Sc^{+2} as a result of combining the photoionization cross sections of the two levels using their respective abundances in the experimental Sc^{+2} sample, however, figures 3.1(a) and 3.1(b) respectively illustrate the individual photoionization cross sections from excited $^2S^e$ and ground $^2D^e$ states of Sc^{+2}; since, in

both cases, the photoionization cross sections obtained using length and velocity forms agree very well, only one form (length) is displayed here and in all subsequent figures.

Figure 3.1(c) shows the total cross sections of the weighted mixture of ground and excited Sc^{+2} (75.3 % of $^2D^e$ and 24.7 % of $^2S^e$) from threshold to 68.0 eV. In the region of photon energy below 30.0 eV, there are no resonances in the total photoionization cross sections; only the direct photoionization process is possible here. The threshold cross section has a value of 1.81 Mb. Between photon energy 30.0 eV and 50.0 eV, we have a mixture of direct nonresonant and indirect resonance processes, and it is evident that the resonance excitations are dominant in this region where the cross section can reach hundreds of Mb; this is the region of giant, $3p \rightarrow 3d$, resonances. These $3p \rightarrow 3d$ resonances are so strong because they represent $\Delta n=0$ transitions, and, since the spatial extent of a wave function is determined largely by the principal quantum number, n, the $3p$ and $3d$ wave functions occupy substantially the same region of space, resulting in significant overlap and a rather large dipole matrix element. The photoionization cross section in this region is dominated by resonances which decay *via* autoionizing processes leading to the ground $3s^2 3p^6\ ^1S^e$ state of Sc^{+3}. Above 50.0 eV photon energy, the photoionization cross section exhibits complex resonance structure, and this can be explained by the fact that the photon energy in this region is high enough to produce, through resonance excitation followed by autoionization, both ground and excited states of Sc^{+3} including $3s^2 3p^6\ ^1S^e$, $3s^2 3p^5 3d\ ^3P^o$, $3s^2 3p^5 3d\ ^3F^o$, etc., i.e., ionization plus excitation.

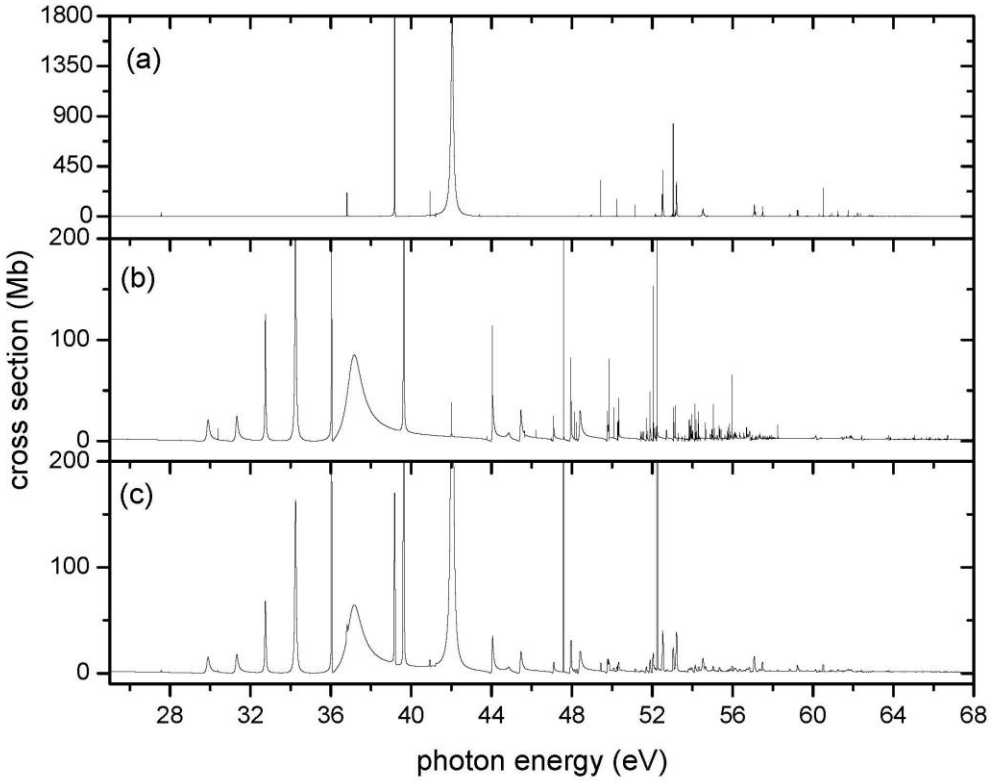

Figure 3.1: Calculated photoionization cross sections of Sc^{+2}: (a) initial $^2S^e$ excited state, (b) initial $^2D^e$ ground state, and (c) total photoionization cross sections obtained from a weighted sum of (a) and (b) showing the two strongest resonances at energies 37.17 and 42.04 eV. Note the complex resonance structure at photon energies above 45 eV.

It is worth noting that most of the characteristics of the Sc^{+2} photoionization cross section spectrum originate from the ejection of the 3*d* electron (or 4*s* for the excited state), leading to the ground state of the target, $3s^2 3p^6\ ^1S^e$. Up to a photon energy of 54.40 eV, only this channel is open; consequently other channels play minor roles in defining the photoionization cross section in the energy range considered in this work

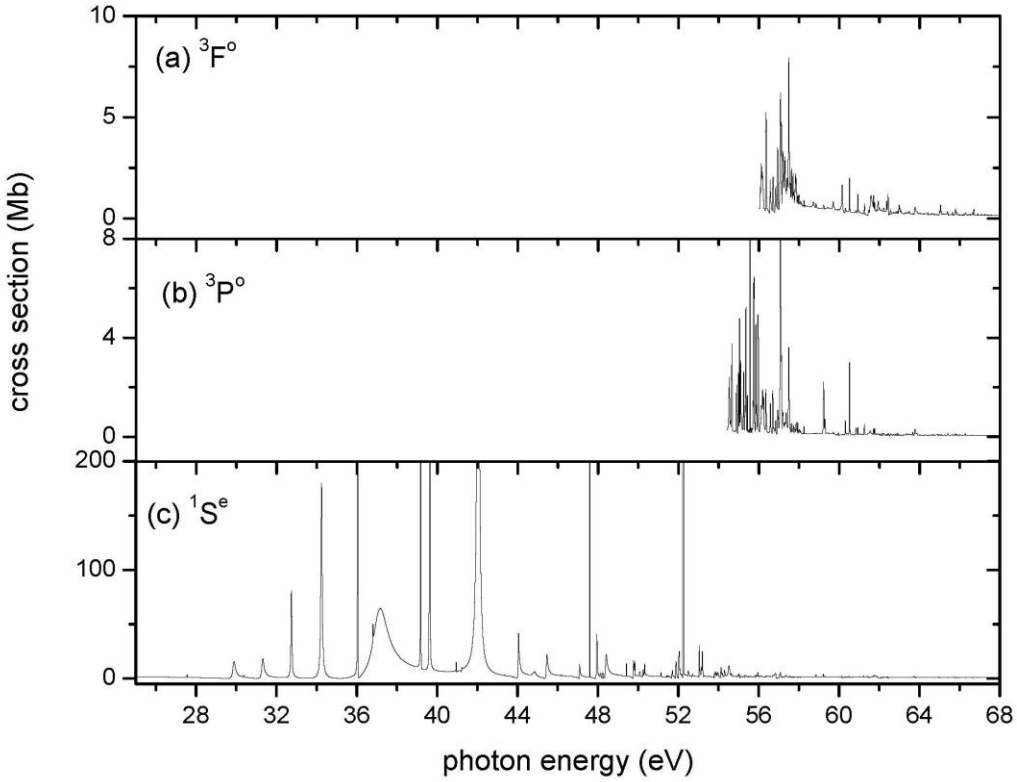

Figure 3.2: Calculated photoionization cross section for the weighted sum of ^{2}S^e and ^{2}D^e initial states for the satellite transitions leaving the Sc^{+3} ion in the (a) $3s^2 3p^5 3d$ ^{3}F^o excited state and (b) $3s^2 3p^5 3d$ ^{3}P^o excited state, along with (c) the main line transition to the $3s^2 3p^6$ ^{1}S^o ground state of Sc^{+3}.

(threshold to 68.0 eV). Figure 3.2 is illustrative of the importance of the main line $3s^2 3p^6$ ^{1}S^e [figure 3.2(c)] compared to the satellite lines $3s^2 3p^5 3d$ ^{3}P^o and $3s^2 3p^5 3d$

$^3F^o$ [figures 3.2(b) and 3.2(a)]. Note particularly the vertical scales of figures 3.2(a) and 3.2(b) as compared to figure 3.1(c).

Figure 3.3 shows comparison between our LS results and the experimental data [9,10] for photon energies from 29 to 53.0 eV for the weighted average of $^2D^e$ and $^2S^e$ initial states. The theoretical results have been broadened by a 40 meV width Gaussian to account for experimental resolution. The two strongest and broadest resonances of Sc^{+2} arise from $^2D^e$ and $^2S^e$ symmetries, and are located respectively at 37.17 eV and 42.04 eV, as seen in figure 3.3(a). Experimental results [9,10] showed those resonances were positioned at 37.13 eV and 41.80 eV (see figure 3.3(b). Since this calculation is a non-relativistic operation (LS coupling), relativistic effects, such as fine structure splitting, are not included, and the absence of the spin-orbit interaction term in the calculation can be observed in figure 3.3(a) where the theoretical photoionization cross section spectrum doesn't show any splitting. Above 45.0 eV both photoionization cross section spectra 3.3(a) and 3.3(b) reveal differences even though they are less clear than in lower photon energies. Despite the use of non-relativistic R-matrix method in this first part of this work, our results reproduce experimental results better than any previous theoretical works [11,12] to the best of our knowledge; particularly if we consider the most prominent resonance positions. Deviations obtained here are smaller than those in previous theoretical calculations [11,12], relativistic or non-relativistic. As far as absolute magnitudes are concerned, for reasons that shall be discussed below, we believe that the reported experimental cross sections are too small by a factor of 1.632. Thus, the experimental cross section shown in figure 3.3(b) has been multiplied by that factor.

With this factor, the dominant resonances in the 37 eV and 42 eV regions are seen to be in excellent agreement.

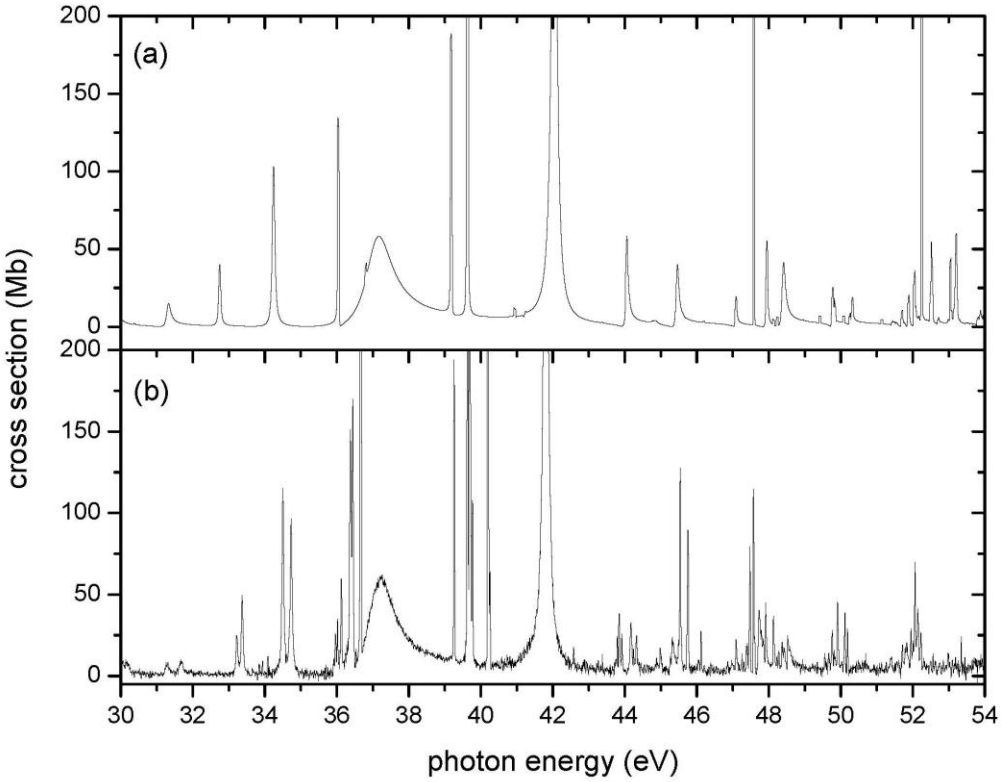

Figure 3.3: Sc^{+2} photoionization cross sections from 29 to 53.0 eV for a weighted average of $^2D^e$ and $^2S^e$ initial states; (a) theory (LS-coupling) and (b) modified experiment [9,10]. Note the difference between the two spectra due to the absence of the spin-orbit interaction from the theoretical calculation. The experimental cross section has been multiplied by a factor of 1.632 for reason discussed below.

The QB methodology is used to analyze resonances in terms of energies, widths and transitions. The results of our calculations are compared in table 3 with the experimental data [9,10]. The resonance widths obtained in our calculation are in good

agreement with experimental data, as seen in table 3.3. For example the two strongest photoionization resonances have theoretical widths of 850.4 meV and 146.6 meV, and the corresponding experimental widths are 847 and 148 meV respectively. In the theoretical resonance structure, we observe various widths from a very narrow (3.4 meV) to a very broad (850.4 meV). Since the nonrelativistic LS calculation omits fine structure splittings, our major resonance structure and identifications, in the region of giant resonances, appear simpler than experimental [9,10]. For the ground state Sc^{+2} ($^2D^e$), nine resonances have been identified in the photon energies from 29 to 45 eV [table 3.3 and figure 3.4(b)]. The spectrum of the excited state Sc^{+2} ($^2S^e$) shows less complexity than the $^2D^e$ case, and we only have three resonances between 30 and 45 eV [table 3.3 and figure 3.4(a)].

Many resonances in the photoionization cross section spectra exhibit an asymmetric shape, i.e., a Fano profile; this is due to the interference between the direct photoionization channels and the resonant channels. Figure 3.4 also shows that the two strongest resonances have great differences in their shapes. The $^2D^e \rightarrow 3p^5 3d\ (^3F) 4s\ ^2F^o$ resonance in figure 3.4(b) is highly asymmetric while the transition $^2S^e \rightarrow 3p^5 3d\ (^1P) 4s\ ^2P^o$ in figure 3.4(a) has a nearly symmetric line shape; this occurs because the underlying continuum is so small for the $^2S^e$ initial state, a $4s \rightarrow \varepsilon p$ transition, as opposed to the much larger $3d \rightarrow \varepsilon f, \varepsilon p$ continuum cross section for the $^2D^e$ initial state.

Table 3.3: Theoretical and experimental resonance energies E_{res} (eV), widths Γ (mev) and the corresponding transitions.

This Calculation		Transition	Experiment	
E_{res}	Γ		E_{res}	Γ
29.89	143.5	$^2D^e \rightarrow 3p^5(3d^2\ ^1G)\ ^2F^o$	30.03	142
31.33	115.7	$^2D^e \rightarrow 3p^5(3d^2\ ^1D)\ ^2F^o$	31.66	116
34.25	64.5	$^2D^e \rightarrow (3p^5 3d\ ^3F)4s\ ^2F^o$	34.73	53
36.05	3.4	$^2D^e \rightarrow (3p^5 3d\ ^1F)4s\ ^2F^o$		
37.17	850.4	$^2D^e \rightarrow 3p^5(3d^2\ ^3F)\ ^2F^o$	37.13	847
44.04	8.6	$^2D^e \rightarrow (3p^5 3d\ ^3P)4d\ ^2P^o$		
44.07	75.5	$^2D^e \rightarrow (3p^5 3d\ ^3P)4d\ ^2F^o$		
32.75	46.1	$^2D^e \rightarrow (3p^5 3d\ ^3P)4s\ \ ^2P^o$	33.22	48
39.63	4.5	$^2D^e \rightarrow 3p^5(3d^2\ ^3P)\ ^2P^o$	39.63	4.6
42.00	6.5	$^2D^e \rightarrow 3p^5(3d^2\ ^1S)\ ^2P^o$		
36.81	4 5	$^2S^e \rightarrow 3p^5(3d^2\ ^3P)\ ^2P^o$		
39.18	6.5	$^2S^e \rightarrow 3p^5(4s^2\ ^1S)\ ^2P^o$	39.26	6.0
42.04	146.6	$^2S^e \rightarrow (3p^5 3d\ ^1P)4s\ ^2P^o$	41.80	148

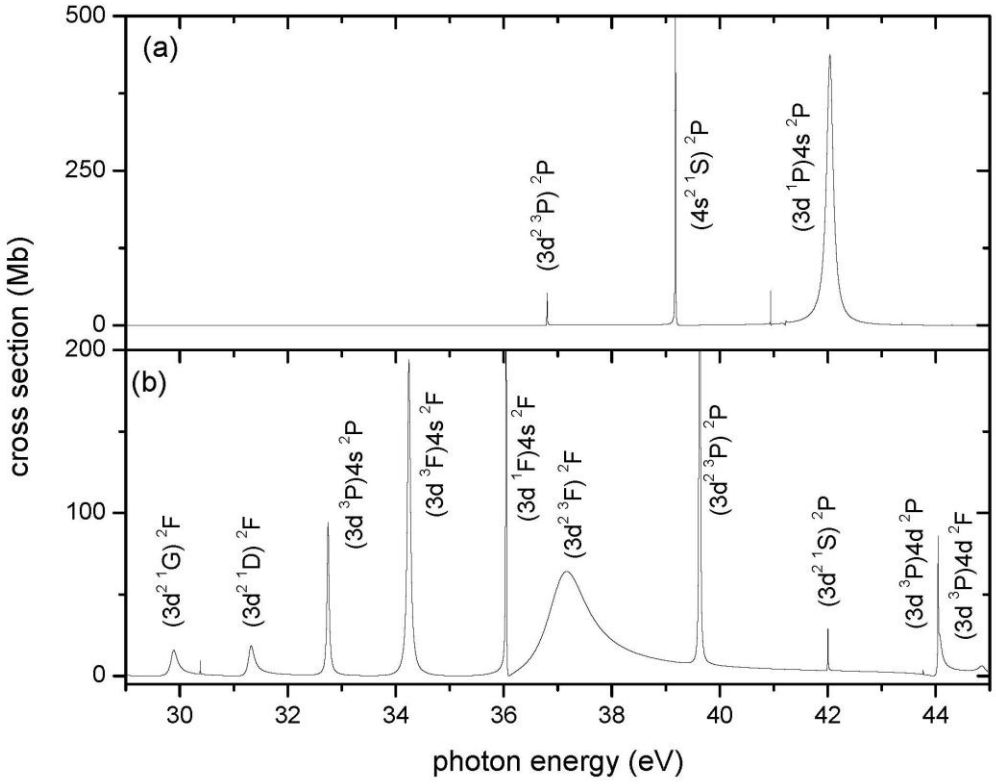

Figure 3.4: Calculated (LS) Sc^{+2} photoionization cross section and resonance identifications between 29 and 45 eV for (a), initial $^2S^e$ state, and (b), initial $^2D^e$ state. Both plots appear simpler than the experimental curves because of the absence of fine-structure splittings in these LS calculations. For simplicity $3p^5$ is omitted from each of the resonance designations,

3.2.2. Relativistic (Breit-Pauli) Calculations

When the spin-orbit interaction is considered, the experimental Sc^{+2} ion beam [9,10] consists of three components, presented in table 3.2: 24.7 % $^2S^e_{1/2}$, 20.7 % $^2D^e_{3/2}$ and 54.6 % $^2D^e_{5/2}$. In the nonrelativistic case, discussed above, the ^2D fractions were simply combined. These fractions are used to obtain the theoretical total photoionization cross section for Sc^{+2} for a meaningful comparison with experiment. The calculated

relativistic (Breit-Pauli) cross sections for the photoionization of the Sc^{+2} $^2S^e_{1/2}$ initial state is shown in figure 3.5. The individual $^2S^e_{1/2} \rightarrow {}^2P^o_{3/2}$ and $^2S^e_{1/2} \rightarrow {}^2P^o_{1/2}$ cross sections are presented in figures 3.5(a) and 3.5(b) respectively, while the total is given in figure 3.5(c). As in the non-relativistic case, the photoionization spectrum is dominated by autoionizing resonances. Among the most important resonances are $^2S^e_{1/2} \rightarrow 3p^5(4s^2\ ^1S)\ ^2P^o_{3/2}$ [figure 3.5(a)] and $^2S^e_{1/2} \rightarrow 3p^5(4s^2\ ^1S)\ ^2P^o_{1/2}$ [figure 3.5(b)] located at 39.01 and 39.52 eV respectively; experimentally [9,10], their positions are 39.26 and 39.77 eV, which means both resonances are shifted to lower energy by about 0.25 eV. These are among the largest deviations between theory and experiment found, in terms of resonance energies. However, the calculated relativistic energy splitting between these two resonances of 0.51 eV agrees exactly with experiment. Both resonances arise from the splitting of LS resonance shown in figure 3.4(a) at 39.18 eV, identified in LS-coupling as $^2S^e \rightarrow 3p^5(4s^2\ ^1S)\ ^2P^o$. Dominating the $^2S^e_{1/2}$ cross section, however, are clearly the giant $3p \rightarrow 3d$ resonances identified as $^2S^e_{1/2} \rightarrow (3p^5 3d\ ^1P)4s\ ^2P^o_{3/2}$ in figure 3.5(a) and $^2S^e_{1/2} \rightarrow (3p^5 3d\ ^1P)4s\ ^2P^o_{1/2}$ in figure 3.5(b); their positions and widths are 42.04 eV and 144 meV, and 42.06 eV and 138 meV, respectively. Although the relativistic interactions cause a splitting of these two resonances, the splitting is so much smaller than the widths that it is unobservable. Experimentally, the sum of these resonances is found at 41.80 eV with a width of 148 meV. Thus, the theoretical resonance energy is again too high by about 0.25 eV, but the width is in excellent agreement with experiment.

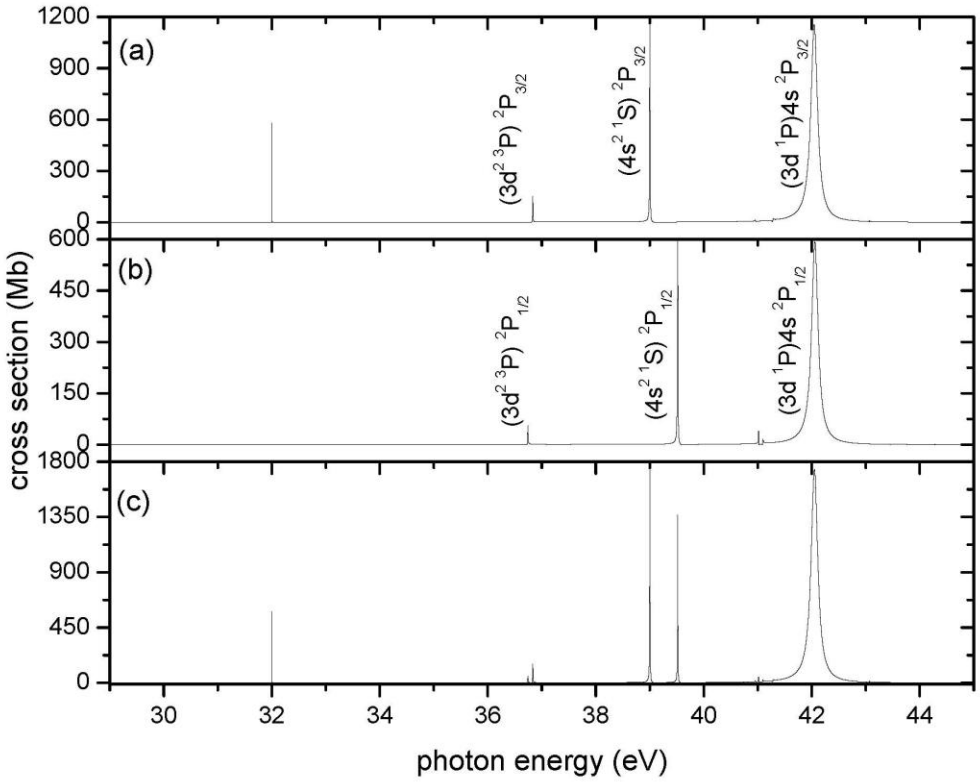

Figure 3.5: Calculated Breit-Pauli photoionization cross sections of the excited $^2S^e_{1/2}$ state of Sc^{+2} showing, (a) the partial cross section to the j=3/2 final state, (b) the partial cross section to the j=1/2 final state, and (c) the total $^2S^e_{1/2}$ cross section, dominated by the resonance at 42.04 eV. For simplicity $3p^5$ is omitted from each of the resonance designations.

The Breit-Pauli results for the photoionization of the ground $^2D^e_{3/2}$ state of Sc^{+2} are presented in figure 3.6. Note that, in the relativistic realm, L is no longer a good quantum number so that the final states of the system, the Sc^{+3} ion plus photoelectron, can be characterized only by total angular momentum, *j*, strictly speaking. Thus, from

the $^2D^e_{3/2}$ ground state, transitions to final states with j =5/2, 3/2 and 1/2 are allowed, and these cross sections are shown in figures 3.6(a), 3.6(b) and 3.6(c) respectively; the total $^2D^e_{3/2}$ photoionization cross section is shown in figure 3.6(d). Resonances are seen to dominate the cross section, although the direct nonresonant photoionization channel is strong enough for interference to occur and produce the asymmetric line shapes, Fano profiles, observed in the cross sections [figures 3.6(a) and 3.6(d)]. The most prominent resonance is located at 37.10 eV with 837 meV width, and it is due to transition $^2D^e_{3/2} \rightarrow 3p^5(3d^2\ ^3F)\ ^2F^o_{5/2}$. This decays *via* a super-Coster-Kronig transition ($3p^5 3d^2 \rightarrow 3p^6 + e^-$) that is also observed in the photoionization cross sections of the [Ne]$3s^2 3p^6 3d\ ^2D^e$ states of ground state Ti^{+3} [19,90-95] and metastable Ca^+ [19,93,96-102]; as long as the $3p \rightarrow 3d$ excitation energy is above the 3*d* threshold, this channel is open and results in this broad giant resonance. When the excitation energy is below the 3d ionization threshold, this decay channel is closed, and this is the case for K-like higher Z ions starting with V^{+4} (see next section). Our theoretical results show good agreement with experimental data [9,10] that place this resonance at 37.14 eV with 847 meV width. An illustration of the relativistic effects in the $^2D^e_{3/2}$ cross section is the splitting leading to the transitions $^2D^e_{3/2} \rightarrow 3p^5(3d^2\ ^3P)\ ^2P^o_{1/2}$ and $^2P^o_{3/2}$. at 39.59 eV [figure 3.6(c)] and 39.68 eV [figure 3.6(b)] respectively; both correspond to the LS-coupling transition $^2D^e \rightarrow 3p^5(3d^2\ ^3P)\ ^2P^o$ at 39.63 eV seen in figure 3.4(b).

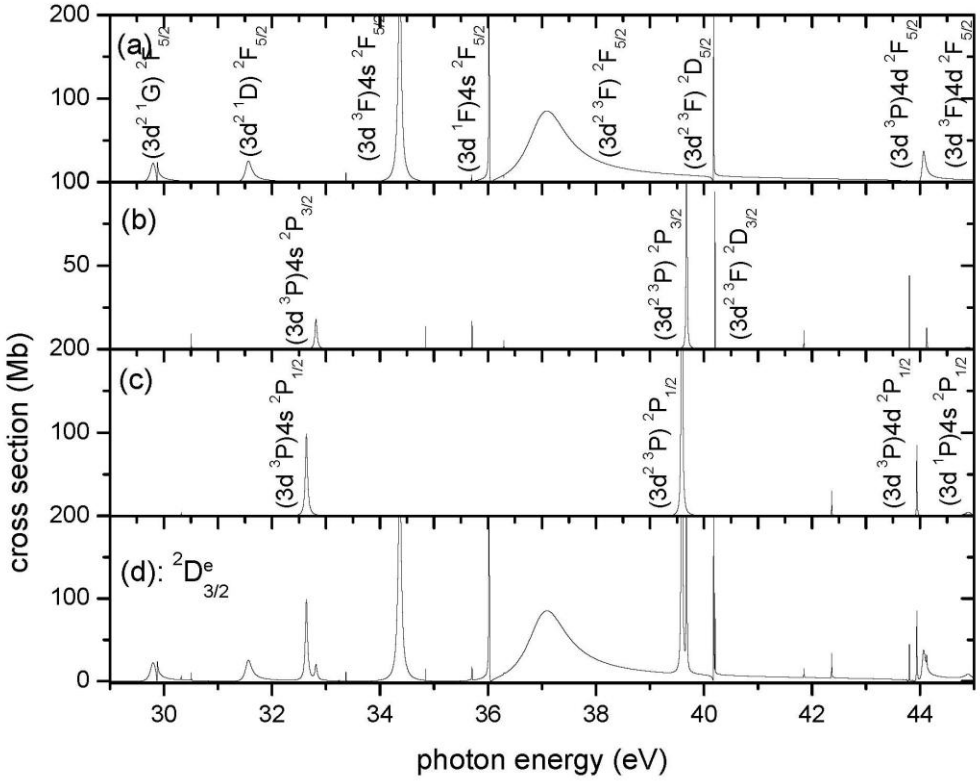

Figure 3.6: Calculated Breit-Pauli photoionization cross sections of the ground $^2D^e_{3/2}$ state of Sc^{+2} showing, (a) the partial cross section to the j=5/2 final state, (b) the partial cross section to the j=3/2 final state, (c) the partial cross section to the j=1/2 final state, and (d) the total $^2D^e_{3/2}$ cross section, dominated by the $3p^5(3d^2\ ^3F)\ ^2F^o_{5/2}$ resonance at 37.10 eV. For simplicity $3p^5$ is omitted from each of the resonance designations.

In figure 3.7, the calculated Breit-Pauli results for the corresponding photoionization cross section for the excited $^2D^e_{5/2}$ state, where the partial cross sections for j = 7/2, 5/2 and 3/2 final states are shown in figures 3.7(a), 3.7(b) and 3.7(c)

respectively. The total photoionization cross section for the $^2D^e_{5/2}$ initial state is shown in figure 3.7(d). The strongest resonance, located at 37.22 eV in figure 3.7 (a), and due to transition $^2D^e_{5/2} \rightarrow 3p^5(3d^2\ ^3F)\ ^2F^o_{7/2}$, has a width of 852.4 meV (847 meV experimentally); it is of substantially the same width as the corresponding $^2D^e_{3/2}$ resonance (837 meV width) in figures 3.6(a) and 3.6(d). Another noteworthy feature of the $^2D^e_{5/2}$ cross section is the relativistic (spin-orbit) splitting of LS resonances. To the LS-coupling transition $^2D^e \rightarrow (3p^5 3d\ ^3F)4s\ ^2F^o$, located at 34.24 eV in figure 3.4(b), correspond two relativistic transitions, $^2D^e_{5/2} \rightarrow (3p^5 3d\ ^3F)4s\ ^2F^o_{5/2}$, seen in figure 3.7(b) at 34.34 eV, and $^2D^e_{5/2} \rightarrow (3p^5 3d\ ^3F)4s\ ^2F^o_{7/2}$, seen in figure 3.7(a) at 34.11 eV. Additional fine structure splitting is illustrated in transitions $^2D^e_{5/2} \rightarrow 3p^5(3d^2\ ^3P)\ ^2P^o_{3/2}$ in figure 3.7(c) at 39.65 eV, and $^2D^e_{3/2} \rightarrow 3p^5(3d^2\ ^3P)\ ^2P^o_{3/2}$ in figure 3.6(b) at 39.68 eV; these transitions are due to the same resonance from different initial states. Thus the splitting is exactly the fine structure splitting between $^2D^e_{3/2}$ and $^2D^e_{5/2}$ which is 0.03 eV in this calculation (0.024 eV in the experiment [9,10]). A similar situation arises for the transitions to the $(3p^5 3d\ \ ^3P)4s\ ^2P^o_{3/2}$ resonance from the $^2D^e_{3/2}$ and $^2D^e_{5/2}$ initial states in figures 3.6(b) and 3.7(c); again these transitions are separated by 0.03 eV.

Note that, in the results of the relativistic calculations, the existence of the resonances identified as $^2D^e_{5/2} \rightarrow (3p^5 3d\ ^3D)4s\ ^2D^o_{5/2}$, seen in figure 3.7(b) at 36.26 eV, $^2D^e_{3/2} \rightarrow 3p^5(3d^2\ ^3F)\ ^2D^o_{5/2}$, seen in figure 3.6(a) at 40.18 eV, $^2D^e_{3/2} \rightarrow 3p^5(3d^2\ ^3F)\ ^2D^o_{3/2}$ seen in figure 3.6(b) at 40.20 eV and $^2D^e_{5/2} \rightarrow 3p^5(3d^2\ ^3F)\ ^2D^o_{5/2}$, seen in figure 3.7(b) at 40.15 eV, their narrow widths notwithstanding, those resonances mark an important

difference between relativistic and non-relativistic calculations. Specifically, they are forbidden in the nonrelativistic LS calculation because the $^2D^e \rightarrow {}^2D^o$ channel only opens at a photon energy of 54.48 eV. Below this energy, in the 29.0 to 45.0 eV range, the only open channels for the photoionization of the $3p^6 3d\ ^2$D initial state are $3p^6 \varepsilon p\ ^2$P and $3p^6 \varepsilon f\ ^2$F. As mentioned above, however, in the relativistic regime, L is no longer a good quantum number; only total angular momentum *j* is. Thus, the (LS-forbidden) $^2D_{3/2}$ and $^2D_{5/2}$ final states of the Sc^{+3} ion-plus-photoelectron system are not pure, but are mixed with the (LS-allowed) $^2P_{3/2}$ and $^2F_{5/2}$ respectively, i.e., mixed with allowed states of the same *j*. These resonances demonstrate that relativistic interactions affect the results beyond shifts and splittings of resonances and thresholds.

A summary of positions, widths and identifications of the major resonances obtained in the relativistic Breit-Pauli calculation is given in table 3.4, along with a comparison with available experimental data [9,10]. In general the agreement is quite good, especially for the $3p^5 3d^2$ resonances as regards both position and width. Note that some of the resonances listed in table 3.4 can be reached by more than one initial state in the experimental mixture, and one, $3p^5(3d^2\ ^3\text{P})\ ^2\text{P}^o_{3/2}$, can be excited from all three initial states. They are listed more than once for purposes of comparison with the experimental results, and they are listed at different photon arises simply because each of the three initial states has a different ionization energy so that differing photon energies are required from each of these initial states to excite a particular resonance, i.e., the difference in the resonance energies for a given resonance state in the table is just the difference in the binding energies of the initial states of the transitions.

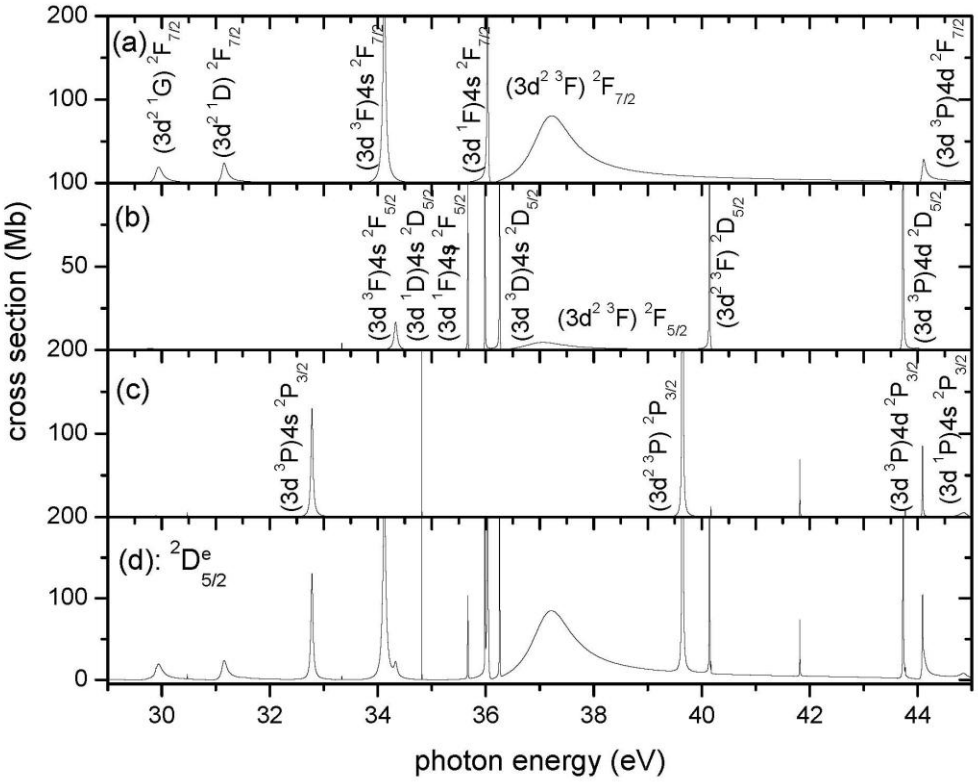

Figure 3.7: Calculated Breit-Pauli photoionization cross sections of the first excited $^2D^e_{5/2}$ state of Sc^{+2} showing, (a) the partial cross section to the j=7/2 final state, (b) the partial cross section to the j=5/2 final state, (c) the partial cross section to the j=3/2 final state, and (d) the total $^2D^e_{3/2}$ cross section, dominated by the $3p^5(3d^2\ ^3F)\ ^2F^o_{7/2}$ resonance at 37.22 eV. For simplicity $3p^5$ is omitted from each of the resonance designations.

Table 3.4: Theoretical (relativistic Breit-Pauli) and experimental resonance energies E_{res} (eV), widths Γ (meV) and the corresponding transitions.

This Calculation		Transitions	Experiment	
Γ	E_{res}		E_{res}	Γ
5.3	36.75	$^2S^e_{1/2} \rightarrow 3p^5(3d^2\ ^3P)\ ^2P^o_{1/2}$		
4.0	36.83	$^2S^e_{1/2} \rightarrow 3p^5(3d^2\ ^3P)\ ^2P^o_{3/2}$		
6.3	39.52	$^2S^e_{1/2} \rightarrow 3p^5(4s^2\ ^1S)\ ^2P^o_{1/2}$	39.77	6.0
7.1	39.00	$^2S^e_{1/2} \rightarrow 3p^5(4s^2\ ^1S)\ ^2P^o_{3/2}$	39.26	7.2
138.0	42.06	$^2S^e_{1/2} \rightarrow (3p^5 3d\ ^1P)4s\ ^2P^o_{1/2}$		
144.0	42.04	$^2S^e_{1/2} \rightarrow (3p^5 3d\ ^1P)4s\ ^2P^o_{3/2}$	41.80	148
44.9	32.64	$^2D^e_{3/2} \rightarrow (3p^5 3d\ ^3P)4s\ ^2P^o_{1/2}$	33.22	45
42.5	32.79	$^2D^e_{5/2} \rightarrow (3p^5 3d\ ^3P)4s\ ^2P^o_{3/2}$	33.37	48
42.3	32.82	$^2D^e_{3/2} \rightarrow (3p^5 3d\ ^3P)4s\ ^2P^o_{3/2}$		
5.3	39.59	$^2D^e_{3/2} \rightarrow 3p^5(3d^2\ ^3P)\ ^2P^o_{1/2}$	39.63	4.6
3.9	39.65	$^2D^e_{5/2} \rightarrow 3p^5(3d^2\ ^3P)\ ^2P^o_{3/2}$	39.69	3.8
3.9	39.68	$^2D^e_{3/2} \rightarrow 3p^5(3d^2\ ^3P)\ ^2P^o_{3/2}$	39.71	2.6
126.2	29.88	$^2D^e_{3/2} \rightarrow 3p^5(3d^2\ ^1G)\ ^2F^o_{5/2}$	30.03	142
149.6	29.95	$^2D^e_{5/2} \rightarrow 3p^5(3d^2\ ^1G)\ ^2F^o_{7/2}$	30.17	142
127.2	31.57	$^2D^e_{3/2} \rightarrow 3p^5(3d^2\ ^1D)\ ^2F^o_{5/2}$	31.66	116
101.5	31.16	$^2D^e_{5/2} \rightarrow 3p^5(3d^2\ ^1D)\ ^2F^o_{7/2}$	31.27	111
64.9	34.37	$^2D^e_{3/2} \rightarrow (3p^5 3d\ ^3F)4s\ ^2F^o_{5/2}$	34.73	53
63.1	34.13	$^2D^e_{5/2} \rightarrow (3p^5 3d\ ^3F)4s\ ^2F^o_{7/2}$	34.50	44
64.9	34.34	$^2D^e_{5/2} \rightarrow (3p^5 3d\ ^3F)4s\ ^2F^o_{5/2}$		
1.1	36.02	$^2D^e_{3/2} \rightarrow (3p^5 3d\ ^1F)4s\ ^2F^o_{5/2}$		
5.2	36.04	$^2D^e_{5/2} \rightarrow (3p^5 3d\ ^1F)4s\ ^2F^o_{7/2}$		

Table 3.4: (continued)

Γ	E_{res}		Γ	E_{res}
35.99	1.1	$^2D^e_{5/2} \rightarrow (3p^5 3d\ ^1F)4s\ ^2F^o_{5/2}$		
35.66	0.8	$^2D^e_{5/2} \rightarrow (3p^5 3d\ ^1D)4s\ ^2D^o_{5/2}$		
36.26	0.7	$^2D^e_{5/2} \rightarrow (3p^5 3d\ ^3D)4s\ ^2D^o_{5/2}$		
37.10	837.0	$^2D^e_{3/2} \rightarrow 3p^5(3d^2\ ^3F)\ ^2F^o_{5/2}$	37.13	847
37.22	852.4	$^2D^e_{5/2} \rightarrow 3p^5(3d^2\ ^3F)\ ^2F^o_{7/2}$		
37.07	837.0	$^2D^e_{5/2} \rightarrow 3p^5(3d^2\ ^3F)\ ^2F^o_{5/2}$		
44.06	71.6	$^2D^e_{3/2} \rightarrow (3p^5 3d\ ^3P)4d\ ^2F^o_{5/2}$		
44.11	75.5	$^2D^e_{5/2} \rightarrow (3p^5 3d\ ^3P)4d\ ^2F^o_{7/2}$		
43.73	8.1	$^2D^e_{5/2} \rightarrow (3p^5 3d\ ^3P)4d\ ^2D^o_{5/2}$		
44.09	8.3	$^2D^e_{5/2} \rightarrow (3p^5 3d\ ^3P)4d\ ^2P^o_{3/2}$		
44.84	148	$^2D^e_{5/2} \rightarrow (3p^5 3d\ ^1P)4s\ ^2P^o_{3/2}$		
43.94	2.1	$^2D^e_{3/2} \rightarrow (3p^5 3d\ ^3P)4d\ ^2P^o_{1/2}$		
40.18	0.7	$^2D^e_{3/2} \rightarrow 3p^5(3d^2\ ^3F)\ ^2D^o_{5/2}$	40.21	0.8
40.20	0.3	$^2D^e_{3/2} \rightarrow 3p^5(3d^2\ ^3F)\ ^2D^o_{3/2}$		
40.15	0.8	$^2D^e_{5/2} \rightarrow 3p^5(3d^2\ ^3F)\ ^2D^o_{5/2}$	40.19	0.9

Additional results to complete the Sc^{+2} resonance analysis are the list of line strengths and oscillator strengths for five of the major resonances chosen from table 3.4, and this is shown in table 3.5. As expected and can be seen in table 3.5, transitions with $\Delta j = 1$ ($^2D^e_{3/2} \rightarrow 3p^5(3d^2\ ^3F)\ ^2F^o_{5/2}$, $^2D^e_{5/2} \rightarrow 3p^5(3d^2\ ^3F)\ ^2F^o_{7/2}$ and $^2S^e_{1/2} \rightarrow (3p^5 3d\ ^1P)4s\ ^2P^o_{3/2}$) have stronger line strength and oscillator strength than transitions with $\Delta j = 0$ ($^2D^e_{5/2} \rightarrow 3p^5(3d^2\ ^3F)\ ^2F^o_{5/2}$ and $^2S^e_{1/2} \rightarrow (3p^5 3d\ ^1P)4s\ ^2P^o_{1/2}$).

Table 3.5: Sc III (Sc^{+2}) line strength (S) and oscillator strength (f) for five of the major resonances.

Transitions	Δj	S(a.u.)	f
$^2D^e_{3/2} \rightarrow 3p^5(3d^2\ ^3F)\ ^2F^o_{5/2}$	1	3.404	0.516
$^2D^e_{5/2} \rightarrow 3p^5(3d^2\ ^3F)\ ^2F^o_{7/2}$	1	4.323	0.550
$^2S^e_{1/2} \rightarrow (3p^5 3d\ ^1P)4s\ ^2P^o_{3/2}$	1	6.071	1.564
$^2D^e_{5/2} \rightarrow 3p^5(3d^2\ ^3F)\ ^2F^o_{5/2}$	0	0.204	0.031
$^2S^e_{1/2} \rightarrow (3p^5 3d\ ^1P)4s\ ^2P^o_{1/2}$	0	1.730	0.789

A very useful check upon the magnitude of photoionization cross sections is the Thomas-Reiche-Kuhn sum rule [75-78] which states that the sum of the oscillator strengths (integral over the continuum part) to all possible final states from a given initial state of an atom or atomic ion is exactly equal to the number of electrons in the initial state. It has also been found that the sum rule is true to an excellent approximation subshell by subshell [103]. Since the photoionization cross section is simply a multiplicative constant times the (differential) oscillator strength [103], the total oscillator strength represented by the photoionization cross section can be easily calculated. In the present case, it is expected that the cross section should include almost all of the strength from the $3p^6$ subshell owing to the giant $3p \rightarrow 3d$ resonances which all occur in the continuum; for the outer shell electron, on the other hand, most of the oscillator strength will likely occur in the discrete, i.e., photoexcitation rather than photoionization. Owing to these considerations, the total oscillator strength in the photoionization cross of Sc^{+2} from threshold to 68 eV should be a bit under 6, the number of $3p$ electrons. Our

calculated oscillator strength is 5.293, which is certainly of the correct magnitude. Performing the same calculation on the experimental results, we find a measured oscillator strength of 3.244, which is too low; we cannot account for the missing oscillator strength. Thus, we believe that the overall magnitude of the measured cross section is too small and should be multiplied by a factor of 5.293/3.244 = 1.632 to bring the oscillator strength to a reasonable value. In our comparison with experimental cross sections, therefore, we have used this modified experimental cross section.

The comparison between the two theoretical calculations (non-relativistic and relativistic) and the (modified) experimental data from 29 to 53.0 eV is shown in figure 3.8. The Breit-Pauli calculations [figure 3.8(b)] give good agreement with experimental data [9,10] [figure 3.8(c)] while the LS coupling calculations [figure 3.8(a)], in spite of the absence of fine structure splitting, give a fairly accurate idea about positions of major resonances in the cross section. The most important features of the Sc^{+2} photoionization experimental results [figure 3.8(c)] are well reproduced by the present Breit-Pauli calculations [figure 3.8(b)], although small deviations in some resonance positions remain.

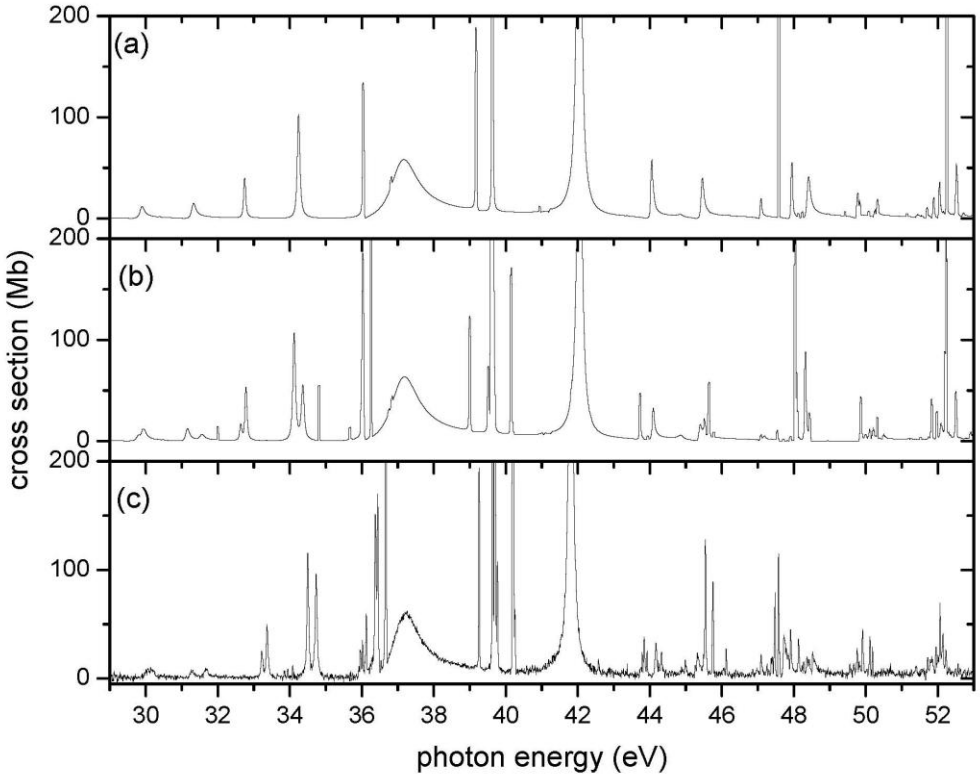

Figure 3.8: Sc^{+2} photoionization cross sections from 29 to 53.0 eV for a weighted average of $^2D^e$ and $^2S^e$ initial states; (a) theory (LS-coupling), (b) theory (relativistic Breit-Pauli), and (c) modified experiment [9,10]. The experimental cross section has been multiplied by a factor of 1.632 for reason discussed in text.

3.3. Conclusion

Photoionization calculations have been performed for Sc^{+2}, the simplest atomic system containing a *d*-electron in the ground state. The calculations have been carried out using the nonrelativistic (LS-coupling) and the relativistic (Breit-Pauli) *R*-matrix methods. Our results showed that the cross section is dominated by $3p \rightarrow 3d$ giant resonances. Rather good agreement was found between experiment and theory for the

positions and widths of the major resonances. The overall magnitudes of the experimental and theoretical cross sections differed considerably, and a sum rule analysis seemed to indicate that the experimental cross section was too small; multiplication by a factor of 1.632, indicated by the sum rule analysis, brought experiment and theory into quite good agreement.

The effects of relativistic interactions (notable the spin-orbit effect) were highlighted by comparison of the nonrelativistic and relativistic calculations. It was found that, in addition to shifts and splitting of various resonances, relativistic effects were important in that various transition that were forbidden at the LS-coupling level of calculation, became possible when relativistic interactions were introduced. Nevertheless, our results show that the non-relativistic *R*-matrix method using LS coupling, despite the exclusion of relativistic effects, is still reasonably good for investigating atomic processes such as photoionization at intermediate Z. However, relativistic (Breit-Pauli or Dirac) R-matrix is required for good quantitative agreement with experimental data. In the following section, we extend our calculations to other members of the Sc^{+2} isoelectronic sequence: Ti^{+3}, V^{+4}, Cr^{+5}, Mn^{+6} and Fe^{+7}.

CHAPTER 4.

PHOTOIONIZATION OF POTASSIUM-LIKE TRANSITION METAL IONS: Ti^{+3}, V^{+4}, Cr^{+5}, Mn^{+6} AND Fe^{+7}

4.1. Description of the Calculations

Calculations about each of the K-like transition metal ions (Ti^{+3}, V^{+4}, Cr^{+5}, Mn^{+6} and Fe^{+7}) are performed the same way as those of the Sc^{+2} ions described in the subsection 3.1. Therefore we will not repeat what is already said in that subsection, but we will report relevant results obtained in those calculations beginning with the target states energy levels and ionization threshold for each of the five K-like transition metal ions we are interested in here.

The target states energy levels (relative to the ground state energy level in each target ion) are shown in tables 4.1 through 4.5, and the five target (N-electron system) ions are Ti^{+4}, V^{+5}, Cr^{+6}, Mn^{+7} and Fe^{+8} which all have the same number of electrons (18) as Sc^{+3}. Our results (target state energy levels) are compared with experimental data from NIST [89], and reasonable agreement is obtained.

Table 4.1: Calculated and experimental (NIST) [89] energy levels in Rydbergs f6r states of Ti V (Ti^{+4}) relative to the ground state.

Ti V state	J	This work	Exp. [89]
$3s^2 3p^6\ {}^1S^e$	0	0.00000	0.00000
$3s^2 3p^5 3d\ {}^3P^o$	0	2.48367	2.50087
	1	2.49314	2.50937
	2	2.51236	2.52704
$3s^2 3p^5 3d\ {}^3F^o$	4	2.61161	2.61785
	3	2.62770	2.63401
	2	2.64390	2.64977
$3s^2 3p^5 3d\ {}^1D^o$	2	2.79307	2.79644
$3s^2 3p^5 3d\ {}^3D^o$	3	2.79831	2.80150
	1	2.80346	2.81811
	2	2.80676	2.81976
$3s^2 3p^5 3d\ {}^1F^o$	3	2.82873	2.83799
$3s^2 3p^5 3d\ {}^1P^o$	1	3.62858	3.60242
$3s^2 3p^5 4s\ {}^3P^o$	2	3.95653	3.95799
	1	3.98314	3.98086
	0	4.00869	4.01016
$3s^2 3p^5 4s\ {}^1P^o$	1	4.06424	4.04377

Table 4.2: Calculated and experimental (NIST) [89] energy levels in Rydbergs f6r states of V VI (V^{+5}) relative to the ground state.

V VI state	J	This work	Exp. [89]
$3s^2 3p^6\ {}^1S^e$	0	0.00000	0.00000
$3s^2 3p^5 3d\ {}^3P^o$	0	2.78103	2.80806
	1	2.79375	2.81941
	2	2.81965	2.84295
$3s^2 3p^5 3d\ {}^3F^o$	4	2.93927	2.94132
	3	2.95902	2.96123
	2	2.98018	2.98180
$3s^2 3p^5 3d\ {}^1D^o$	2	3.13522	3.14514
$3s^2 3p^5 3d\ {}^3D^o$	3	3.13776	3.14857
	1	3.15819	3.17929
	2	3.16395	3.17417
$3s^2 3p^5 3d\ {}^1F^o$	3	3.18936	3.19530
$3s^2 3p^5 3d\ {}^1P^o$	1	4.09529	4.05910
$3s^2 3p^5 4s\ {}^3P^o$	2	4.96331	4.97811
	1	4.99552	5.00577
	0	5.03216	5.04678
$3s^2 3p^5 4s\ {}^1P^o$	1	5.07103	5.08155

Table 4.3: Calculated and experimental (NIST) [89] energy levels in Rydbergs f6r states of Cr VII (Cr^{+6}) relative to the ground state.

Cr VII state	J	This work	Exp. [89]
$3s^2 3p^6\ {}^1S^e$	0	0.00000	0.00000
$3s^2 3p^5 3d\ {}^3P^o$	0	3.08740	3.10905
	1	3.10359	3.12358
	2	3.13659	3.15423
$3s^2 3p^5 3d\ {}^3F^o$	4	3.26237	3.25817
	3	3.28577	3.28212
	2	3.31244	3.30845
$3s^2 3p^5 3d\ {}^1D^o$	2	3.48487	3.48725
$3s^2 3p^5 3d\ {}^3D^o$	3	3.48439	3.48776
	1	3.51075	3.51592
	2	3.52008	3.52311
$3s^2 3p^5 3d\ {}^1F^o$	3	3.54768	3.54689
$3s^2 3p^5 3d\ {}^1P^o$	1	4.54066	4.49287
$3s^2 3p^5 4s\ {}^3P^o$	2	6.09112	6.09508
	1	6.12937	6.12761
	0	6.17853	6.18326
$3s^2 3p^5 4s\ {}^1P^o$	1	6.23461	6.22040

Table 4.4: Calculated and experimental (NIST) [89] energy levels in Rydbergs f6r states of Mn VIII (Mn^{+7}) relative to the ground state.

Mn VIII state	J	This work	Exp. [89]
$3s^2 3p^6\ {}^1S^e$	0	0.00000	0.00000
$3s^2 3p^5 3d\ {}^3P^o$	0	3.38869	3.40502
	1	3.40853	3.42372
	2	3.44898	3.46273
$3s^2 3p^5 3d\ {}^3F^o$	4	3.57785	3.57967
	3	3.60668	3.59878
	2	3.64054	3.63198
$3s^2 3p^5 3d\ {}^3D^o$	3	3.82429	3.82162
	1	3.86001	3.85773
	2	3.87317	3.86961
$3s^2 3p^5 3d\ {}^1D^o$	2	3.83193	3.82565
$3s^2 3p^5 3d\ {}^1F^o$	3	3.90310	3.89595
$3s^2 3p^5 3d\ {}^1P^o$	1	4.98231	4.91368
$3s^2 3p^5 4s\ {}^3P^o$	2	7.32145	
	1	7.36632	7.34572
	0	7.43203	
$3s^2 3p^5 4s\ {}^1P^o$	1	7.48992	7.45872

Table 4.5: Calculated and experimental (NIST) [89] energy levels in Rydbergs f6r states of Fe IX (Fe^{+8}) relative to the ground state.

Fe IX state	J	This work	Exp. [89]
$3s^2 3p^6\ {}^1S^e$	0	0.00000	0.00000
$3s^2 3p^5 3d\ {}^3P^o$	0	3.67965	3.69767
	1	3.70493	3.72084
	2	3.75661	3.76963
$3s^2 3p^5 3d\ {}^3F^o$	4	3.88917	3.88026
	3	3.92096	3.91216
	2	3.96265	3.95324
$3s^2 3p^5 3d\ {}^3D^o$	3	4.15474	4.15184
	1	4.19913	4.19744
	2	4.21974	4.21567
$3s^2 3p^5 3d\ {}^1D^o$	2	4.16740	4.16223
$3s^2 3p^5 3d\ {}^1F^o$	3	4.25345	4.24494
$3s^2 3p^5 3d\ {}^1P^o$	1	5.39438	5.32676
$3s^2 3p^5 4s\ {}^3P^o$	2	8.62148	
	1	8.67325	8.66159
	0	8.76097	
$3s^2 3p^5 4s\ {}^1P^o$	1	8.82007	8.79892

For each of those K-like transition metal ions, the final (N+1) electron system continuum wave function is expressed in the form shown in equation (13). In the first sum in equation (13), only the terms arising from 3 spectroscopic configurations ($3s^2 3p^6$, $3s^2 3p^5 3d$ and $3s^2 3p^5 4s$) are included which abnegates the possibility of pseudo-resonances; those 3 configurations give rise to 9 LS terms corresponding to 17 LSJ levels (see tables 4.1 through 4.5). In the (purely discrete) second sum, however, all of the terms from the 24 N-electron configurations, coupled to all of the single-particle orbitals, both spectroscopic and correlation, are included in the set of χ_i.

In table 4.6 are presented the threshold energies of the nonrelativistic states of each of the five K-like transition metal ions (Ti^{+3}, V^{+4}, Cr^{+5}, $Mn^{+6}$and Fe^{+7}), the $[Ne]3s^2 3p^6 3d\ ^2D^e$ state, along with the corresponding two relativistic initial states, the ground state $[Ne]3s^2 3p^6 3d\ ^2D^e_{3/2}$ plus the first (metastable) excited state $[Ne]3s^2 3p^6 3d\ ^2D^e_{5/2}$. For the Ti^{+3} ions particularly, we have a third relativistic initial state ($[Ne]3s^2 3p^6 4s\ ^2S^e_{1/2}$) that is added to these calculations. Comparing our theoretical ionization potentials with experimental data [89], also shown in the table, it is evident that agreement between theory and experiment is rather good.

Since this part of our work is about K-like transition metal ions (Ti^{+3}, V^{+4}, Cr^{+5}, Mn^{+6} and Fe^{+7}), it is interesting to see how the energy gap (fine structure splitting) between $^2D^e_{3/2}$ and $^2D^e_{5/2}$ levels changes as the nuclear charge Z of those ions increases along the sequence. In table 4.7, we present a comparison between calculated and experimental fine structure splitting (energy gap) corresponding to the two relativistic levels $^2D^e_{3/2}$ and $^2D^e_{5/2}$.

Table 4.6: K-like ions (Ti^{+3}, V^{+4}, Cr^{+5}, $Mn^{+6}$and Fe^{+7}) states threshold energy in eV compared to experiment [89].

Ions	State	Calculation	Experiment	% Difference
Ti^{+3}	$^2S^e_{1/2}$	33.356	33.300	0.168
	$^2D^e$	43.281	43.243	0.087
	$^2D^e_{3/2}$	43.317	43.267	0.117
	$^2D^e_{5/2}$	43.257	43.220	0.085
V^{+4}	$^2D^e$	65.248	65.242	0.009
	$^2D^e_{3/2}$	65.293	65.281	0.018
	$^2D^e_{5/2}$	65.199	65.204	0.007
Cr^{+5}	$^2D^e$	90.646	90.576	0.077
	$^2D^e_{3/2}$	90.718	90.635	0.091
	$^2D^e_{5/2}$	90.581	90.518	0.069
Mn^{+6}	$^2D^e$	119.118	119.120	0.016
	$^2D^e_{3/2}$	119.218	119.203	0.012
	$^2D^e_{5/2}$	119.027	119.037	0.008
Fe^{+7}	$^2D^e$	151.029	150.956	0.048
	$^2D^e_{3/2}$	151.146	151.070	0.050
	$^2D^e_{5/2}$	150.883	150.843	0.026

Table 4.7: Calculated and experimental [89] fine structure splitting energy gap ΔE (eV) between $^2D^e_{3/2}$ and $^2D^e_{5/2}$ levels for K-like ions (Sc^{+2}, Ti^{+3}, V^{+4}, Cr^{+5}, Mn^{+6} and Fe^{+7}).

Ions	Z	Calculated ΔE	Experimental ΔE
Sc^{+2}	21	0.030	0.024
Ti^{+3}	22	0.059	0.047
V^{+4}	23	0.094	0.077
Cr^{+5}	24	0.137	0.117
Mn^{+6}	25	0.191	0.166
Fe^{+7}	26	0.263	0.227

4.2. Results and Discussion

Among transition metal ions of the potassium isoelectronic sequence (Ti^{+3}, V^{+4}, Cr^{+5}, Mn^{+6} and Fe^{+7}) studied in this chapter, the Ti^{3+} is the most extensively investigated experimentally and theoretically [19,90-95] because of the presence, in the photoionization cross section spectra, of the giant ($3p \rightarrow 3d$ excitation) resonances as it was observed in Sc^{+2} case studied previous chapter; in consequence we first report on the photoionization cross sections of Ti^{3+} with non-relativistic and relativistic calculations. We must note, concerning the photoionization of Ti^{+3}, that existing theoretical and experimental works have reached good agreement especially the two recent calculations (Gorczyca *et al* [94] and Eissner *et al* [95]) showed excellent agreement with experiment [19]; however both theoretical works are limited to the lower photon energy region (threshold to 45.3 eV) while the energy range in the experiment was from threshold to 49.5 eV.

4.2.1. Photoionization of Ti^{+3} Ions

4.2.1.1. Non-relativistic (LS coupling) Calculations

In the non-relativistic calculations of Ti^{+3} ions, the initial states of this ion are represented by the ground [Ne]$3s^2 3p^6 3d\ ^2D^e$ and the first excited [Ne]$3s^2 3p^6 4s\ ^2S^e$ states. In figures 4.1 and 4.2, we present results of the non-relativistic calculations for photon energy from 3*d* electron threshold (43.28 eV) to 83.0 eV, and figures 4.1 shows the photoionization cross sections from threshold to 51.0 eV while figure 4.2 is about 51.0 to 83 eV. Figures [4.1(a) and 4.2(a)] and [4.1(b) and 4.2(b)] respectively illustrate the individual photoionization cross sections from excited $^2S^e$ and ground $^2D^e$ states of Ti^{+3}; since, in both cases, the photoionization cross sections obtained using length and velocity forms agree very well, only one form (length) is displayed here and in all subsequent figures.

In the Ti^{+3} excited $^2S^e$ state, the 4*s* electron ionization (33.35 eV) threshold cross section (not seen in figure 4.1(a)) is 0.695 Mb. For photon energy below 45.0 eV [figure 4.1(a)], there are no resonances in the excited $^2S^e$ state photoionization cross section; only the direct photoionization process is possible here, and leads to [$(3s^2 3p^6\ ^1S^e)\ \varepsilon p$] $^2P^o$ final state of the (N+1) electron system. Above 45.0 eV, we enter the 3*p* electron excitation region characterized by the presence of series of Rydberg resonances associated with 3*p* electron photoexcitation [figures 4.1(a) and 4.2(a)] such as [$(3p^5 nd)\ 4s\ ^2P^o$] and [$(3p^5 n's)\ 4s\ ^2P^o$]. These two sequences of Rydberg resonances contains the most important features of the Ti^{3+} excited $^2S^e$ state photoionization cross sections spectrum [figure 4.1(a)], among them, we note the resonance located at 48.62 eV (with 18.5 meV

width), and attributed to transition $^2S^e \rightarrow 3p^5(4s^2\ ^1S)\ ^2P^o$ and the remarkably large and broad resonance feature in figure 4.1(a) at 49.09 eV (with 186.4 meV width); this peak reaches 1556 Mb, and is attributed to transition $^2S^e \rightarrow (3p^5 3d\ ^1P)4s\ ^2P^o$ that is followed by autoionization (decay) to the ground $3s^2 3p^6\ ^1S^e$ state of Ti^{+4}. Figure 4.2(a) displays higher order members of those rydberg series of resonances originated from 3*p* electron photoexcitation to higher principal quantum numbers [$(3p^5 nd)\ 4s\ ^2P^o$] and [$(3p^5 n's)\ 4s\ ^2P^o$] with $n \geq 4$ and $n' \geq 5$. They are mixed, and decay to the [$(3s^2 3p^6\ ^1S^e)\ \varepsilon p\ ^2P^o$] continuum. The limit of those two sequences is the excited target Ti^{+4} ($3p^5 4s\ ^1P^o$) state at energy 98.55 eV (98.23 eV from experiment [89]). Due to dipole transition selection rules, only the transition $^2S^e \rightarrow\ ^2P^o$ is allowed; this confers to the outer 4*s* electron, in this photoionization of Ti^{+3} excited $^2S^e$ state case, a role of "spectator" since it only contributes to angular momentum coupling with its spin. The very limited number of resonances observed in this case is illustrative of this fact.

For the ground $^2D^e$ state of Ti^{+3}, the photoionization cross sections in figures [4.1(b) and 4.2(b)] exhibit far more complex structure than the excited $^2S^e$ state of Ti^{+3}. At the threshold (43.28 eV), the cross section is 56.0 Mb [figure 4.1(b)]; for photon energy in the vicinity of the threshold the cross section is a mixture of direct nonresonant and indirect resonance processes, and it is evident that the resonance excitations are dominant in this region where the cross section can reach hundreds of Mb. For photon energy up to 51 eV [figure 4.1(b)], the cross section is dominated by giant, $3p \rightarrow 3d$ resonances; these $3p \rightarrow 3d$ resonances are so strong because they represent $\Delta n=0$ transitions, and, since the spatial extent of a wave function is determined largely by the principal quantum number, n, the 3*p* and 3*d* wave functions occupy substantially the

same region of space, resulting in significant overlap and a rather large dipole matrix element. The photoionization cross section in this region is dominated by resonances which decay *via* autoionizing processes leading to the ground $3s^2 3p^6\ {}^1S^e$ state of Ti^{+4}. In this region, the direct photoionization contribution to the cross section is quite small; thus the giant resonances are fairly symmetric since any asymmetry is due to interference between the resonant and nonresonant amplitudes. The direct photoionization cross section for the outer 3*d* electron, has been calculated [104] for Ti^{3+} at 45 eV to be 2.2 Mb, more than an order of magnitude smaller than the present result for the total (direct and indirect photoionization cross sections) of about 27.0 Mb (30.0 Mb experimentally [19]. Among the most prominent resonances in figure 4.1(b) are the resonance at the threshold (located at energy 43.64 eV with a width of 1.27 eV), indentified as the $^2D^e \rightarrow 3p^5(3d^2\ {}^3F)\ {}^2F^o$ transition, the resonance at 44.59 eV (41.8 meV width) identified as $^2D^e \rightarrow (3p^5 3d\ {}^3P)4s\ {}^2P^o$ and the resonance at 47.73 3V (5.9 meV width) attributed to $^2D^e \rightarrow 3p^5(3d^2\ {}^3P)\ {}^2P^o$. are the dominant resonances originating from 3*p* photoexcitation; they are the lowest members of the series of Rydberg resonances start from the threshold and continue to the higher energy region [figure 4.2(b)] with higher principal quantum numbers. Examples of the higher members of these series of Rydberg resonance, [$(3p^5 nd$) $3d\ {}^2P^o$, $^2F^o$] and [$(3p^5 n's\ {}^3P^o)\ 3d\ {}^2P^o$, $^2F^o$] with $n \geq 3$ and $n' \geq 4$ are displayed in both figures 4.1(b) and 4.2(b).

The series of Rydberg resonances interfere with direct photoionization continua $3s^2 3p^6\ {}^1S^e$ (εf, εp), and converge to the six Ti^{+4} $3s^2 3p^5 3d$ thresholds starting with $^3P^o$ at a photon energy of 77.16 eV to $^1P^o$ at 92.62 eV (92.23 eV from experiment [89]). In the region above 77.16 eV [figure 4.2(b)], the photon energy is high enough to produce,

through resonance excitation followed by autoionization, both ground and excited states of Ti^{+4} including $3s^2 3p^6\ {}^1S^e$, $3s^2 3p^5 3d\ {}^3P^o$, $3s^2 3p^5 3d\ {}^3F^o$, etc., i.e., ionization plus excitation; the continuum cross sections (direct process) comprise $3s^2 3p^6\ {}^1S^e$ (εf, εp), $3s^2 3p^5 3d\ {}^3P^o$ (εd, εs), $3s^2 3p^5 3d\ {}^3F^o$ (εd, εs) and so forth.

It is noteworthy that most of the characteristics of the Ti^{3+} photoionization cross sections spectrum originate from the ejection of the 3*d* electron (or 4*s* for the excited state), leading to the ground state of the target, $3s^2 3p^6\ {}^1S^e$. Up to a photon energy of 77.16 eV, only this channel is open; consequently other channels play minor roles in defining the photoionization cross section in the energy range considered in this work, at least for the LS coupling calculations part: threshold to 88.0 eV. Figure 4.3 is illustrative of the importance of the main line $3s^2 3p^6\ {}^1S^e$ [figure 4.3(c)] compared to the satellite lines $3s^2 3p^5 3d\ {}^3P^o$ and $3s^2 3p^5 3d\ {}^3F^o$ [figures 4.3(b) and 4.3(a)] in the photoionization cross sections of the ground $[Ne]3s^2 3p^6 3d\ {}^2D^e$ of Ti^{+3}. Note particularly the vertical scales of figures 4.3(a) and 4.3(b) as compared to figure 4.3(c).

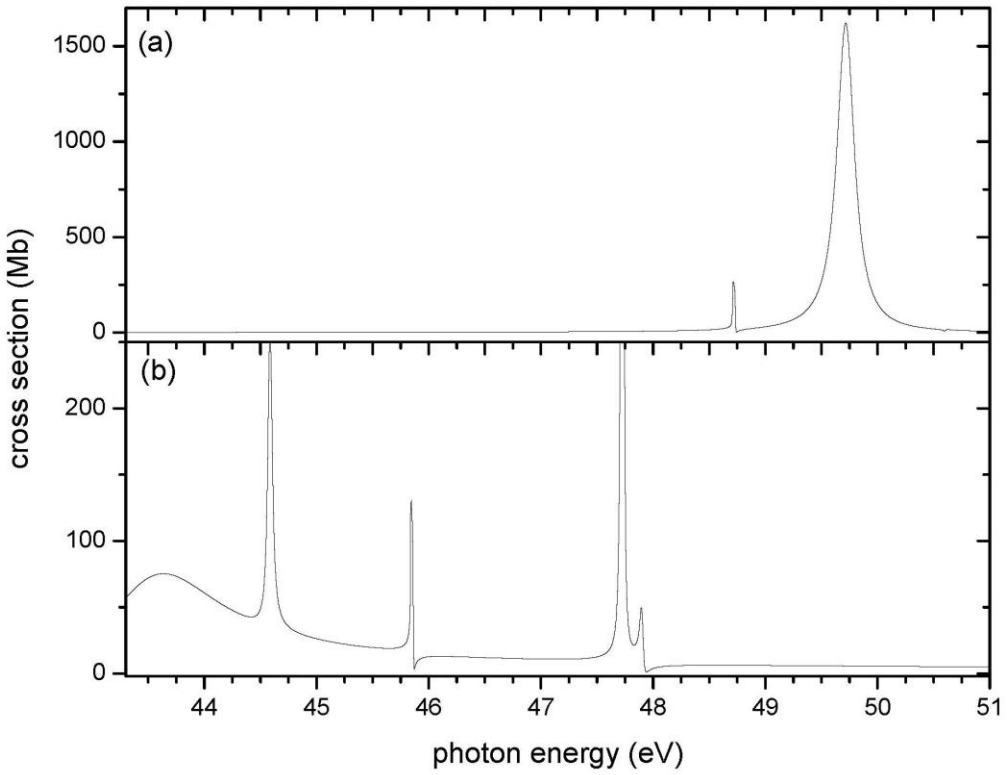

Figure 4.1: Calculated photoionization cross sections of Ti^{+3} from threshold to 51.0 eV: (a) initial $^2S^e$ excited state showing the strongest resonance $^2S^e \rightarrow (3p^5 3d\ ^1P)4s\ ^2P^o$ at energy 49.09 eV and (b) initial $^2D^e$ ground state showing the strongest resonance $^2D^e \rightarrow 3p^5(3d^2\ ^3F)\ ^2F^o$ at energy 43.64 eV. Note the cut-off in resonance structure at threshold in (b).

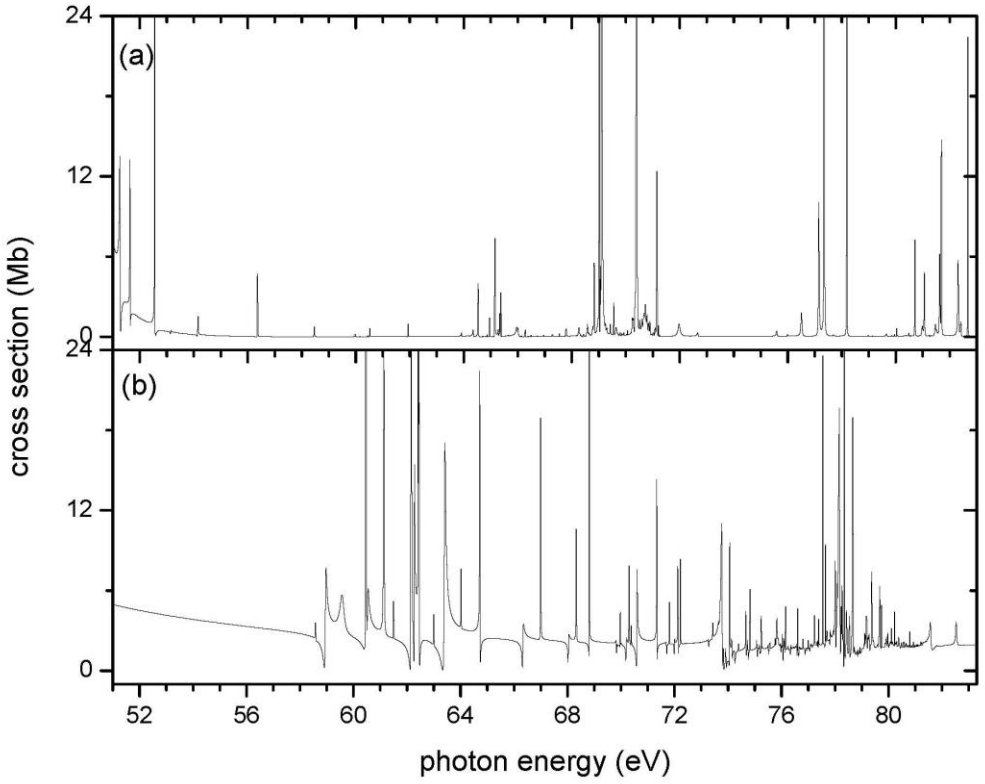

Figure 4.2: Calculated photoionization cross sections of Ti^{+3} from 51.0 to 83.0 eV: (a) initial $^2S^e$ excited state showing the rydberg series of resonances [($3p^5nd\ ^1P^o$) $4s\ ^2P^o$] and [($3p^5n's\ ^1P^o$) $4s\ ^2P^o$] with $n \geq 4$ and $n' \geq 5$ and (b) initial $^2D^e$ ground state showing series of Rydberg resonances [($3p^5nd$) $3d\ ^2P^o$, $^2F^o$] and [($3p^5n's\ ^3P^o$) $3d\ ^2P^o$, $^2F^o$] with $n \geq 4$ and $n' \geq 5$.

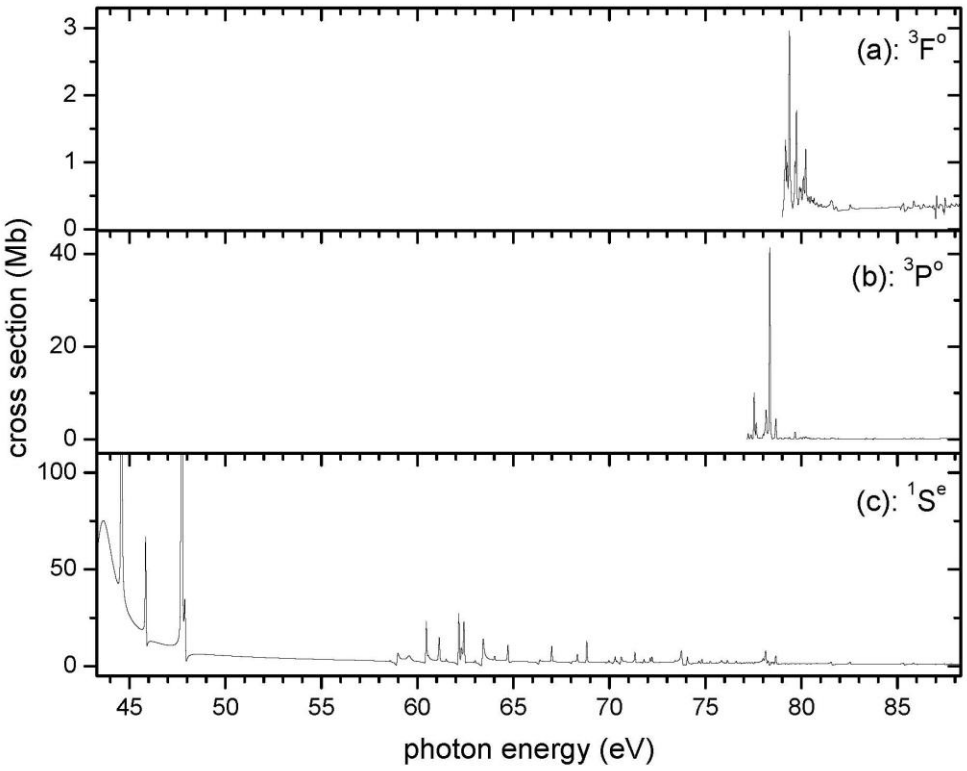

Figure 4.3: Calculated photoionization cross section of the ground [Ne]$3s^2 3p^6 3d$ $^2D^e$ initial state for the satellite transitions leaving the Ti^{+4} ion in the (a) $3s^2 3p^5 3d$ $^3F^o$ excited state and (b) $3s^2 3p^5 3d$ $^3P^o$ excited state, along with (c) the main line transition to the $3s^2 3p^6$ $^1S^o$ ground state of Ti^{+4}.

The photoelectron angular distributions asymmetry parameter beta (β) dependence on energy is presented in figure 4.4 for both the ground [Ne]$3s^2 3p^6 3d$ $^2D^e$ and the excited [Ne]$3s^2 3p^6 4s$ $^2S^e$ states of Ti^{+3} ions. Figure 4.4(a) shows the asymmetry parameter β for the excited [Ne]$3s^2 3p^6 4s$ $^2S^e$ state, and as we can see there is no energy-dependence here since $\beta = 2$. This can be understood by the fact, in non-relativistic calculations (LS coupling approach), $\beta = 2$ for $s \rightarrow p$ transition; the variation of β with energy requires at least two outgoing channels with differing energy dependences to interfere with one another [85]. The photoionization of [Ne]$3s^2 3p^6 4s$ $^2S^e$ state leads to one final state only: [$(3s^2 3p^6$ $^1S^e)$ εp $^2P^o$]. The asymmetry parameter β dependence on energy can be clearly seen in figure 4.4(b) where we are presenting the case of the ground [Ne]$3s^2 3p^6 3d$ $^2D^e$ of Ti^{+3}. This is a non-relativistic operation, therefore Photoionization of the $^2D^e$ state involves 2 transitions ($d \rightarrow p$ and $d \rightarrow f$) leading to final states[$(3s^2 3p^6$ $^1S^e)$ εp $^2P^o$] and [$(3s^2 3p^6$ $^1S^e)$ εf $^2F^o$]; since we have at least two channels, β is energy dependent [figure 4.4(b)].

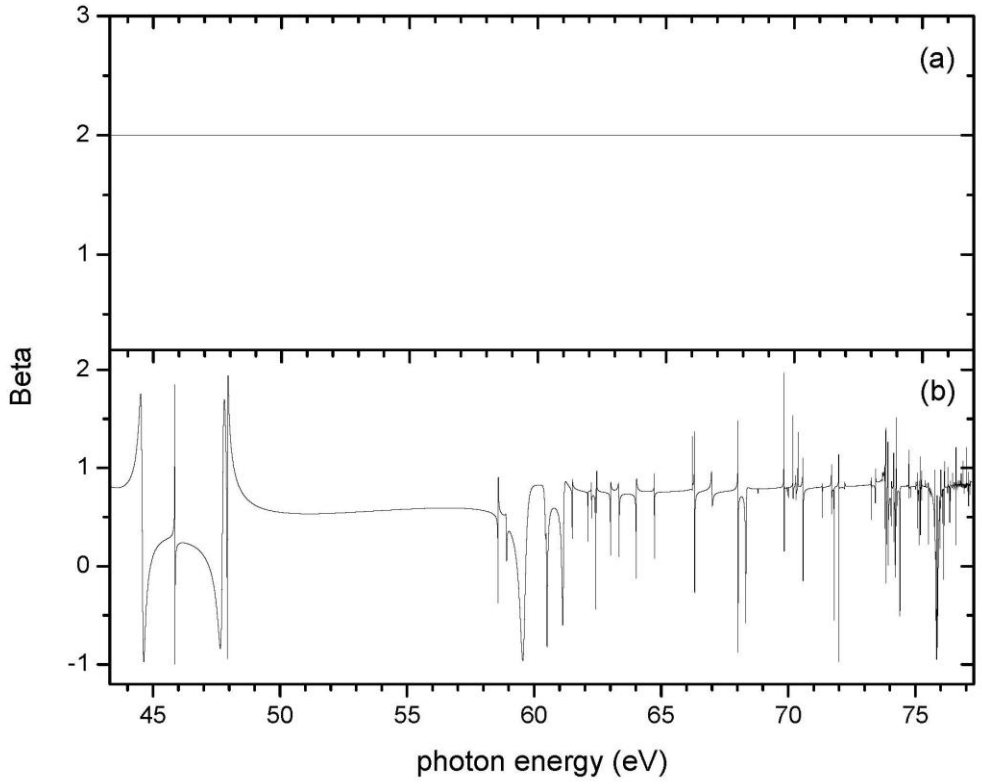

Figure 4.4: Calculated Ti^{+3} asymmetry parameter beta (p) curves for photon energy from threshold to 77.0 eV: (a) initial $^2S^e$ excited state showing $\beta = 2$ for $s \rightarrow p$ transition and (b) initial $^2D^e$ ground state showing β energy dependence for $d \rightarrow p$ and $d \rightarrow f$ transitions.

In figure 4.5 we show comparison between our LS results and the experimental data from Schippers *et al* [19] for photon energies from 43.3 to 49.5 eV for the ground $^2D^e$ initial state. The theoretical results have been broadened by a 18.0 meV width Gaussian to account for experimental resolution. The unique strongest and broadest resonance of Ti^{+3} ground state ($^2D^e$ symmetry) is located at 43.64 eV, as seen in figure 4.5(a). Experimental results [19] showed this resonance was positioned at 43.46 eV (see

figure 4.5(b). Since this calculation is a non-relativistic operation (LS coupling), relativistic effects, such as fine-structure splitting, are not included, and the absence of the spin-orbit interaction term in the calculation can be observed in figure 4.5(a) where the theoretical photoionization cross section spectrum doesn't show any splitting, and looks far simpler than the experimental counterpart in figure 4.5(b). We can compare, at this effect, the single superimposed resonance feature at 44.58 eV, due to transition $^2D^e \rightarrow (3p^5 3d\ ^3P)\ 4s\ \ ^2P^o$, in figure 4.5(a) to the double superimposed resonance structures that are observed at 44.42 and 44.61 eV respectively in figure 4.5(b). It is clear, from this early comparison between non-relativistic results and experimental data [19] shown in figure 4.5, that the introduction of relativistic effect with the Breit-Pauli calculations is necessary to reproduce experimental results. Not only do those relativistic effects allow the introduction of spin-orbit interaction leading to fine structure splitting, but also the dipole transition $^2D^e \rightarrow {}^2D^o$ can be accounted for in our theoretical results since, for the range of photon energy considered in the Ti^{+3} experiment [19] (threshold to 49.5 eV), this transition is forbidden in LS coupling approach. The striking difference between figures 4.5(a) and 4.5(b) in the energy region 47.5 to 48 eV is a concrete illustration of the influence of relativistic effects through the allowed transition $^2D^e \rightarrow {}^2D^o$.

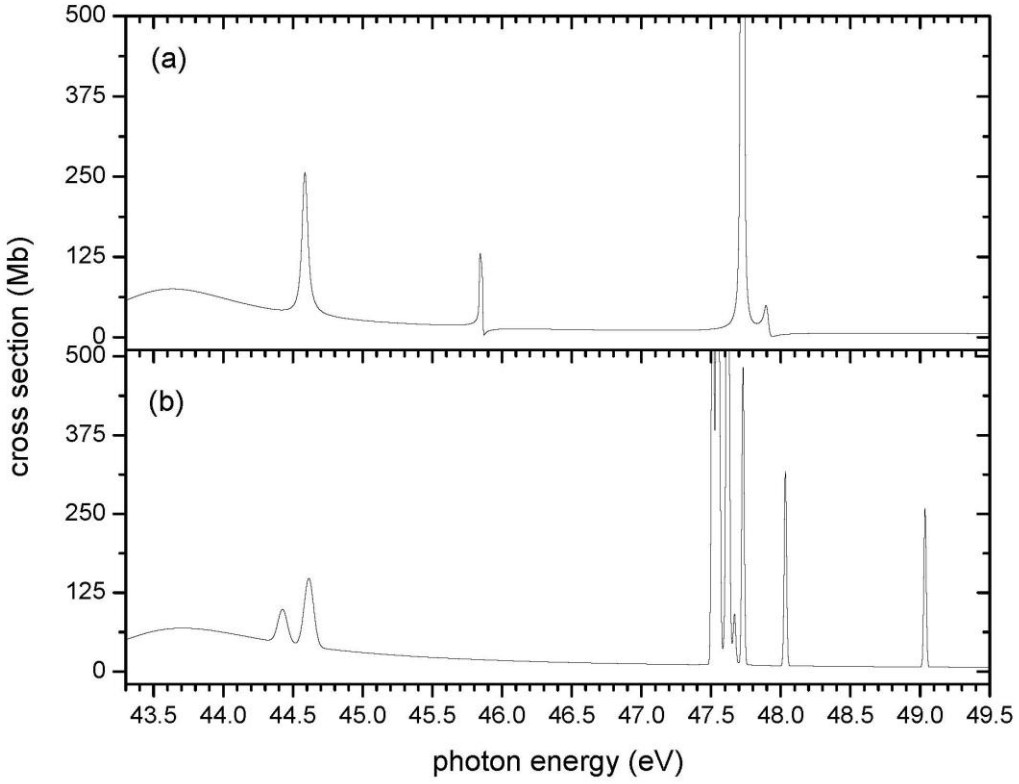

Figure 4.5: Ti^{+3} photoionization cross sections from 43.3 to 49.5 eV for the ground $^2D^e$ initial state; (a) theory (LS-coupling) and (b) experiment (Schippers *et al* [19]). Note the difference between the two spectra due to the absence of the spin-orbit interaction and the possibility of $^2D^e \rightarrow {}^2D^o$ transition from the theoretical calculation.

4.2.1.2. Relativistic (Breit-Pauli) Calculations

With the introduction of the spin-orbit interaction in our calculations with the use of the Breit-Pauli *R*-matrix method, initial states of the Ti^{3+}ion are represented by the ground $[Ne]3s^2 3p^6 3d\ ^2D^e_{3/2}$ state, the first excited $[Ne]3s^2 3p^6 3d\ ^2D^e_{5/2}$ state and the second excited $[Ne]3s^2 3p^6 4s\ ^2S^e_{1/2}$ state. The calculated relativistic (Breit-Pauli) cross

sections for the photoionization of Ti^{+3} in the excited $^2S^e_{1/2}$ initial state is shown in figure 4.6. The individual $^2S^e_{1/2} \rightarrow {}^2P^o_{3/2}$ and $^2S^e_{1/2} \rightarrow {}^2P^o_{1/2}$ cross sections are presented in figures 4.6(a) and 4.6(b) respectively, while the total is given in figure 4.6(c).

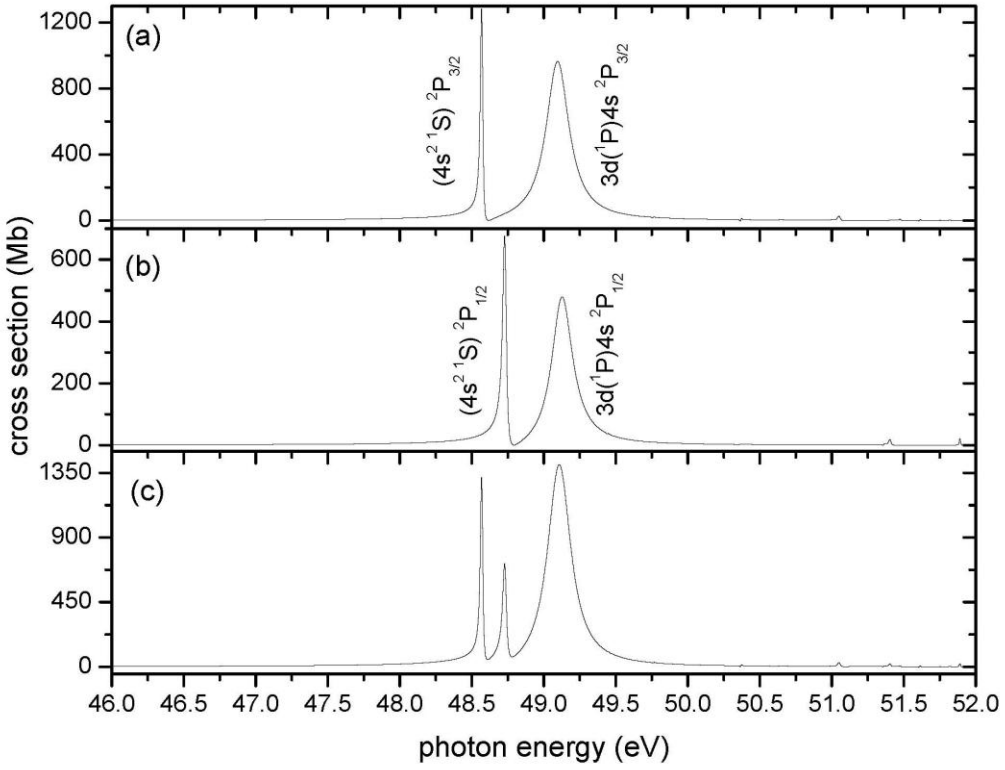

Figure 4.6: Calculated Breit-Pauli photoionization cross sections of the excited $^2S^e_{1/2}$ state of Ti^{+3} from 46.0 to 52.0 eV showing, (a) the partial cross section to the j=3/2 final state, (b) the partial cross section to the j=1/2 final state, and (c) the total $^2S^e_{1/2}$ cross section, dominated by the resonance at 49.09 eV. For simplicity $3p^5$ is omitted from each of the resonance designations.

As in the non-relativistic case, the photoionization spectrum is dominated by autoionizing resonances. Among important resonances in figure 4.6 note the very narrow resonances due to transitions $^2S^e_{1/2} \rightarrow 3p^5(4s^2\ ^1S)\ ^2P^o_{3/2}$ [figure 4.6(a)] and $^2S^e_{1/2} \rightarrow 3p^5(4s^2\ ^1S)\ ^2P^o_{1/2}$ [figure 4.6(b)] located at 48.57 eV (5.2 meV width) and 48.73 eV (26.9 meV width) respectively. Both resonances arise from the splitting of LS resonance shown in figure 4.1(a) at 48.62 eV (see above), identified in LS-coupling as $^2S^e \rightarrow 3p^5(4s^2\ ^1S)\ ^2P^o$. Dominating the $^2S^e_{1/2}$ cross section, however, are clearly the giant $3p \rightarrow 3d$ resonances identified as $^2S^e_{1/2} \rightarrow (3p^5 3d\ ^1P)4s\ ^2P^o_{3/2}$ in figure 4.6(a) and $^2S^e_{1/2} \rightarrow (3p^5 3d\ ^1P)4s\ ^2P^o_{1/2}$ in figure 4.6(b); their positions and widths are 49.09 eV and 192.7 meV, and 49.12 eV and 175.2 meV, respectively. Although the relativistic interactions cause a splitting of these two resonances, the splitting is so much smaller than the widths that it is unobservable. In the experiment conducted by Schippers *et al* [19], on the photoionization of Ti^{3+}, the excited $^2S^e_{1/2}$ state was not part of the target beam because it is significantly excited (by 9.96 eV) compared to the ground $^2D^e_{3/2}$ state, while in the case of Sc^{2+} the $^2S^e_{1/2}$ state was part of the target beam because it is only 3.16 eV above the ground $^2D^e_{3/2}$ state [9,10]. In the experiment on the photoionization of Ti^{3+} reported by Ryabtsev *et al* [92], however, the excited $^2S^e_{1/2}$ state was included as part of the target. From this experiment, resonances, originating from transitions $^2S^e_{1/2} \rightarrow 3p^5(4s^2\ ^1S)\ ^2P^o_{3/2}$ [figure 4.6(a)] and $^2S^e_{1/2} \rightarrow 3p^5(4s^2\ ^1S)\ ^2P^o_{1/2}$ [figure 4.6(b)], were found at 48.64 and 48.69 eV (24.8 meV width for each of them) respectively; it is clear that our theoretical results (48 55 and 48.73 eV) are in rather good agreement with the experimental data

from Ryabtsev *et al* [92] for those particular resonances. For the strongest and broadest resonance feature in the excited Ti^{3+} $^2S^e$ state photoionization cross section, the two spin-orbit components of the $^2S^e \rightarrow (3p^5 3d\ ^1P)4s\ ^2P^o$, there are no experimental or previous theoretical results to compare with. However we can say that both resonances are just equivalent to one single resonance attributed to transition $^2S^e \rightarrow (3p^5 3d\ ^1P)4s\ ^2P^o$, and this resonance was observed in photoionization of the ground $[Ne]3s^2 3p^6 4s\ ^2S^e_{1/2}$ state of Ca^+ [19,93,96-102] and in the excited $[Ne]3s^2 3p^6 4s\ ^2S^e_{1/2}$ state of Sc^{+2} [9-11,93], and in each of those cases, this resonance is very broad and strong with respective positions 33.19 eV and 41.80 eV (experimental data [19,93]). Consequently, from Ca^+ to Sc^{+2}, this resonance position, compared to the 4s electron ionization threshold (11.87 eV in Ca^+ and 21.59 eV in Sc^{2+}), changes from 21.32 to 20.21 eV [19,93]. This tendency in the resonance position to get closer and closer to the 4s electron threshold, as the nuclear charge Z increases, should continue with Ti^{3+} and higher Z potassium-like ions; our theoretical calculations places it at 15.74 eV from the 4*s* electron threshold (33.35 eV). The width of this specific resonance, on the contrary, increases from Ca^+ to Sc^{+2} (92.0 and 147 meV); our calculated width (this work) is about 193.0 meV; which is in agreement with the trend in resonance width to augment as the nuclear charge Z of those ions increases. this strong $^2S^e \rightarrow (3p^5 3d\ ^1P)4s\ ^2P^o$ transition has an oscillator strength [103] in our calculation of 2.17 out of a total oscillator strength for 3*p* photoabsorption of 6, i.e., this transition accounts for about 36.17 % of the total 3*p* oscillator strength, an enormous contribution.

The Breit-Pauli results for the photoionization of the ground $^2D^e_{3/2}$ state of Ti^{+3} are presented in figure 4.7 for photon energy from threshold to 49.5 eV. From the $^2D^e_{3/2}$

ground state, transitions to final states with j =5/2, 3/2 and 1/2 are allowed, and these cross sections are shown in figures 4.7(a), 4.7(b) and 4.7(c) respectively; the total $^2\mathrm{D}^e_{3/2}$ photoionization cross section is shown in figure 4.7(d). For photon energy between the 3*d* ionization threshold (43.31 eV) and 49.5 eV, resonances are seen to dominate the cross section, although the direct nonresonant photoionization channel is strong enough for interference to occur and produce the asymmetric line shapes, Fano profiles, observed in the cross sections [figures 4.7(a) and 4.7(d)]. The most prominent resonance is located at 43.544 eV with 1.28 eV width, and it is due to the $^2\mathrm{D}^e_{3/2} \rightarrow 3p^5(3d^2\ ^3\mathrm{F})\ ^2\mathrm{F}^o_{5/2}$ transition, a $\Delta j = 1$ transition. This resonance decays *via* a super-Coster-Kronig [105,106] transition ($3p^5 3d^2 \rightarrow 3p^6 + e^-$) that is also observed in the photoionization cross sections of the excited (metastable) [Ne]$3s^2 3p^6 3d\ ^2\mathrm{D}^e$ states of Ca^+ [19,93,96-102] and the ground [Ne]$3s^2 3p^6 3d\ ^2\mathrm{D}^e$ state of Sc^{+2} [9-11,19,93,107,108]; as long as the excitation energy is above the 3*d* threshold, this channel is open and results in this broad giant resonance. When the excitation energy is below the 3*d* ionization threshold, this decay channel is closed, and this is the case for K-like higher Z ions starting with V^{4+} (see below). Our theoretical results show good agreement with experimental data [19] that place this resonance at 43.460 eV with 1.5 eV width. We note that, compared to the 3*d* electron ionization threshold, the experimental positions of this resonance are [19,93] 19.16 eV in metastable Ca^+, 12.38 eV in ground state Sc^{2+} and 0.22 eV in Ti^{3+}; our calculations (this work), show it at positions 19.17, 12.44 and 0.31 eV respectively, which is rather good agreement.

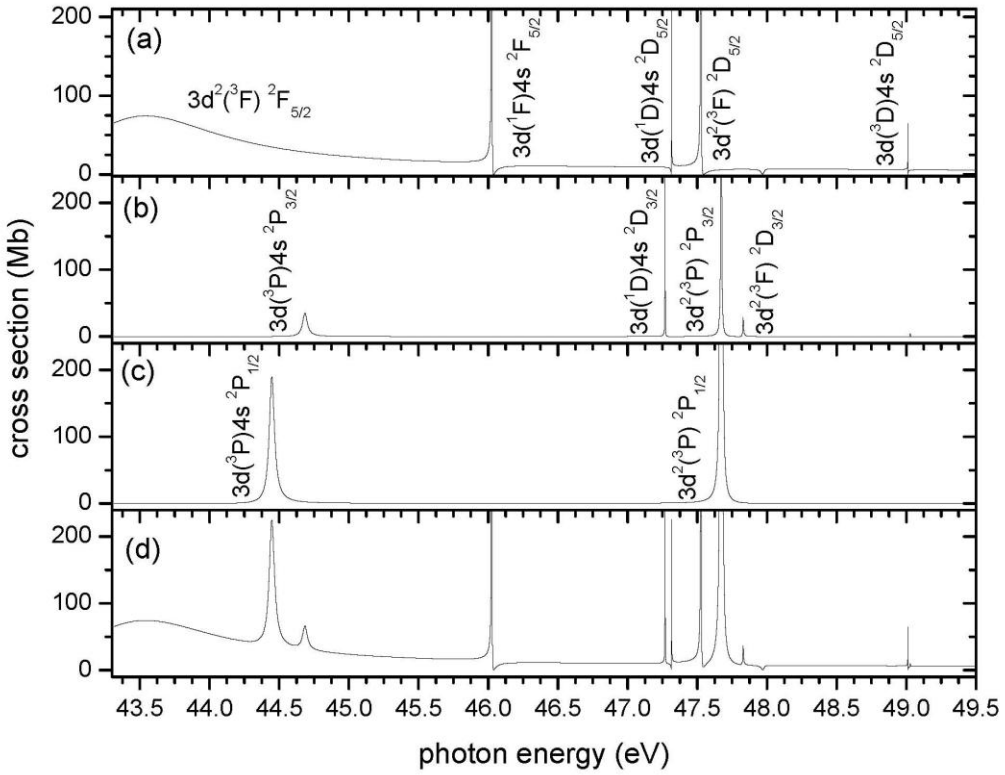

Figure 4.7: Calculated Breit-Pauli photoionization cross sections of the ground $^2\mathrm{D}^e_{3/2}$ state of Ti^{+3} showing, (a) the partial cross section to the j=5/2 final state, (b) the partial cross section to the j=3/2 final state, (c) the partial cross section to the j=1/2 final state, and (d) the total $^2\mathrm{D}^e_{3/2}$ cross section, dominated by the $3p^5(3d^2\ ^3\mathrm{F})\ ^2\mathrm{F}^o_{5/2}$ resonance at 43.54 eV. For simplicity $3p^5$ is omitted from each of the resonance designations.

Other important resonances in the photoionization $^2\mathrm{D}^e_{3/2}$ state of Ti^{3+} include the $^2\mathrm{D}^e_{3/2} \rightarrow (3p^5 3d\ ^3\mathrm{P})4s\ ^2\mathrm{P}^o_{1/2}$ (Δj = -1) located at 44.453 eV (44.4 meV width), seen in

figure 4.7(c), and the $^2D^e_{3/2} \rightarrow (3p^5 3d\ ^3P)4s\ \ ^2P^o_{3/2}$ (Δj = 0) resonance at 44.688 eV (40.4 meV width), seen in figure 4.7(b). Note the weakness of the $^2P^o_{3/2}$ resonance in terms of strength and width compared to the $^2P^o_{1/2}$ resonance. Additional resonances resulting from $^2D^e_{3/2}$ photoionization include $^2D^e_{3/2} \rightarrow 3p^5(3d^2\ ^3P)\ ^2P^o_{1/2}$ at 47.681 eV (4.3 meV width) shown in figure 4.7(c), $^2D^e_{3/2} \rightarrow 3p^5(3d^2\ ^3P)\ ^2P^o_{3/2}$ at 47.676 eV (6.1 meV width) seen in figure 4.7(b), $^2D^e_{3/2} \rightarrow 3p^5(3d^2\ ^3F)\ ^2D^o_{5/2}$ located at 47.531 eV (1.4 meV width) in figure 4.7(a), and $^2D^e_{3/2} \rightarrow (3p^5 3d\ ^3F)4s\ ^2F^o_{5/2}$ at 46.030 eV (3.5 meV width) in figure 4.7(a). Note that the $^2D^e \rightarrow\ ^2D^o$ photoionizing transitions are forbidden in this energy range without the introduction of relativistic effects; there is no $^2D^o$ continuum since the ionization of the 3*d* electron leads only to $^2P^o$ and $^2F^o$ continua.

In figure 4.8, we present the calculated Breit-Pauli results for the corresponding photoionization cross section for the excited $^2D^e_{5/2}$ from threshold to 49.5 eV, and the partial cross sections for *j* = 7/2, 5/2 and 3/2 final states are shown in figures 4.8(a), 4,8(b) and 4.8(c) respectively. The total photoionization cross section for the $^2D^e_{5/2}$ initial state is shown in figure 4.8(d). The strongest resonance, located at 43.718 eV [figure 4.8 (a)], $^2D^e_{5/2} \rightarrow 3p^5(3d^2\ ^3F)\ ^2F^o_{7/2}$, has a width of 1.3 eV (1.5 eV experimentally); it is of substantially the same width as the corresponding $^2D^e_{3/2}$ resonance (1.28 eV) at 43.544 eV [figure 4.7(a)]. Most resonances seen in figure 4.8 for the $Ti^{+3}\ ^2D^e_{5/2}$ cross sections have their equivalent already listed in the case of Ti^{+3} $^2D^e_{3/2}$ discussed above; among then are $^2D^e_{5/2} \rightarrow 3p^5(3d^2\ ^3F)\ ^2F^o_{5/2}$ seen at 43.484 eV [figure 4.8(b)] with Δj = 0, $^2D^e_{5/2} \rightarrow (3p^5 3d\ ^3P)4s\ \ ^2P^o_{3/2}$ (Δj = -1) located at 44.628 eV

[figure 4.8(c)] and $^2D^e_{5/2} \rightarrow 3p^5(3d^2\ ^3P)\ ^2P^o_{3/2}$ at 47.616 eV [figure 4.8(c)]. Another example of $\Delta j = 0$ but with $\Delta L = 0$, $^2D^e_{5/2} \rightarrow 3p^5(3d^2\ ^3F)\ ^2D^o_{5/2}$ is seen in figure 4.8(b) at 47.471 eV. Further, there are $^2D^e_{5/2} \rightarrow (3p^5 3d\ ^1F)4s\ ^2F^o_{5/2}$ at 47.917 eV (23.7 meV width) [figure 4.8(b)] and $^2D^e_{5/2} \rightarrow (3p^5 3d\ ^1F)4s\ ^2F^o_{7/2}$ at 47.910 eV [figure 4.8(a)] (26.3 meV width). The fine structure splitting between the $^2D^e_{3/2}$ and $^2D^e_{5/2}$ states of Ti^{+3} ions, which is calculated to be $\Delta E = 0.060$ eV (experimental value is 0.047 eV [19,89]), is mirrored in the various resonance energy differences: $^2D^e_{3/2} \rightarrow 3p^5(3d^2\ ^3F)\ ^2F^o_{5/2}$ at 43.544 eV in figure 4.7(a) and $^2D^e_{5/2} \rightarrow 3p^5(3d^2\ ^3F)\ ^2F^o_{5/2}$ at 43.488 eV in figure 4.8(b), $^2D^e_{3/2} \rightarrow (3p^5 3d\ ^3P)4s\ \ ^2P^o_{3/2}$ at 44.688 eV in figure 4.7(b) and $^2D^e_{5/2} \rightarrow (3p^5 3d\ ^3P)4s\ ^2P^o_{3/2}$ at 44.628 eV in figure 4.8(c) and $^2D^e_{3/2} \rightarrow 3p^5(3d^2\ ^3P)\ ^2P^o_{3/2}$ at 47.676 eV in figure 4.7(b) and $^2D^e_{5/2} \rightarrow 3p^5(3d^2\ ^3P)\ ^2P^o_{3/2}$ at 47.616 eV in figure 4.8(c).

The experimental Ti^{+3} ion beam [19] consists of two components: 45.0 % $^2D^e_{3/2}$ and 55.0 % $^2D^e_{5/2}$, and these fractions are used to obtain the theoretical total photoionization cross section for Ti^{+3} for a meaningful comparison with experiment [19].

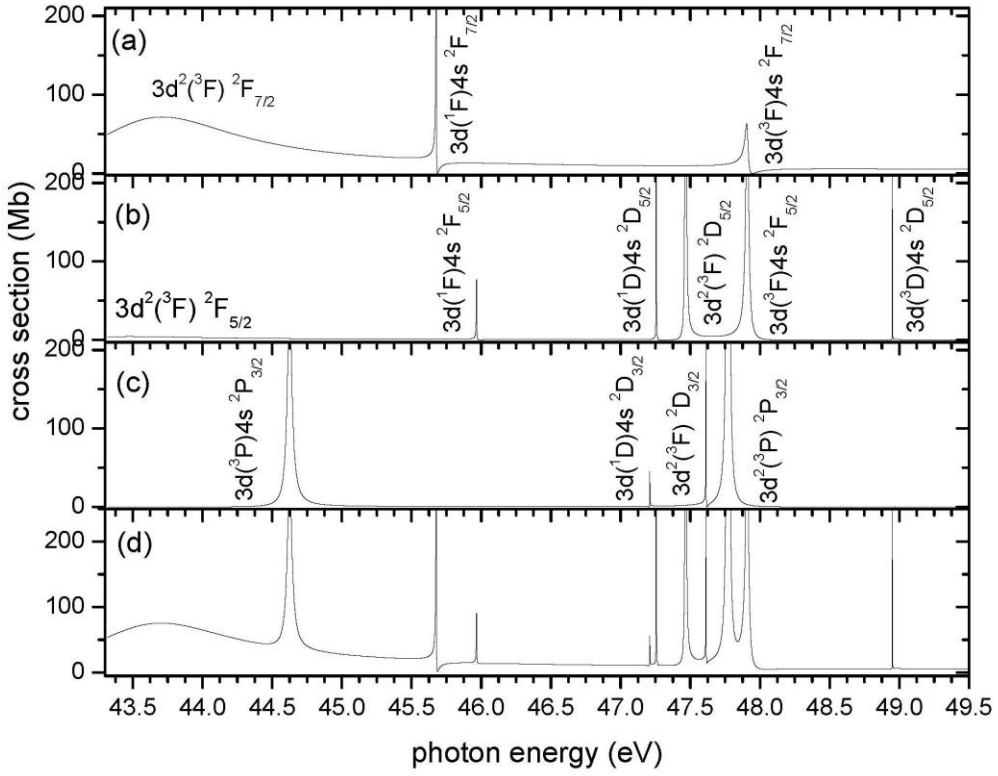

Figure 4.8: Calculated Breit-Pauli photoionization cross sections of the ground $^2D^e_{5/2}$ state of Ti^{+3} showing, (a) the partial cross section to the j=7/2 final state, (b) the partial cross section to the j=5/2 final state, (c) the partial cross section to the j=3/2 final state, and (d) the total $^2D^e_{5/2}$ cross section, dominated by the $3p^5(3d^2\ ^3F)\ ^2F^o_{7/2}$ resonance at 43.71 eV. For simplicity $3p^5$ is omitted from each of the resonance designations.

The comparison between theoretical and experimental data is shown in figure 4.9. The experimental photon energy range is from the 3*d* ionization threshold to 49.5 eV; this means the experiment [19] only involves the region of giant resonances. Those resonances, originating from $3p \rightarrow 3d$ and $3p \rightarrow 4s$ excitations, have been largely investigated theoretically and experimentally [19,90-95]. In figure 4.9, it is seen that the main feature of both theoretical and experimental cross section is the strongest and broadest resonance at the threshold, and attributed to the giant dipole transition $^2D^e \rightarrow 3p^5(3d^2\ ^3F)\ ^2F^o$. Despite the fact that this resonance is truncated (some of it is below the ionization threshold), it is still stronger than what was observed in excited (metastable) Ca^+ [19,93] and ground state of Sc^{+2} [19,93]. The width of this resonance is 1.5 eV experimentally [19,93] (1.3 eV in the present work), while for the metastable state of Ca^+ and the ground state of Sc^{2+}, corresponding widths are 0.324 eV and 0.847 eV respectively [19,93]. The loss of strength in this resonance in Ti^{3+}, due to truncation at the threshold, was estimated by Ryabtsev *et al* [19,92] to be about 40 %.

Comparing our theoretical results and experimental data, shown in figure 4.9, good agreement between them is seen. For example, the calculation for the large resonance at threshold exhibits a maximum of 74.04 Mb at 43.62 eV [figure 4.9(a)] while from experiment ([figure 4.9(b)], [19]), the maximum is 68.86 Mb at 43.70 eV, quite good agreement indeed; well within the experimental uncertainty of 15 %. Another illustration of the good agreement between theory (this work) and experiment [19] are the two narrower resonance structures that are superimposed on the giant resonance located theoretically at 44.45 and 44.62 eV [figure 4.9(a)], while the experiment [21] places them at 44.42 and 44.61 eV respectively [figure 4.9(b)].

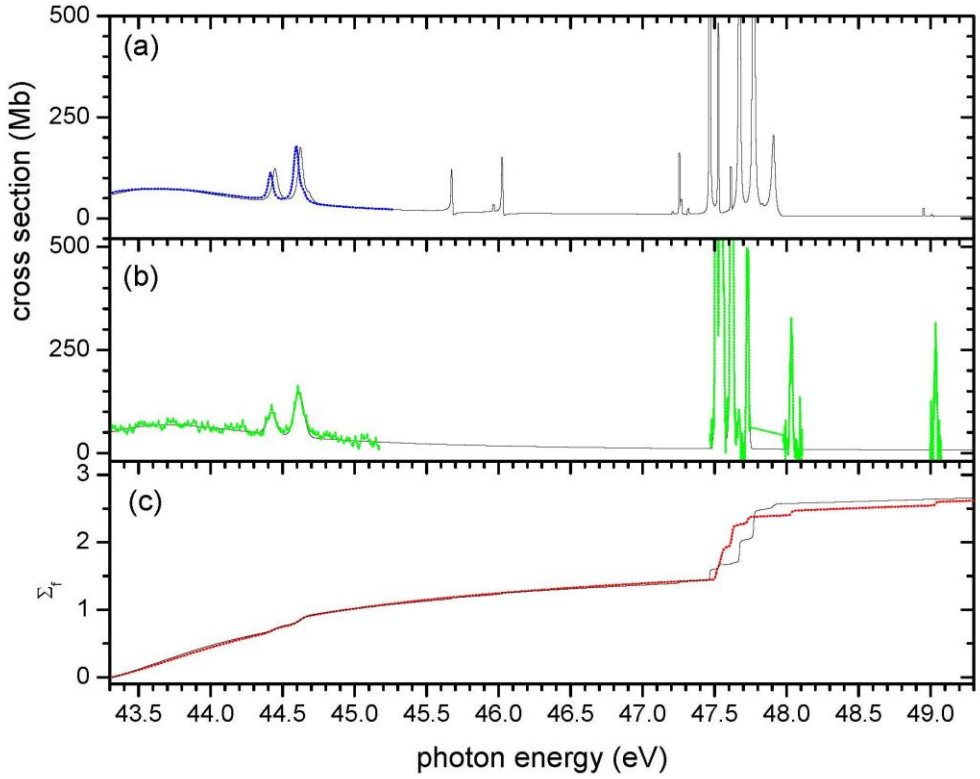

Figure 4.9: Ti^{3+} photoionization cross sections from 43.30 to 49.50 eV for a weighted average of $^2D^e_{3/2}$ and $^2D^e_{5/2}$ initial states; (a) theoretical calculations showing Nikolic *et al* [94] results (blue short dots) and results from this work (black solid line), (b) experiment [19] showing measured cross section data (green short dots) with error bars (low energy region) and the result of a resonance fit comprising eleven individual resonances (solid line), and (c) comparison of oscillator strength sums between this work (solid line) and experiment (red dotted line). Note the cut off, at the threshold, of the giant $3p^5(3d^2\ ^3F)\ ^2F^o$ dipole resonance in figures (a) and (b).

Despite this good agreement in the low energy region between the present work and experiment [19] (figure 4.9), very small differences between theory [figure 4.9(a)] and experiment [figure 4.9(b)] are seen in the 47.50 to 47 eV photon energy region, in terms of resonance positions, where the largest deviation observed is 0.16 eV only. Another less important difference between theory (this work) and experimental data [19] shown in figure 4.9(b) is the fact that cross section measurements were not performed in the energy ranges 45.1685- 47.4667 eV, 47.7484- 47.9757 eV and 48.1085- 48.9978 eV. This explains why, in the photon energy region from 45.6 to 46.1 eV, the two small resonance features seen at 45.68 and 46.03 eV (with respective widths 3.8 and 3.4 meV) in figure 4.9(a) were not part of experimental [19] results [figure 4.9(b)]. However, the experiment of Ryabtsev *et al* [92] showed similar resonance features with almost the same widths (4.3 and 3.7 meV), but there are deviations in the resonance positions (see table 4.8 below) compared to our results.

As what was done in the Sc^{+2} photoionization cross section case in the subsection 3.2.2, we can apply the Thomas-Reiche-Kuhn sum rule [75-78] to the Ti^{+3} photoionization case; Note it is also an excellent approximation for subshell photoionization [103]. Since the photoionization cross section is simply a multiplicative constant times the (differential) oscillator strength [39], the total oscillator strength represented by the photoionization cross section can be easily calculated. In the present case, it is expected that the cross section should include almost all of the strength from the $3p^6$ subshell owing to the giant $3p \rightarrow 3d$ resonances which all occur in the continuum; for the outer shell electron, on the other hand, most of the oscillator strength will likely occur in the discrete, i.e., photoexcitation rather than photoionization. Performing

oscillator strength calculations on Ti^{3+} within the experiment [19] photon energy range (from threshold to 49.5 eV), we find 2.810 out of possible 6 (number of 3*p* electrons); the measured oscillator strength is 2.631, in quite good agreement with theory. The theoretical and experimental results respectively represent about 47.0 % and 44.0 % of the total 3*p* oscillator strength even though the photon energy range is from threshold to 49.5 eV (6.2 eV wide); through those considerations, we confirm the important contribution of those giant dipole resonances to the sum of oscillator strengths in the photoionization of Ti^{3+}.

Continuing our discussion about photoionization of Ti^{+3} ions, in figure 4.9(c) we can see the progression of theoretical (the present work) in solid line and experimental [19] sums of oscillator strength (dotted line) as function of photon energy. Figure 4.9(c) reveals that theoretical results (the present work) and experimental data [19], for the photoionization cross sections of Ti^{+3}, agree very well until photon energy 47.40 eV where theoretical photoionization cross section results start getting higher that the experimental data. [47.4-47.8 eV] is the region where the transition $^2D^e \rightarrow {}^2D^o$ occurs, and resonances, generated through this transition and with its different channels, are very narrow, but very high in magnitude (over 1000.0 Mb).

A summary of positions, widths and identifications of the major resonances obtained in the relativistic Breit-Pauli calculation is given in table 4.8, along with a comparison with available experimental data [19,92]. In general the agreement is quite good, especially for resonances in the lower energy region (below 45.50 eV) as regards both position and width. Note that some of the resonances listed in table 4.8 can be reached by more than one initial state in the experimental mixture. They are listed more

Table 4. 8: Theoretical (relativistic Breit-Pauli) and experimental [21,22] resonance energies E_{res} (eV), widths Γ (meV) and the corresponding transitions.

This Calculation		Transitions	Experiments		
E_{res}	Γ		E_{res} [22]	Γ [22]	E_{res} [21]
43.54	1280	$^2D^e_{3/2} \rightarrow 3p^5(3d^2\ ^3F)\ ^2F^o_{5/2}$	43.67	930.9	43.46
43.71	1300	$^2D^e_{5/2} \rightarrow 3p^5(3d^2\ ^3F)\ ^2F^o_{7/2}$	43.67	930.9	
43.48	1280	$^2D^e_{5/2} \rightarrow 3p^5(3d^2\ ^3F)\ ^2F^o_{5/2}$			
44.45	44.4	$^2D^e_{3/2} \rightarrow (3p^5 3d\ ^3P)4s\ \ ^2P^o_{1/2}$	44.46	39.7	44.42
44.62	40.4	$^2D^e_{5/2} \rightarrow (3p^5 3d\ ^3P)4s\ \ ^2P^o_{3/2}$	44.65	52.1	44.61
44.68	40.4	$^2D^e_{3/2} \rightarrow (3p^5 3d\ ^3P)4s\ \ ^2P^o_{3/2}$			
45.68	3.8	$^2D^e_{5/2} \rightarrow (3p^5 3d\ ^3F)4s\ \ ^2F^o_{7/2}$	46.04	4.3	
45.97	3.4	$^2D^e_{5/2} \rightarrow (3p^5 3d\ ^3F)4s\ \ ^2F^o_{5/2}$	46.33	4.7	
46.03	3.4	$^2D^e_{3/2} \rightarrow (3p^5 3d\ ^3F)4s\ \ ^2F^o_{5/2}$	46.38	4.7	
47.46	1.4	$^2D^e_{5/2} \rightarrow 3p^5(3d^2\ ^3F)\ ^2D^o_{5/2}$	47.77		47.62
47.52	1.4	$^2D^e_{3/2} \rightarrow 3p^5(3d^2\ ^3F)\ ^2D^o_{5/2}$	47.81		47.67
47.68	6.1	$^2D^e_{3/2} \rightarrow 3p^5(3d^2\ ^3P)\ ^2P^o_{1/2}$	47.58	16.1	47.54
47.61	4.3	$^2D^e_{5/2} \rightarrow 3p^5(3d^2\ ^3P)\ ^2P^o_{3/2}$	47.66	23.6	47.51
47.66	4.3	$^2D^e_{3/2} \rightarrow 3p^5(3d^2\ ^3P)\ ^2P^o_{3/2}$	47.71	9.9	47.56
47.91	26.3	$^2D^e_{5/2} \rightarrow (3p^5 3d\ ^1F)4s\ \ ^2F^o_{7/2}$	48.37	28.5	
47.91	23.7	$^2D^e_{5/2} \rightarrow (3p^5 3d\ ^1F)4s\ \ ^2F^o_{5/2}$	48.32	18.6	
48.57	15.2	$^2S^e_{1/2} \rightarrow 3p^5(4s^2\ ^1S)\ ^2P^o_{3/2}$	48.64	24.8	
48.73	26.9	$^2S^e_{1/2} \rightarrow 3p^5(4s^2\ ^1S)\ ^2P^o_{1/2}$	48.69	24.8	
49.04	192.7	$^2S^e_{1/2} \rightarrow (3p^5 3d\ \ ^1P)4s\ \ ^2P^o_{3/2}$			
49.12	175.2	$^2S^e_{1/2} \rightarrow (3p^5 3d\ \ ^1P)4s\ \ ^2P^o_{1/2}$			

than once for purposes of comparison with the experimental results. They are listed at different photon energy simply because each of the initial states has a different ionization energy so that different photon energies are required from each of these initial states to excite a particular resonance, i.e., the difference in the resonance energies for a given resonance state in the table is just the difference in the binding energies of the initial states of the transitions.

Additional results to complete the Ti^{+3} resonance analysis are the list of line strengths and oscillator strengths for five of the major resonances chosen from table 4.8, and this is shown in table 4.9. As expected and can be seen in table 4.9, transitions with $\Delta j = 1$ ($^2D^e_{3/2} \rightarrow 3p^5(3d^2\ ^3F)\ ^2F^o_{5/2}$, $^2D^e_{5/2} \rightarrow 3p^5(3d^2\ ^3F)\ ^2F^o_{7/2}$ and $^2S^e_{1/2} \rightarrow (3p^5 3d\ ^1P)4s\ ^2P^o_{3/2}$) have stronger line strength and oscillator strength than transitions with $\Delta j = 0$ ($^2D^e_{5/2} \rightarrow 3p^5(3d^2\ ^3F)\ ^2F^o_{5/2}$ and $^2S^e_{1/2} \rightarrow (3p^5 3d\ ^1P)4s\ ^2P^o_{1/2}$).

Table 4.9: Ti IV (Ti^{+3}) line strength (S) and oscillator strength (f) for five of the major resonances.

Transitions	Δj	S (a.u.)	f
$^2D^e_{3/2} \rightarrow 3p^5(3d^2\ ^3F)\ ^2F^o_{5/2}$	1	5.206	0.926
$^2D^e_{5/2} \rightarrow 3p^5(3d^2\ ^3F)\ ^2F^o_{7/2}$	1	7.728	1.035
$^2S^e_{1/2} \rightarrow (3p^5 3d\ ^1P)\ 4s\ ^2P^o_{3/2}$	1	4.885	1.468
$^2D^e_{5/2} \rightarrow 3p^5(3d^2\ ^3F)\ ^2F^o_{5/2}$	0	0.270	0.048
$^2S^e_{1/2} \rightarrow (3p^5 3d\ ^1P)\ 4s\ ^2P^o_{1/2}$	0	1.166	0.702

4.2.2. Photoionization of V^{+4}, Cr^{+5}, Mn^{+6} and Fe^{+7} Ions

4.2.2.1. Photoionization of V^{+4} from Threshold to 116.0 eV

Stating with V^{+4}, and continuing with other ions in the K-like transition metal ions series studied here (Cr^{+5}, Mn^{+6} and Fe^{+7}), the Super-Coster-Kronig decay channel, that produces those giant ($3p \rightarrow 3d$) dipole resonances is closed because the $3p \rightarrow 3d$ excitation energy is below the ionization threshold; therefore resonance structures observed in the photoionization cross section spectra of those ions are much narrower than what we have seen in Sc^{+2} and Ti^{+3} (see above sections).

In figure 4.10, we present the asymmetry parameter and photoionization cross section calculation results for the ground $^2D^e$ initial state of V^{+4}. The asymmetry parameter β dependence on energy is shown in figure 4.10(a); this is a non-relativistic operations (LS coupling), therefore photoionization of the $^2D^e$ initial state involves 2 transitions ($d \rightarrow p$ and $d \rightarrow f$) leading to final states[$(3s^2 3p^6\ ^1S^e)\ \varepsilon p\ ^2P^o$] and [$(3s^2 3p^6\ ^1S^e)\ \varepsilon f\ ^2F^o$]; since we have at least two channels (for the final state), β is energy dependent [figure 4.10(a)]. Figure 4.10(b) photoionization cross section results for the ground $^2D^e$ state leaving the residual (target) V^{+5} ion in the ground state $3s^2 3p^6\ ^1S^o$. We can see in figure 4.10(b) that the cross section is dominated by series of Rydberg resonances associated with the $3p$ electron excitation to higher principal quantum number, with respect to the Sc^{+2} and Ti^{+3} cases; they can be described as [$(3p^5 nd)$ 3d $^2P^o$, $^2F^o$] and [$(3p^5 n's)$ $3d\ ^2P^o$, $^2F^o$] (with $n \geq 4$ and $n' \geq 5$). Those series eventually decay to continua [$3s^2 3p^6\ ^1S^e$ (εf, εp)], which also originate from direct photoionization of the ground [Ne]$3s^2 3p^6 3d\ ^2D^e$ state of V^{+4}. We must note that those sequences of Rydberg resonances start converging at photon energy 103.78 eV (103.43 eV from experiment [89] to excited target V^{+5}state

$3s^2 3p^5 3d\ ^3\mathrm{P}^o$, and the upper limit of both series is the excited target V^{+5} ($3p^5 3d\ ^1\mathrm{P}^o$) state at photon energy 120.94 eV (120.44 eV from experiment [89]).

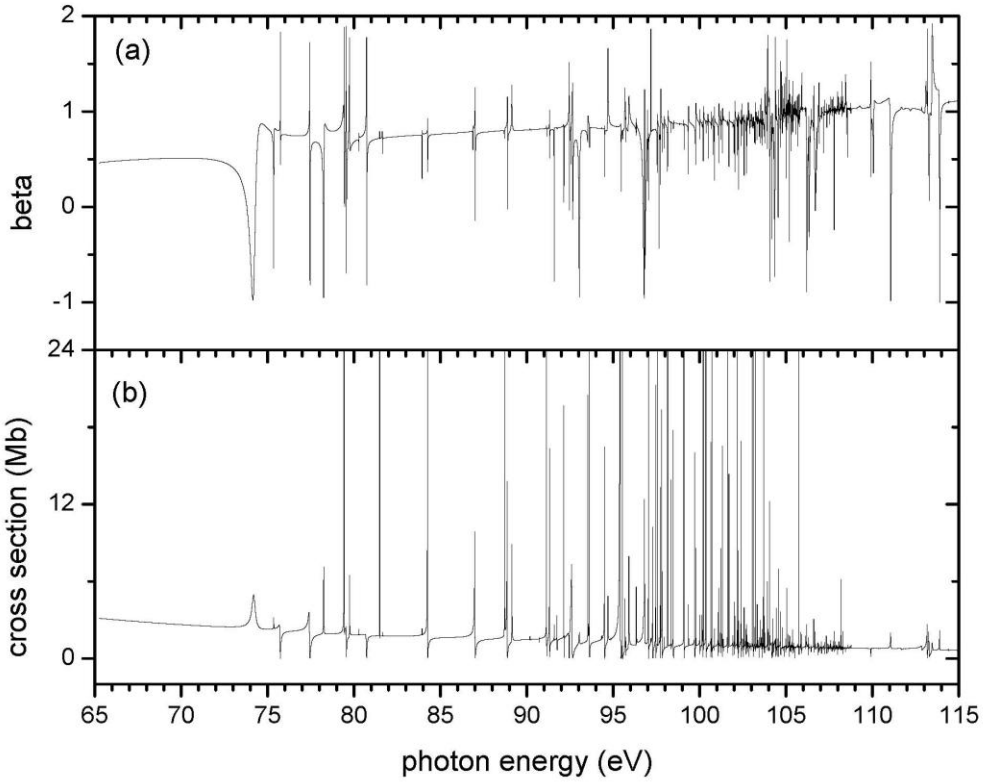

Figure 4.10: Non-relativistic calculations for V^{+4} showing (a) initial $^2\mathrm{D}^e$ ground state asymmetry parameter β energy dependence for $d \rightarrow p$ and $d \rightarrow f$ transitions, and (b) the main line cross sections for photoionization of V^{+4} $^2\mathrm{D}^e$ initial state leaving the residual (target) V^{+5} ion in the ground state $3s^2 3p^6\ ^1\mathrm{S}^o$.

For relativistic photoionization cross section calculations, there are two initials states: the ground state $^2D^e_{3/2}$ and the first excited state $^2D^e_{5/2}$. The Breit-Pauli results for the photoionization of the ground $^2D^e_{3/2}$ state of V^{+4} are presented in figure 4.11. From the $^2D^e_{3/2}$ ground state, transitions to final states with j =5/2, 3/2 and 1/2 are allowed, and these cross sections are shown in figures 4.11(a), 4.11(b) and 4.11(c) respectively. In figure 4.12 we present the calculated Breit-Pauli results for photoionization cross section of excited $^2D^e_{5/2}$ state. The partial cross section results for j = 7/2, 5/2 and 3/2 final states are shown in figures 4.12(a), 4.12(b) and 4.12(c) respectively. Figure 4.13 shows non-relativistic and relativistic results for V^{+4} photoionization calculations; in figure 4.13(a) non-relativistic cross sections for the V^{+4} $^2D^e$ are presented, and as in the case of Sc^{+2} or Ti^{+3}, discussed above, figures 4.13(a) and 4.10(b) exactly look the same up to photon energy 103.01 eV because photoionization of V^{+4} leaving the target ion V^{+5} in the ground state $3s^2 3p^6$ $^1S^e$ is the only open channel until this energy level is reached. Figure 4.13(b) is about the total cross sections from the ground $^2D^e_{3/2}$ state, and figure 4.13(c) shows the total cross sections from the excited $^2D^e_{5/2}$ state of V^{+4}. For both $^2D^e_{3/2}$ and $^2D^e_{5/2}$ states of V^{+4} cross section shown in figures 4.13(b) and 4.13(c), the series of Rydberg resonances associated with the 3p electron photoexcitation are [($3p^5nd$) 3d $^2P^o$, $^2D^o$, $^2F^o$] and [($3p^5n's$) 3d $^2P^o$, $^2D^o$, $^2F^o$] (with $n \geq 4$ and $n' \geq 5$); note the difference between figures 4.13(b) and 4.13(c) on the one hand, and figures 4.13(a) on the other hand, is due to transition $^2D^e \rightarrow {}^2D^o$ which is forbidden in the non-relativistic approach until photon energy 103.78 eV (103.43 eV in the experiment []89]). The fact that the

difference is noticeable demonstrates the importance of relativistic interactions even at this (relatively) low Z.

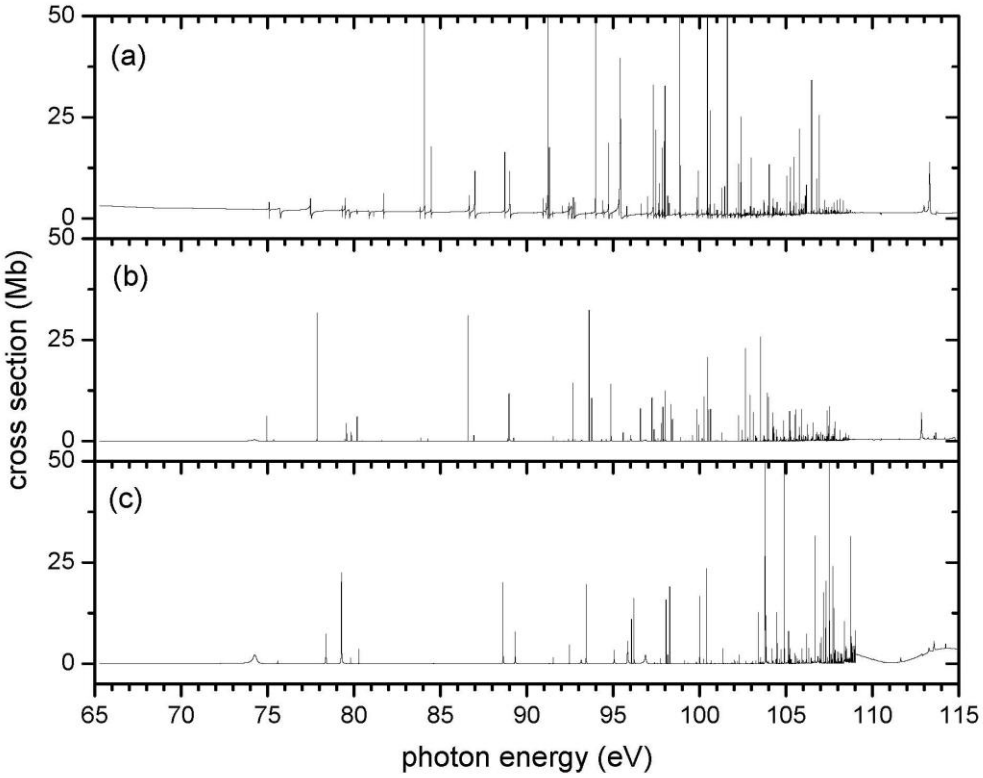

Figure 4.11: Calculated Breit-Pauli photoionization cross sections for the ground $^2D^e_{3/2}$ state of V^{+4} showing, (a) the partial cross section to the j=5/2 final state, (b) the partial cross section to the j=3/2 final state, (c) the partial cross section to the j=1/2 final state.

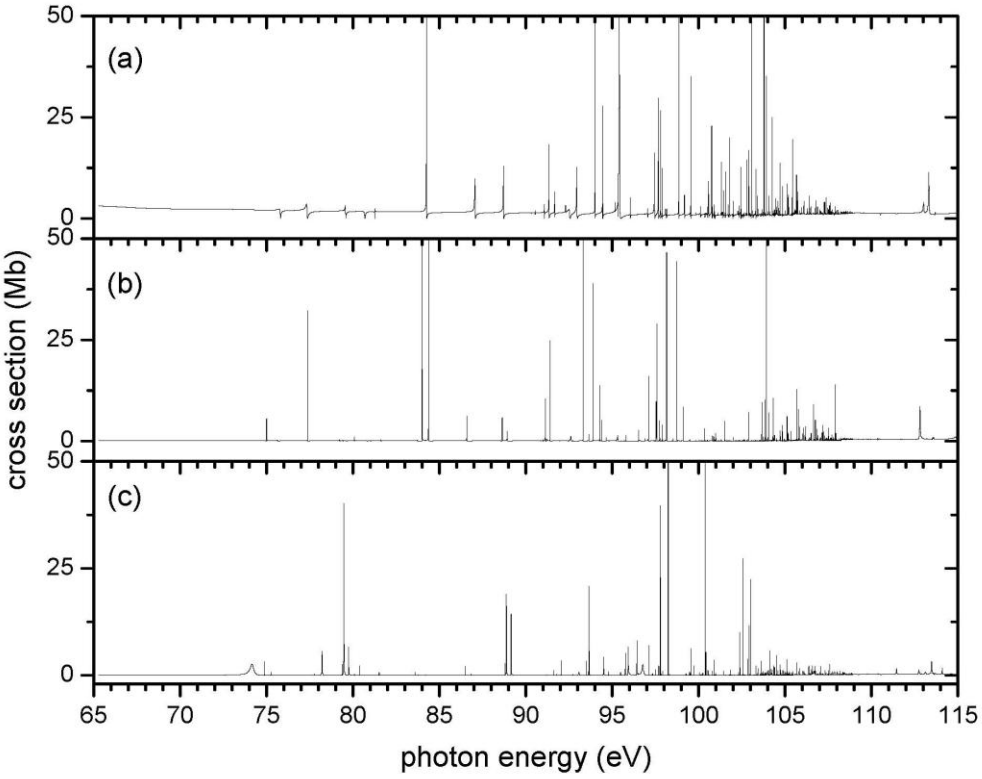

Figure 4.12: Calculated Breit-Pauli photoionization cross sections for the excited $^2D^e_{5/2}$ state of V^{+4} showing, (a) the partial cross section to the j=7/2 final state, (b) the partial cross section to the j=5/2 final state and (c) the partial cross section to the j=3/2 final state.

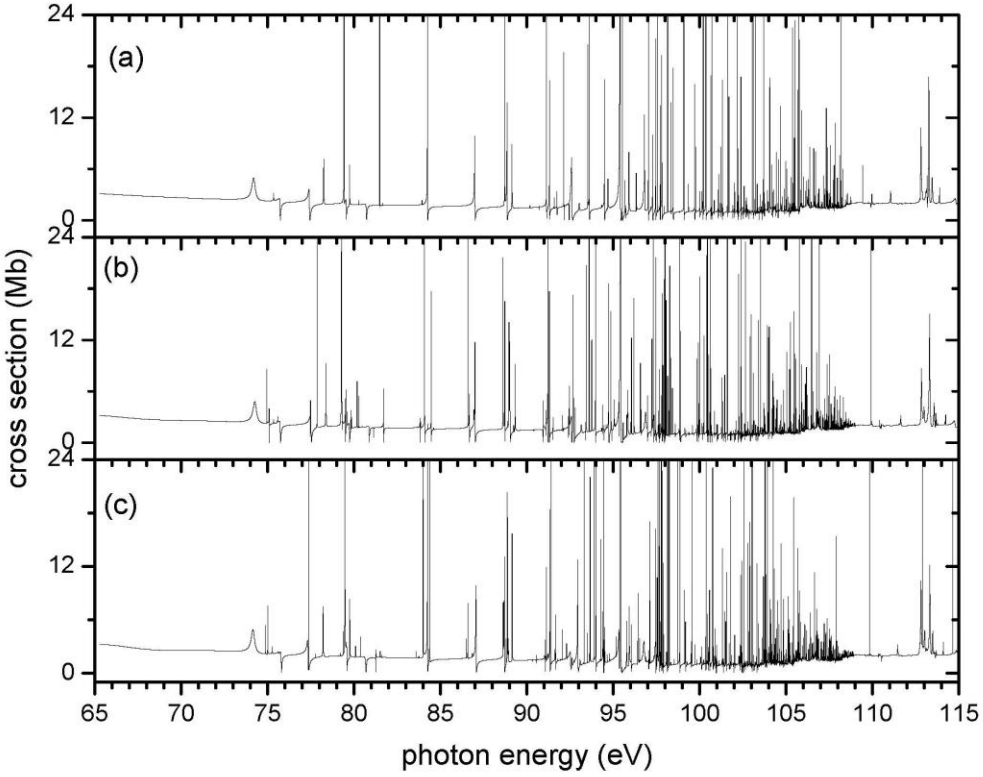

Figure 4.13: Calculated V^{+4} photoionization cross sections showing (a) non-relativistic (LS-coupling) cross sections from the initial ground state $^2D^e$, (b) the total for the ground $^2D^e_{3/2}$ state, and (c) the total for the excited $^2D^e_{5/2}$ state.

4.2.2.2. Photoionization of Cr^{+5} from Threshold to 145.0 eV

In figure 4.14, we present the asymmetry parameter and photoionization cross section calculation results for the ground $^2D^e$ initial state of Cr^{+5}. The asymmetry parameter β dependence on energy is shown in figure 4.14(a); this is a non-relativistic operations (LS coupling), therefore photoionization of the $^2D^e$ initial state involves 2 transitions ($d \rightarrow p$ and $d \rightarrow f$) leading to final states [($3s^2 3p^6\ ^1S^e$) $\varepsilon p\ ^2P^o$] and [($3s^2 3p^6\ ^1S^e$) $\varepsilon f\ ^2F^o$]; since we have at least two channels (for the final state), β is energy dependent [figure 4.14(a)]. Figure 4.14(b) shows photoionization cross section results for the ground $^2D^e$ state leaving the residual (target) Cr^{+6} ion in the ground state $3s^2 3p^6\ ^1S^o$. We can see in figure 4.14(b) that the cross section is dominated by series of Rydberg resonances associated with the $3p$ electron excitation to higher principal quantum number, with respect to the Sc^{+2} and Ti^{+3} cases; they can be described as [($3p^5 nd$) $3d\ ^2P^o$, $^2F^o$] and [($3p^5 n's$) $3d\ ^2P^o$, $^2F^o$] (with $n \geq 4$ and $n' \geq 5$). Those series eventually decay to continua [$3s^2 3p^6\ ^1S^e$ (εf, εp)], which also originate from direct photoionization of the ground [Ne]$3s^2 3p^6 3d\ ^2D^e$ state of Cr^{+5}. We must note that those sequences of Rydberg resonances start converging at photon energy 133.54 eV (133.46 eV from experiment [89] to excited target Cr^{+6}state $3s^2 3p^5 3d\ ^3P^o$, and the upper limit of both series is the excited target Cr^{+6} ($3p^5 3d\ ^1P^o$) state at photon energy 152.39 eV (151.67 eV from experiment [89]).

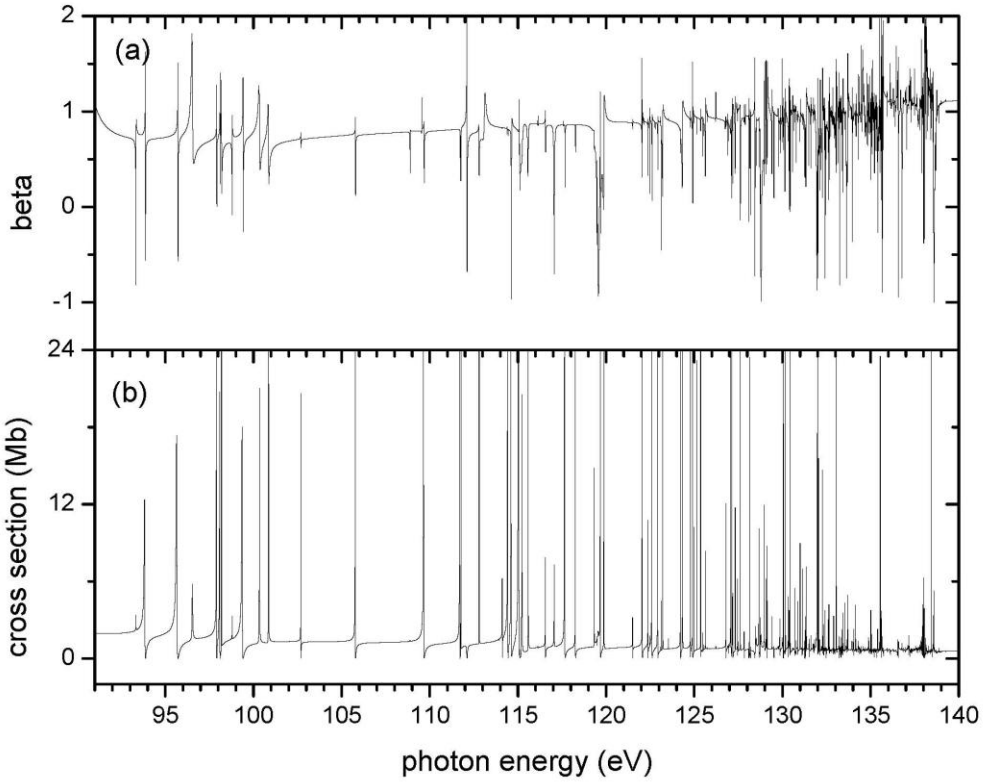

Figure 4.14: Non-relativistic calculations for Cr^{+5} showing (a) initial $^2D^e$ ground state asymmetry parameter β energy dependence for $d \rightarrow p$ and $d \rightarrow f$ transitions, and (b) the main line cross sections for photoionization of Cr^{+5} $^2D^e$ initial state leaving the residual (target) Cr^{+6} ion in the ground state $3s^2 3p^6\ ^1S^o$.

For Cr^{+5} relativistic photoionization cross section calculations, we have two initials states: the ground $^2D^e_{3/2}$ state and the first excited $^2D^e_{5/2}$ state. The Breit-Pauli results for the photoionization of the ground $^2D^e_{3/2}$ state of Cr^{+5} are presented in figure 4.15. From the $^2D^e_{3/2}$ ground state, transitions to final states with j =5/2, 3/2 and 1/2 are

allowed, and these cross sections are shown in figures 4.15(a), 4.15(b) and 4.15(c) respectively. In figure 4.16 we present the calculated Breit-Pauli results for photoionization cross section of excited $^2D^e_{5/2}$ state. The partial cross section results for j = 7/2, 5/2 and 3/2 final states are shown in figures 4.16(a), 4.16(b) and 4.16(c) respectively. Figure 4.17 shows non-relativistic and relativistic results for Cr^{+5} photoionization calculations; in figure 4.17(a) cross sections for the Cr^{+5} $^2D^e$ are presented, and as in the case of Sc^{+2} or Ti^{+3}, discussed above, figures 4.17(a) and 4.14(b) exactly look the same up to photon energy 133.54 eV because photoionization of Cr^{+5} leaving the target ion Cr^{+6} in the ground state $3s^2 3p^6$ $^1S^e$ is the only open channel until this energy level is reached. Figure 4.17(b) is about the total cross sections from the ground $^2D^e_{3/2}$ state, and figure 4.17(c) shows the total cross sections from the excited $^2D^e_{5/2}$ state of Cr^{+5}. For both $^2D^e_{3/2}$ and $^2D^e_{5/2}$ states of Cr^{+5} cross section shown in figures 4.17(b) and 4.17(c), the series of Rydberg resonances associated with the 3p electron photoexcitation are [($3p^5nd$) 3d $^2P^o$, $^2D^o$, $^2F^o$] and [($3p^5n's$) 3d $^2P^o$, $^2D^o$, $^2F^o$] (with $n \geq 4$ and $n' \geq 5$); note the difference between figures 4.17(b) and 4.17(c) on the one hand, and figures 4.17(a) on the other, is due to transition $^2D^e \rightarrow {}^2D^o$ which is forbidden in the non-relativistic approach until photon energy 133.54 eV (133.47 eV in the experiment []89]). The fact that the difference is noticeable demonstrates the importance of relativistic interactions even at this (relatively) low Z.

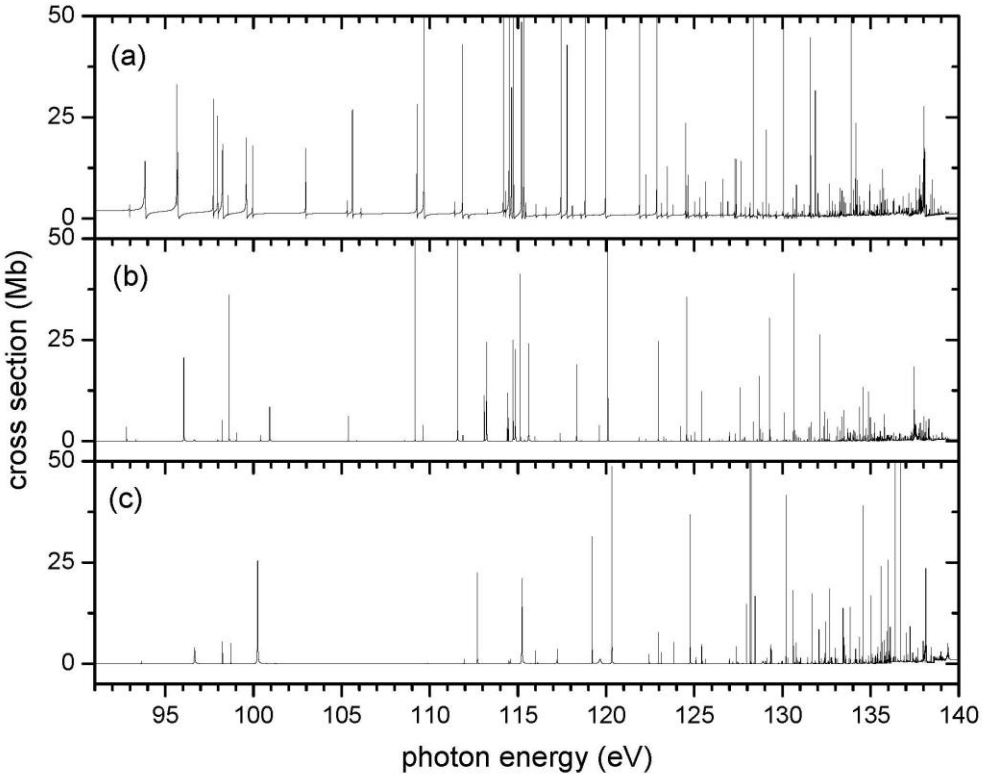

Figure 4.15: Calculated Breit-Pauli photoionization cross sections for the ground $^2D^e_{3/2}$ state of Cr^{+5} showing, (a) the partial cross section to the j=5/2 final state, (b) the partial cross section to the j=3/2 final state, (c) the partial cross section to the j=1/2 final state.

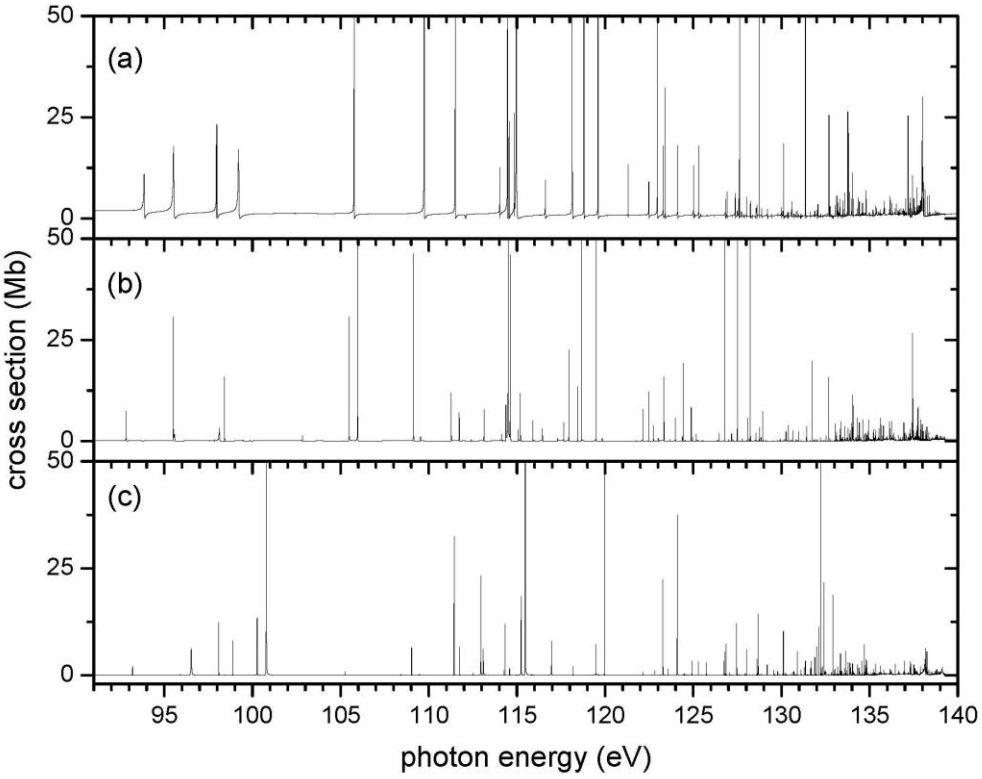

Figure 4.16: Calculated Breit-Pauli photoionization cross sections for the excited $^2D^e_{5/2}$ state of Cr^{+5} showing, (a) the partial cross section to the j=7/2 final state, (b) the partial cross section to the j=5/2 final state and (c) the partial cross section to the j=3/2 final state.

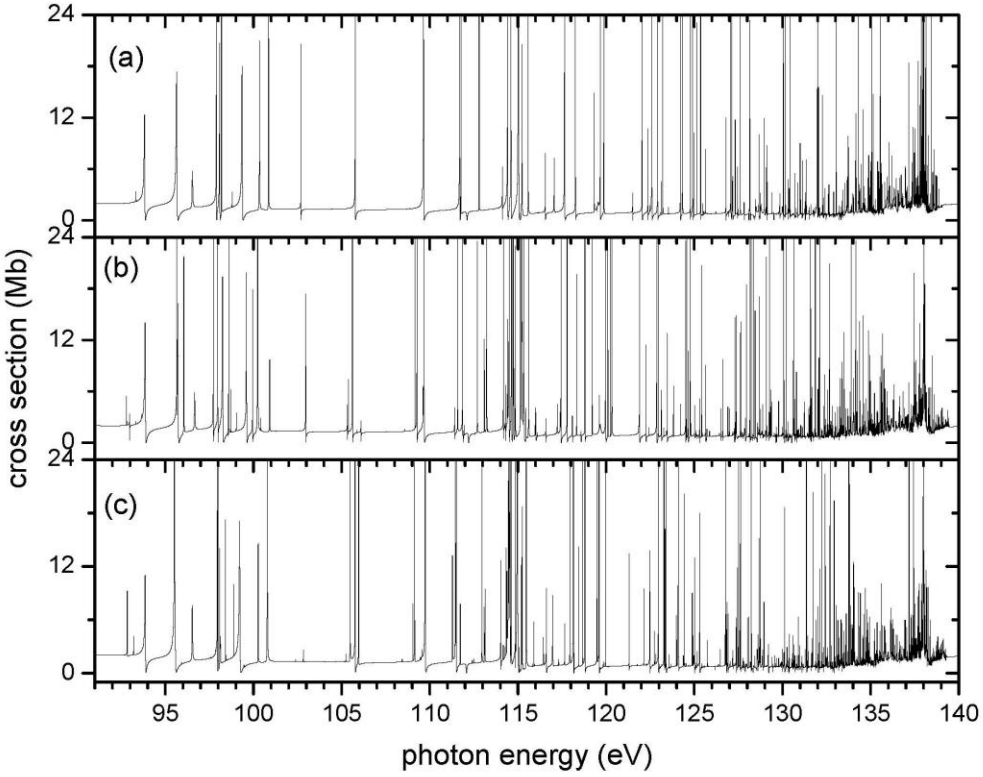

Figure 4.17: Calculated Cr^{+5} photoionization cross sections showing (a) non-relativistic (LS-coupling) cross sections from the initial ground state $^2D^e$, (b) the total for the ground $^2D^e_{3/2}$ state, and (c) the total for the excited $^2D^e_{5/2}$ state.

4.2.2.3. Photoionization of Mn^{+6} from Threshold to 170.0 eV

In figure 4.18, we present the asymmetry parameter and photoionization cross section calculation results for the ground $^2D^e$ initial state of Mn^{+6}. The asymmetry parameter β dependence on energy is shown in figure 4.18(a); this is a non-relativistic operations (LS coupling), therefore photoionization of the $^2D^e$ initial state involves 2 transitions ($d \rightarrow p$ and $d \rightarrow f$) leading to final states [($3s^2 3p^6\ ^1S^e$) $\varepsilon p\ ^2P^o$] and [($3s^2 3p^6\ ^1S^e$) $\varepsilon f\ ^2F^o$]; since we have at least two channels (for the final state), β is energy dependent [figure 4.18(a)]. Figure 4.18(b) shows photoionization cross section results on the ground $^2D^e$ state leaving the residual (target) Mn^{+7} ion in the ground state $3s^2 3p^6\ ^1S^o$. We can see in figure 4.18(b) that the cross section is dominated by series of Rydberg resonances associated with the $3p$ electron excitation to higher principal quantum number, with respect to the Sc^{+2} and Ti^{+3} cases; they can be described as [($3p^5 nd$) $3d\ ^2P^o$, $^2F^o$] and [($3p^5 n's$) $3d\ ^2P^o$, $^2F^o$] (with $n \geq 4$ and $n' \geq 5$). Those series eventually decay to continua [$3s^2 3p^6\ ^1S^e$ (εf, εp)], which also originate from direct photoionization of the ground [Ne]$3s^2 3p^6 3d\ ^2D^e$ state of Mn^{+6}. We must note that those sequences of Rydberg resonances start converging at photon energy 166.00 eV (165.68 eV from experiment [89] to excited target Mn^{+7}state $3s^2 3p^5 3d\ ^3P^o$, and the upper limit of both series is the excited target Mn^{+7} ($3p^5 3d\ ^1P^o$) state at photon energy 186.87 eV (185.94 eV from experiment [89]).

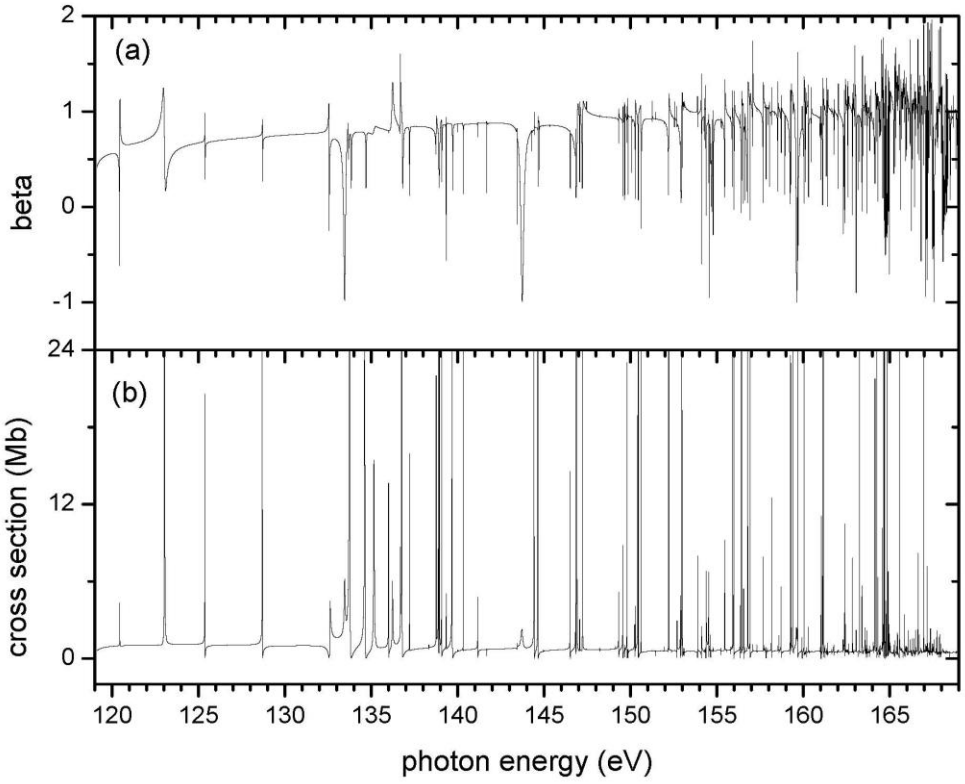

Figure 4.18: Non-relativistic calculations for Mn^{+6} showing (a) initial $^2D^e$ ground state asymmetry parameter β energy dependence for $d \rightarrow p$ and $d \rightarrow f$ transitions, and (b) the main line cross sections for photoionization of Mn^{+6} $^2D^e$ initial state leaving the residual (target) Mn^{+7} ion in the ground state $3s^2 3p^6\ ^1S^o$.

For Mn^{+6} relativistic photoionization cross section calculations, we have two initials states: the ground $^2D^e_{3/2}$ state and the first excited $^2D^e_{5/2}$ state. The Breit-Pauli results for the photoionization of the ground $^2D^e_{3/2}$ state of Mn^{+6} are presented in figure 4.19. From the $^2D^e_{3/2}$ ground state, transitions to final states with j =5/2, 3/2 and 1/2 are

allowed, and these cross sections are shown in figures 4.19(a), 4.19(b) and 4.19(c) respectively. In figure 4.20 we present the calculated Breit-Pauli results for photoionization cross section of excited $^2D^e_{5/2}$ state. The partial cross section results for j = 7/2, 5/2 and 3/2 final states are shown in figures 4.20(a), 4.20(b) and 4.20(c) respectively. Figure 4.21 shows non-relativistic and relativistic results for Mn^{+6} photoionization calculations; in figure 4.21(a) cross sections for the Mn^{+6} $^2D^e$ are presented, and as in the case of Sc^{+2} or Ti^{+3}, discussed above, figures 4.21(a) and 4.18(b) exactly look the same up to photon energy 166.0 eV because photoionization of Mn^{+6} leaving the target ion Mn^{+7} in the ground state $3s^2 3p^6\ ^1S^e$ is the only open channel until this energy level is reached. Figure 4.21(b) is about the total cross sections from the ground $^2D^e_{3/2}$ state, and figure 4.21(c) shows the total cross sections from the excited $^2D^e_{5/2}$ state of Mn^{+6}. For both $^2D^e_{3/2}$ and $^2D^e_{5/2}$ states of Mn^{+6} cross section shown in figures 4.21(b) and 4.21(c), the series of Rydberg resonances associated with the $3p$ electron photoexcitation are [($3p^5nd$) 3d $^2P^o$, $^2D^o$, $^2F^o$] and [($3p^5n's$) $3d$ $^2P^o$, $^2D^o$, $^2F^o$] (with $n \geq 4$ and $n' \geq 5$); note the difference between figures 4.21(b) and 4.21(c) on the one hand, and figures 4.21(a) on the other, is due to transition $^2D^e \rightarrow {}^2D^o$ which is forbidden in the non-relativistic approach until photon energy 166.00 eV (165.68 eV in the experiment []89]). The fact that the difference is noticeable demonstrates the importance of relativistic interactions even at this (relatively) low Z.

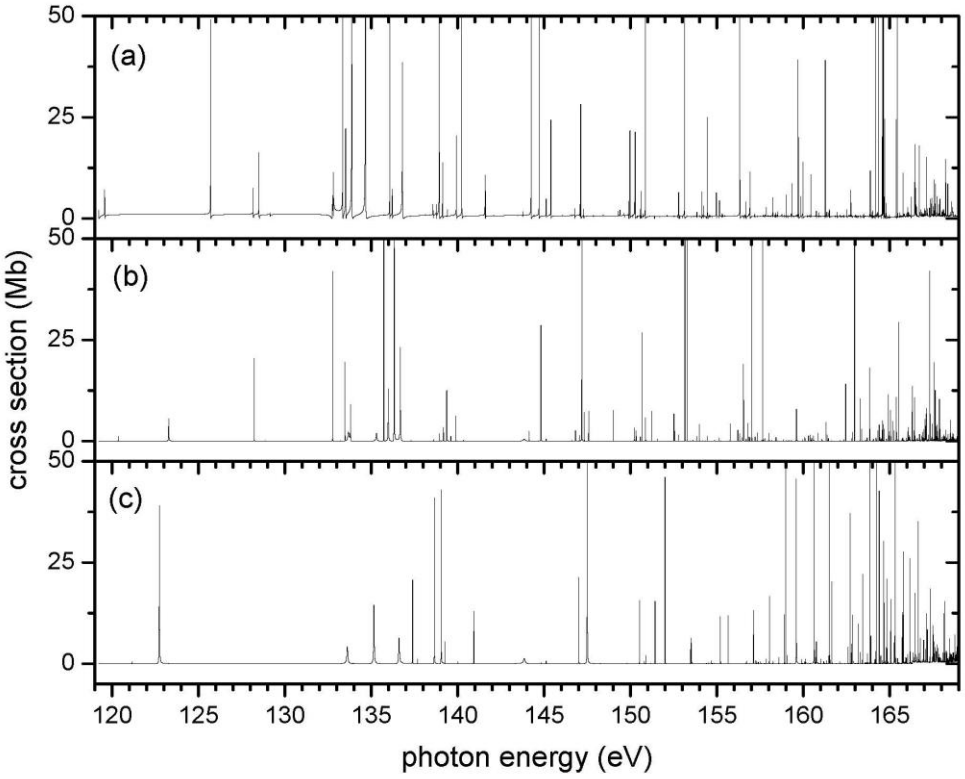

Figure 4.19: Calculated Breit-Pauli photoionization cross sections for the ground $^2D^e_{3/2}$ state of Mn^{+6} showing, (a) the partial cross section to the j=5/2 final state, (b) the partial cross section to the j=3/2 final state, (c) the partial cross section to the j=1/2 final state.

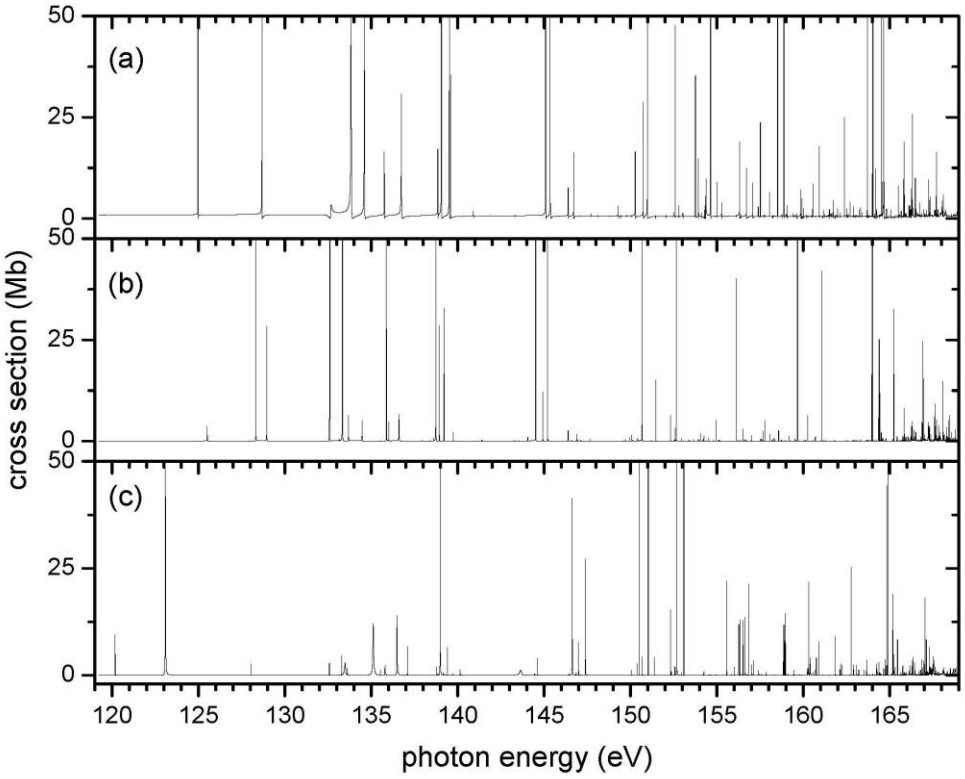

Figure 4.20: Calculated Breit-Pauli photoionization cross sections for the excited $^2D^e_{5/2}$ state of Mn^{+6} showing, (a) the partial cross section to the j=7/2 final state, (b) the partial cross section to the j=5/2 final state and (c) the partial cross section to the j=3/2 final state.

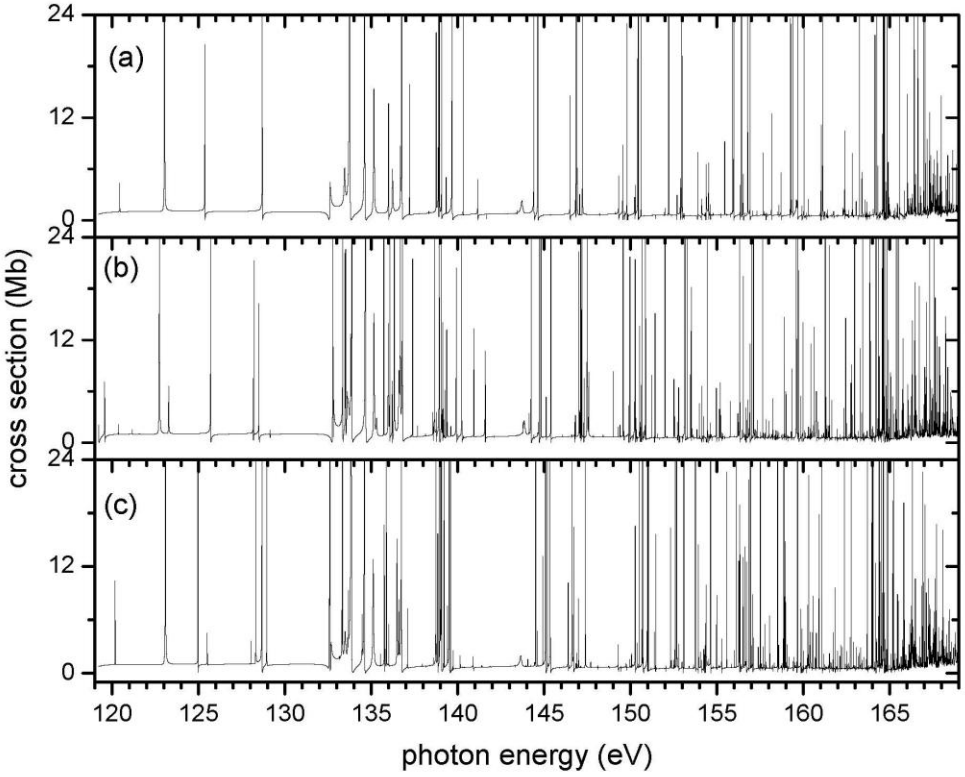

Figure 4.21: Calculated Mn^{+6} photoionization cross sections showing (a) non-relativistic (LS-coupling) cross sections from the initial ground state $^2D^e$, (b) the total for the ground $^2D^e_{3/2}$ state, and (c) the total for the excited $^2D^e_{5/2}$ state.

4.2.2.4. Photoionization of Fe^{+7} from Threshold to 203.0 eV

In figure 4.22, we present the asymmetry parameter and photoionization cross section calculation results on the ground $^2D^e$ initial state of Fe^{+7}. The asymmetry parameter β dependence on energy is shown in figure 4.22(a); this is a non-relativistic operations (LS coupling), therefore photoionization of the $^2D^e$ initial state involves 2 transitions ($d \rightarrow p$ and $d \rightarrow f$) leading to final states [($3s^2 3p^6\ ^1S^e$) $\varepsilon p\ ^2P^o$] and [($3s^2 3p^6\ ^1S^e$) $\varepsilon f\ ^2F^o$]; since we have at least two channels (for the final state), β is energy dependent [figure 4.22(a)]. Figure 4.22(b) shows photoionization cross section results on the ground $^2D^e$ state leaving the residual (target) Fe^{+8} ion in the ground state $3s^2 3p^6\ ^1S^o$. We can see in figure 4.22(b) that the cross section is dominated by series of Rydberg resonances associated with the $3p$ electron excitation to higher principal quantum number, with respect to the Sc^{+2} and Ti^{+3} cases; they can be described as [($3p^5 nd$) 3d $^2P^o$, $^2F^o$] and [($3p^5 n's$) $3d\ ^2P^o$, $^2F^o$] (with $n \geq 4$ and $n' \geq 5$). Those series eventually decay to continua [$3s^2 3p^6\ ^1S^e$ (εf, εp)], which also originate from direct photoionization of the ground [Ne]$3s^2 3p^6$3d $^2D^e$ state of Fe^{+7}. We must note that those sequences of Rydberg resonances start converging at photon energy 202.19 eV (202.21 eV from experiment [89] to excited target Fe^{+8}state $3s^2 3p^5 3d\ ^3P^o$, and the upper limit of both series is the excited target Fe^{+8} ($3p^5 3d\ ^1P^o$) state at photon energy 224.39 eV (223.39 eV from experiment [89]).

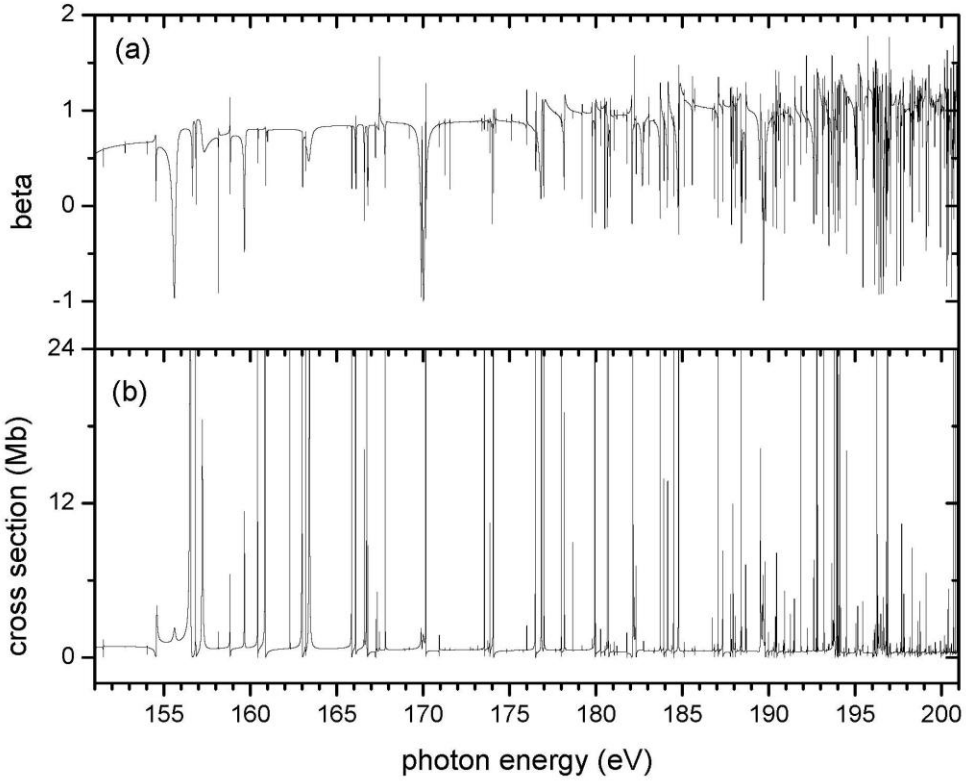

Figure 4.22: Non-relativistic calculations for Fe^{+7} showing (a) initial $^2D^e$ ground state asymmetry parameter β energy dependence for $d \rightarrow p$ and $d \rightarrow f$ transitions, and (b) the main line cross sections for photoionization of Fe^{+7} $^2D^e$ initial state leaving the residual (target) Fe^{+8} ion in the ground state $3s^2 3p^6\ ^1S^o$.

For Fe^{+7} relativistic photoionization cross section calculations, we have two initials states: the ground $^2D^e_{3/2}$ state and the first excited $^2D^e_{5/2}$ state. The Breit-Pauli results for the photoionization of the ground $^2D^e_{3/2}$ state of Fe^{+7} are presented in figure 4.23. From the $^2D^e_{3/2}$ ground state, transitions to final states with j =5/2, 3/2 and 1/2 are

allowed, and these cross sections are shown in figures 4.23(a), 4.23(b) and 4.23(c) respectively. In figure 4.24 we present the calculated Breit-Pauli results for photoionization cross section of excited $^2D^e_{5/2}$ state. The partial cross section results for j = 7/2, 5/2 and 3/2 final states are shown in figures 4.24(a), 4.24(b) and 4.24(c) respectively. Figure 4.25 shows non-relativistic and relativistic results for Fe^{+7} photoionization calculations; in figure 4.25(a) cross sections for the Fe^{+7} $^2D^e$ are presented, and as in the case of Sc^{+2} or Ti^{+3}, discussed above, figures 4.25(a) and 4.22(b) exactly look the same up to photon energy 202.2 eV because photoionization of Fe^{+7} leaving the target ion Fe^{+8} in the ground state $3s^2 3p^6$ $^1S^e$ is the only open channel until this energy level is reached. Figure 4.25(b) is about the total cross sections from the ground $^2D^e_{3/2}$ state, and figure 4.25(c) shows the total cross sections from the excited $^2D^e_{5/2}$ state of Fe^{+7}. For both $^2D^e_{3/2}$ and $^2D^e_{5/2}$ states of Fe^{+7} cross section shown in figures 4.25 (b) and 4.25(c), the series of Rydberg resonances associated with the 3p electron photoexcitation are [(3p^5nd) 3d $^2P^o$, $^2D^o$, $^2F^o$] and [(3$p^5n's$) 3d $^2P^o$, $^2D^o$, $^2F^o$] (with $n \geq 4$ and $n' \geq 5$); note the difference between figures 4.21(b) and 4.21(c) on the one hand and figures 4.21(a) on the other, is due to transition $^2D^e \rightarrow {}^2D^o$ which is forbidden in the non-relativistic approach until photon energy 202.19 eV (202.20 eV in the experiment []89]). The fact that the difference is noticeable demonstrates the importance of relativistic interactions even at this (relatively) low Z.

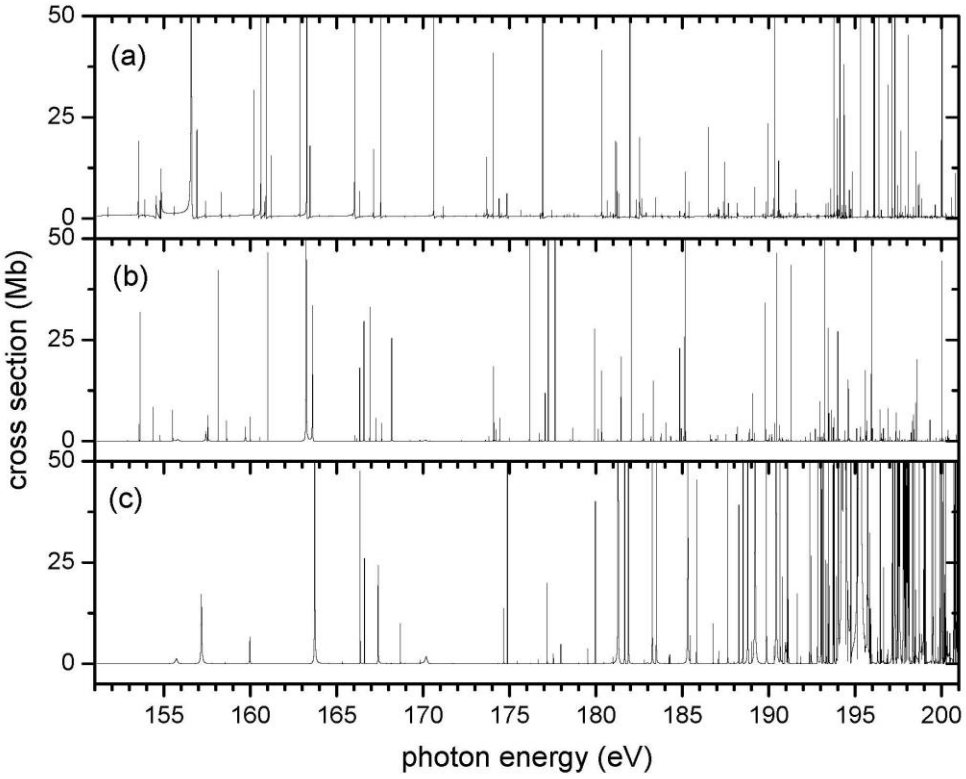

Figure 4.23: Calculated Breit-Pauli photoionization cross sections for the ground $^2D^e_{3/2}$ state of Fe^{+7} showing, (a) the partial cross section to the j=5/2 final state, (b) the partial cross section to the j=3/2 final state, (c) the partial cross section to the j=1/2 final state.

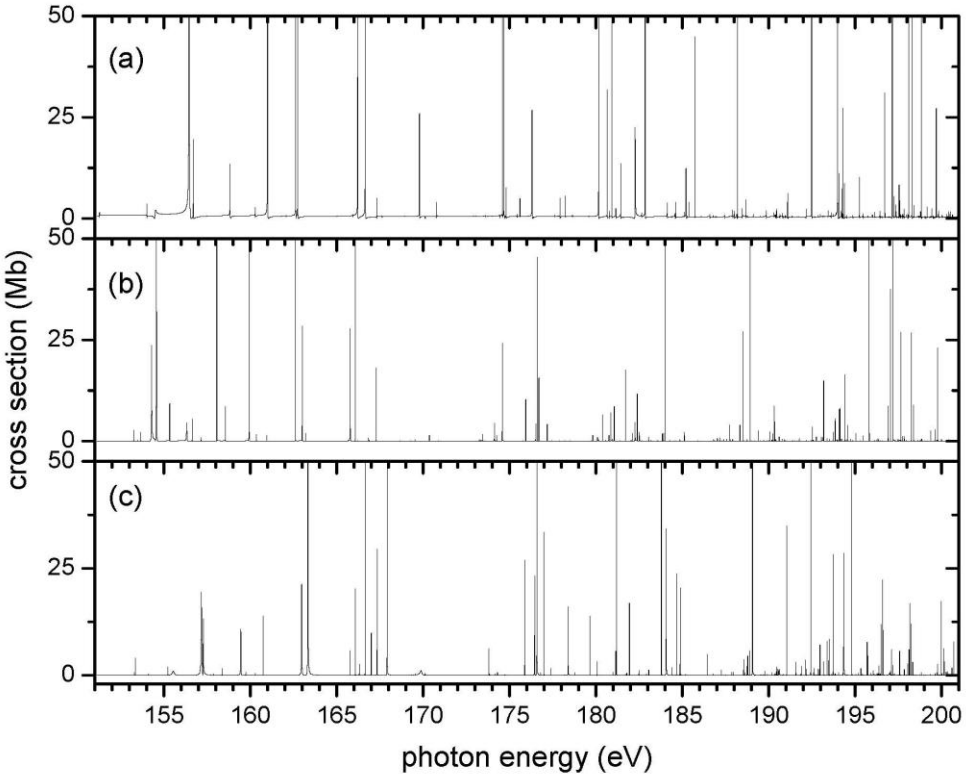

Figure 4.24: Calculated Breit-Pauli photoionization cross sections for the excited $^2D^e_{5/2}$ state of Fe^{+7} showing, (a) the partial cross section to the j=7/2 final state, (b) the partial cross section to the j=5/2 final state and (c) the partial cross section to the j=3/2 final state.

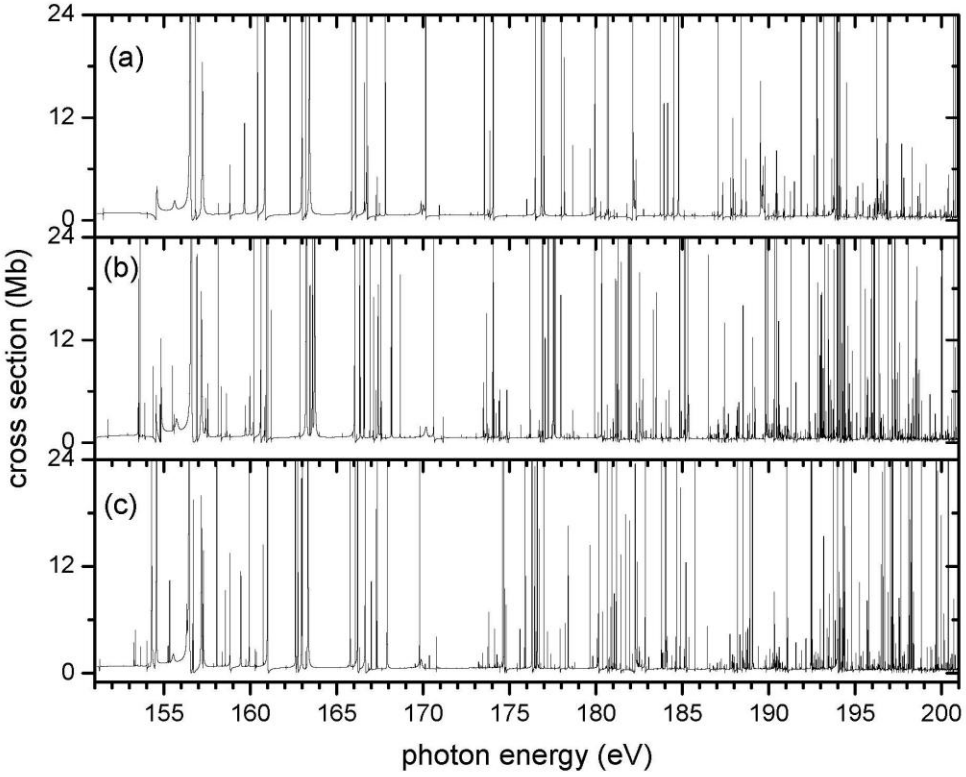

Figure 4.25: Calculated Fe^{+7} photoionization cross sections showing (a) non-relativistic (LS-coupling) cross sections from the initial ground state $^2D^e$, (b) the total for the ground $^2D^e_{3/2}$ state, and (c) the total for the excited $^2D^e_{5/2}$ state.

4.2.3. Sum of oscillator strengths comparison for K-like ions

To compare the various K-like transition metal ions, Sc^{+2}, Ti^{+3}, V^{+4}, Cr^{+5}, Mn^{+6} and Fe^{+7}, the oscillator strength (Σ_f) sum [78,103] is investigated, in each case, in each of three different states ($^2D^e$, $^2D^e_{3/2}$, $^2D^e_{5/2}$) for photon energies between the lowest ionization threshold and the first 3*p* threshold. The results of our calculations are shown in table 4.10.

Table 4.10: K-like transition metal ions (Sc^{+2}, Ti^{+3}, V^{+4}, Cr^{+5}, Mn^{+6} and Fe^{+7}) sum of oscillator strengths Σ_f for $^2D^e$, $^2D^e_{3/2}$, $^2D^e_{5/2}$ states for photon energy between 3*d* and first 3*p* electron ionization threshold..

K-like Ions	Sc^{+2}	Ti^{+3}	V^{+4}	Cr^{+5}	Mn^{+6}	Fe^{+7}
$\Sigma_f(^2D^e)$	3.99	3.19	1.08	1.00	0.99	0.79
$\Sigma_f(^2D^e_{3/2})$	5.13	3.75	1.10	1.08	1.01	0.95
$\Sigma_f(^2D^e_{5/2})$	5.44	4.26	1.12	1.09	1.03	0.94
$\Sigma_f(^2D^e_{3/2}) - \Sigma_f(^2D^e)$	1.14	0.56	0.02	0.08	0.02	0.16
$\Sigma_f(^2D^e_{5/2}) - \Sigma_f(^2D^e)$	1.45	1.07	0.04	0.09	0.04	0.15

Looking at results in table 4.10, it is evident that the oscillator strength sum in the continuum decreases with increasing Z from Z = 21 to Z = 26; this occurs because, with increasing Z, more and more of the oscillator strength of the $3p \rightarrow 3d$ transitions move into the discrete, i.e., this strength goes into bound-bound transition, not photoionization. This movement into the discrete was clearly in evidence for Ti^{+3}, discussed above, where a $3p \rightarrow 3d$ resonance straddled the threshold with about 40% of it in the discrete region. For the next ion, V^{4+} (Z=23) all of these resonant states that produce those giant ($3p \rightarrow 3d$ excitation) resonances become bound states and the oscillator strength in the continuum is seen to drop off sharply as compared to Sc^{+2} (section 3) and Ti^{+3} photoionization where almost all of the strength from the $3p^6$ subshell is owing to the giant $3p \rightarrow 3d$ resonances and lies in the continuum. For V^{+4}, Cr^{+5}, Mn^{+6} and Fe^{+7} photoionization, although the giant $3p \rightarrow 3d$ resonances occur in the discrete (below threshold), for the outer shell electron most of the oscillator strength remains

predominantly in the continuum. This is evident from table 4.10 where the oscillator strength sum for the four ions (V^{+4}, Cr^{+5}, Mn^{+6} and Fe^{+7}) is close to 1 in each case. Note that the photoionization cross sections for V^{+4}, Cr^{+5}, Mn^{+6} and Fe^{+7} are dominated by series of Rydberg resonances associated with 3*p* transitions to states with $n > 3$); since $\Delta n \neq 0$ for these transitions, the overlap (and dipole matrix element) between 3*p* orbital and *nd* orbital (n > 3) is small compared to the $\Delta n = 0$ case, so that these higher resonances are much weaker and narrower. Differences between Sc^{+2} and Ti^{+3} cases, one hand, and V^{+4}, Cr^{+5}, Mn^{+6} and Fe^{+7} on the other, in terms of continuum oscillator strength sum (table 4.10) further confirms the importance of the contribution of these giant ($3p \rightarrow 3d$ excitation) resonances to the cross section of each of the K-like ions where they lie above the ionization threshold.

Furthermore, from table 4.10, the two last lines [$\Sigma_f(\,^2D^e_{3/2})$ - $\Sigma_f(^2D^e)$ and $\Sigma_f(^2D^e_{5/2})$ - $\Sigma_f(^2D^e)$] show large differences between relativistic and non-relativistic calculations for each of the K-like ions considered here; in each case, the relativistic oscillator strengths for Sc^{+2} and Ti^{+3} are quite large, of order unity, while for V^{+4}, Cr^{+5}, Mn^{+6} and Fe^{+7} the differences are quite small. The large differences are due to the contributions of the $3p \rightarrow 3d$ dipole transition in the $^2D^e \rightarrow {}^2D^o$ channel which is forbidden in non-relativistic (LS coupling) theory below the first 3*p* ionization. This difference in continuum oscillator becomes far less important for the higher ions where all of the giant dipole oscillator strength is in the discrete. All of these observations are summarized in figure 4.26 which illustrates the evolution of the continuum oscillator strength sum with Z.

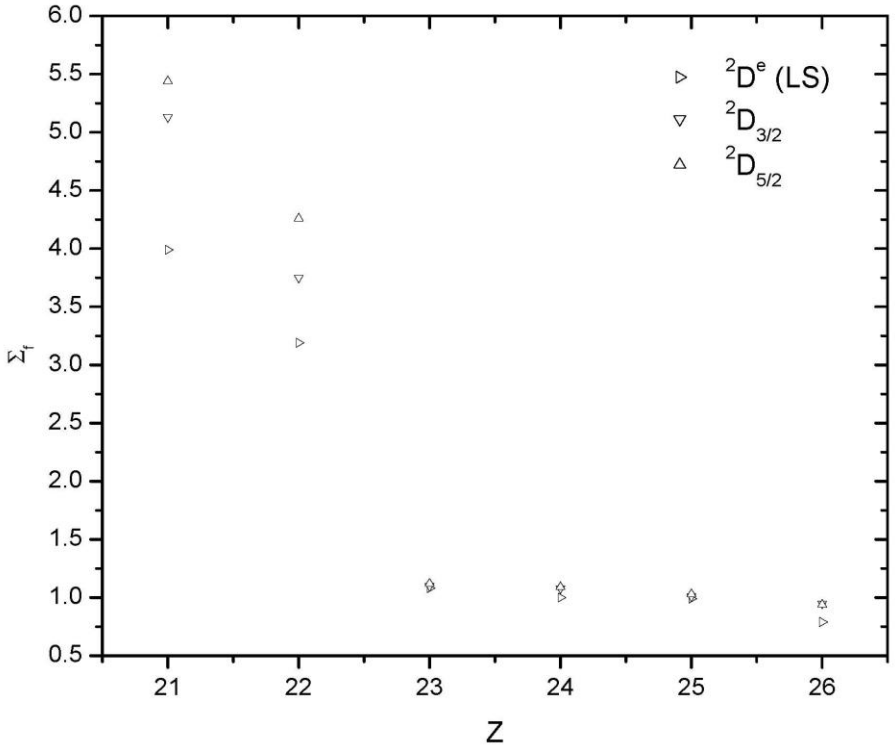

Figure 4.26: Plot of the sum of oscillator strengths Σ_f as function of nuclear charge Z for $^2D^e$ (LS-coupling), $^2D^e_{3/2}$ and $^2D^e_{5/2}$ states. Notice the weakness of Σ_f for $Z \geq 23$ compared to Σ_f for Z =21 or 22. This is due to the important contribution to Σ_f from the giant ($3p \rightarrow 3d$ excitation) dipole transition.

4.3. Conclusion

In this section, photoionization cross section calculation results for K-like transition metal ions (Ti^{+3}, V^{+4}, Cr^{+5}, Mn^{+6} and Fe^{+7}) have been presented. For each of those ions, we have performed both non-relativistic (LS-coupling) and relativistic (Breit-Pauli) calculations. While the photoionization cross section spectra of Ti^{+3}, as for Sc^{+2},

are dominated by the giant ($3p \rightarrow 3d$ excitation) resonances, those of higher Z ($Z \geq 23$) ions (V^{+4}, Cr^{+5}, Mn^{+6} and Fe^{+7}) are dominated by Rydberg series of resonances. This observation can be generalized, and extended to the last four members of the potassium isoelectronic sequence of the iron group (Co^{+8}, Ni^{+9}, Cu^{+10} and Zn^{+11}); those four ions photoionization cross section spectra also are dominated by Rydberg series of resonance. Our theoretical results on Ti^{+3} showed good quantitative and qualitative agreement with available experimental data, and highlight the necessity to include core excitations ($3p$ excitation, in this case) in the description of transition processes in open d-subshell atoms or ions. For Ti^{+3} the photoionization cross section results on the excited $[Ne]3s^2 3p^6 4s$ $^2S^e_{1/2}$ state are presented, but there is no previous work to compare with; it would be more interesting to have results from other sources (experimental or theoretical) to confirm our theoretical results. Also, for the other four ions (V^{+4}, Cr^{+5}, Mn^{+6} and Fe^{+7}), studied in this work, the same need for experimental data exists.

We have extensively talked about presence of the giant ($3p \rightarrow 3d$ excitation) resonances in the photoionization cross section spectra of potassium-like transition metal ions such as Sc^{+2} and Ti^{+3}, but it also occurs in photoionization process in potassium-like alkali earth metal ion (Ca^+); to this effect, the next section is about the study of the photoionization of ground and excited state of Ca^+ ions.

CHAPTER 5.

PHOTOIONIZATION OF GROUND AND EXCITED STATES OF Ca^+ IONS AND COMPARISON ALONG THE ISOELECTRONIC SEQUENCE

5.1. Description of the Calculations

For the calculations on Ca^+, we follow the same procedures as what was done in the calculations on Sc^{+2} (subsection 3.1.), consequently we only report on relevant differences for Ca^+ calculations. The configuration-interaction (CI) expansion of the Ca III configuration functions included four spectroscopic configurations, $3s^2 3p^6$, $3s^2 3p^5 3d$, $3s^2 3p^5 4s$ and $3s^2 3p^5 4p$, and 26 correlation configurations. Specifically, the correlation configurations included are $3s^2 3p^5 4d$, $3s^2 3p^5 4f$, $3s^2 3p^5 5s$, $3s^2 3p^5 5p$, $3s^2 3p^5 5d$, $3s 3p^6 3d$, $3s^2 3p^4 3d^2$, $3s^2 3p^4 3d 4p$, $3s^2 3p^4 4s 4p$, $3s^2 3p^4 3d 5p$, $3s^2 3p^4 4s 5p$, $3s^2 3p^4 4p 5p$, $3s^2 3p^4 4p 4d$, $3s^2 3p^4 3d 4f$, $3s^2 3p^4 4s 4f$, $3s^2 3p^4 4p 4f$, $3s^2 3p^3 3d^3$, $3s^2 3p^3 3d^2 4s$, $3s^2 3p^3 4s 4p^2$, $3s^2 3p^3 4p^3$, $3s 3p^5 3d^2$, $3s 3p^5 3d 4s$, $3s 3p^5 3d 4p$, $3s 3p^4 3d^3$, $3s 3p^6 4p$, $3s 3p^6 5d$. Thus, a total of 30 configurations corresponding to 682 LS terms were included in the nonrelativistic calculation; for the relativistic (BP) calculation, the relativistic spin-orbit, Darwin and mass correction terms were added to the Hamiltonian and the resulting CI yielded LSJ terms constructed from the LS terms.

To get some idea of the accuracy of the N-electron target state energies, the calculated and experimental (NIST) [89] energy levels relative to the ground state of Ca^{+2} states are shown in table 5.1, and reasonable agreement with experiment is seen.

Table 5.1: Calculated and experimental (NIST) [89] energy levels in Rydbergs f6r states of Ca III (Ca^{+2}) relative to the ground state.

Ca III state	J	This work	Exp. [89]
$3s^2 3p^6\ {}^1S^e$	0	0.00000	0.00000
$3s^2 3p^5 3d\ {}^3P^o$	0	1.84255	1.85327
	1	1.84753	1.85763
	2	1.85761	1.86666
$3s^2 3p^5 3d\ {}^3F^o$	4	1.94253	1.93471
	3	1.95236	1.94445
	2	1.96139	1.95315
$3s^2 3p^5 3d\ {}^1D^o$	2	2.07332	2.05788
$3s^2 3p^5 3d\ {}^3D^o$	3	2.07132	2.06250
	1	2.08113	2.07251
	2	2.08283	2.07211
$3s^2 3p^5 3d\ {}^1F^o$	3	2.09192	2.08146
$3s^2 3p^5 4s\ {}^3P^o$	2	2.19562	2.21025
	1	2.21093	2.22285
	0	2.22496	2.23818
$3s^2 3p^5 4s\ {}^1P^o$	1	2.25923	2.25717
$3s^2 3p^5 3d\ {}^1P^o$	1	2.56320	2.54565

Two separate photoionization cross section calculations were performed. In the first, relativistic effects were neglected, and the calculation was carried out with the LS-coupling non-relativistic R-matrix codes [14,15]. In the first sum in equation (13), only the terms arising from the spectroscopic configurations are included which abnegates the possibility of pseudo-resonances. In the (purely discrete) second sum, however, all of the terms from the 30 N-electron configurations, coupled to all of the single-particle orbitals, both spectroscopic and correlation, are included in the set of χ_i.

The initial state wave function, for the Ca^+ ions case, was constructed from adding a single electron to the N-electron target states to include the main configuration, $3s^2 3p^6 3d$ or $3s^2 3p^6 4s$, along with all single electron promotions out the 3*s*, 3*p* and the outer shell (3*d* or 4*s*), along with all double promotions of the type $3s^2 3p^5 nln'l'$, and the important double promotions of the $3s^2 3p^4 3d^2 nl$ variety. Other possible two-electron promotions were omitted to insure that the ground state was not overcorrelated as compared to the target states, i.e., to balance the calculation. The terms arising from these states formed the basis of a large CI calculation to obtain the initial state wave function. In table 5.2 are presented the threshold energies of the two nonrelativistic states of Ca^+, the ground $[Ne]3s^2 3p^6 4s\ ^2S^e$ state and the excited $[Ne]3s^2 3p^6 3d\ ^2D^e$ metastable state, along with the corresponding three relativistic initial states, the ground state $[Ne]3s^2 3p^6 4s\ ^2S^e_{1/2}$ plus the first two (metastable) excited states $[Ne]3s^2 3p^6 3d\ ^2D^e_{3/2}$ and $[Ne]3s^2 3p^6 3d\ ^2D^e_{5/2}$. Comparing our theoretical ionization potentials with experimental data [89], also shown in the table, it is evident that agreement between theory and experiment is rather good.

In both LS and BP calculations, the R-matrix box radius was 30.0 au, and 34 basis orbitals were used to represent the continuum for each value of the angular momentum. The QB method [16-18] is adopted in this work to determine the resonance energies and widths. The QB method works in the *R*-matrix environment (see subsection 2.6 above).

Table 5.2: Ca II (Ca^+) states threshold energy in eV compared to experiment [89].

State	Calculation	Experiment	Error (%)
$^2S^e$	11.9868	11.8717	0.96
$^2D^e$	10.1653	10.1755	0.10
$^2S^e_{1/2}$	11.9853	11.8717	0.95
$^2D^e_{3/2}$	10.1664	10.1793	0.12
$^2D^e_{5/2}$	10.1499	10.1718	0.21

5.2. Results and Discussion

5.2.1. Non-relativistic (LS coupling) Calculations

In the non-relativistic calculations for Ca^+ ions, the initial states of this ion are the ground [Ne]$3s^2 3p^6 4s\ ^2S^e$ and the excited (metastable) [Ne]$3s^2 3p^6 3d\ ^2D^e$ states. In figure 5.1, we present results of the non-relativistic calculations for photon energy from 23.0 to 46.0 eV. Figures 5.1(a) and 5.1(b) respectively illustrate the individual photoionization cross sections from ground $^2S^e$ and excited $^2D^e$ states of Ca^+; since, in both cases, the photoionization cross sections obtained using length and velocity forms agree very well, only one form (length) is displayed here and in all subsequent figures.

In the case of the Ca^+ ground $^2S^e$ state, the 4*s* electron threshold (11.98 eV from this work and 11.87 eV from experiment [89]) cross section (not seen in figure 5.1(a)) magnitude is 0.1 Mb. For photon energy below 27.0 eV [figure 5.1(a)], there are no resonances in the ground $^2S^e$ state photoionization cross section; only the direct photoionization process is possible here, and leads to $[(3s^2 3p^6\ ^1S^e)\ \varepsilon p]\ ^2P^o$. Starting at

27.0 eV, we enter the 3*p* electron excitation region characterized by the presence of series of Rydberg resonances associated with 3*p* electron photoexcitation [figures 5.1(a)] such as [($3p^5nd$) *4s* $^2P^o$] and [($3p^5n's$) *4s* $^2P^o$]. These two sequences of Rydberg resonances contain the most important features of the Ca^+ ground $^2S^e$ state photoionization cross section spectrum [figure 5.1(a)]; among them, we can point out the resonance located at 28.31 eV (2.1 meV width), and attributed to the transition $^2S^e \rightarrow 3p^5(4s^2\ ^1S)\ ^2P^o$ and the largest and broadest resonance feature in figure 5.1(a) at 33.18 eV (68.8 meV width); this peak reaches 2200 Mb, and is attributed to the transition $^2S^e \rightarrow (3p^5 3d\ ^1P)4s\ ^2P^o$ that is followed by autoionization (decay) to the ground $3s^2 3p^6\ ^1S^e$ state of Ca^{+2}. Figure 5.1(a) also displays higher order members of those Rydberg series of resonances originated from 3*p* electron photoexcitation to higher principal quantum number [($3p^5nd$) *4s* $^2P^o$] and [($3p^5n's$) *4s* $^2P^o$] with $n \geq 4$ and $n' \geq 5$, and they are mixed, and interfering with the [($3s^2 3p^6\ ^1S^e$) $\varepsilon p\ ^2P^o$] continuum. The limit of those two sequences is the excited target Ca^{+2} ($3p^5 4s\ ^1P^o$) state at energy 42.58 eV (42.47 eV from experiment [89]). Due to dipole transition selection rules, only the transition $^2S^e \rightarrow {}^2P^o$ is allowed; this confers to the outer 4*s* electron, in this photoionization of Ca^+ ground $^2S^e$ state case, a role of "spectator" since it only contributes to angular momentum coupling with its spin. The very limited number of resonances observed in this case is illustrative of this fact.

For the excited (metastable) $^2D^e$ state of Ca^+, the photoionization cross section, shown in figure 5.1(b), exhibits far more complex structure than the ground $^2S^e$ state of Ca^+. At threshold (10.16 eV in this work and 10.17 eV from experiment [89]), the cross section magnitude is 5.0 Mb (not shown in figure 5.1(b)); from threshold to 23.0 eV there are no resonances in the excited (metastable) $^2D^e$ state photoionization cross section.

Only the direct photoionization process is possible here, and leads to [$3s^2 3p^6\ {}^1S^e$ (εf, εp) ${}^2P^o$, ${}^2F^o$]. For photon energy from 23.0 to 33.0 eV, we have a mixture of direct non-resonant and indirect resonance processes, and it is evident that the resonance excitations are dominant in this region where the cross section can reach hundreds of Mb. Previous experiments and theoretical studies [97,98,109] of Ca^+ photoionization have shown that all resonant states that can contribute with significant oscillator strength, in this region, have energies above 23.0 eV; this observation qualitatively and quantitatively agrees with our results in this work. In this photon energy region [figure 5.1(b)], we observe giant, $3p \rightarrow 3d$ excitation, resonances; these $3p \rightarrow 3d$ resonances are so strong because they represent $\Delta n=0$ transitions, and, since the spatial extent of a wave function is determined largely by the principal quantum number, n, the $3p$ and $3d$ wave functions occupy substantially the same region of space, resulting in significant overlap and a rather large dipole matrix element. The photoionization cross section in this region is dominated by resonances which decay *via* autoionizing processes leading to the ground $3s^2 3p^6\ {}^1S^e$ state of Ca^{+2}. In this region, the direct photoionization contribution to the cross section can almost be neglected in terms of cross section magnitude even if by interfering with the resonant channel, the line shape of those giant resonances becomes more asymmetric depending on the relative matrix elements of the two pathways (direct and indirect processes).

The most prominent resonances in this region of figure 5.1(b) include two types of resonance corresponding to the two allowed transitions in the case of excited (metastable) ${}^2D^e$ state of Ca^+: ${}^2D^e \rightarrow {}^2F^o$ and ${}^2D^e \rightarrow {}^2P^o$ with $\Delta l = +1$ and $\Delta l = -1$ respectively. For the transition ${}^2D^e \rightarrow {}^2P^o$, we observe, in figure 5.1(b), the resonance

located at 23.41 eV (41.4 meV width) that is attributed to transition $^2D^e \rightarrow (3p^5 3d\ ^3P)4s\ ^2P^o$ and the resonance located at 30.21 eV (11.4 meV width), and is attributed to transition $^2D^e \rightarrow 3p^5(3d^2\ ^3P)\ ^2P^o$. For the transition $^2D^e \rightarrow\ ^2F^o$, the following resonances are the most important: the $^2D^e \rightarrow 3p^5(3d^2\ ^1G)\ ^2F^o$ resonance located at 24.46 eV (16.6 meV width), the $^2D^e \rightarrow 3p^5(3d^2\ ^1D)\ ^2F^o$ resonance located at 24.89 eV (119.6 meV width), the $^2D^e \rightarrow (3p^5 3d\ ^3F)4s\ ^2F^o$ resonance located at 25.72 eV (22.5 meV width), the $^2D^e \rightarrow (3p^5 3d\ ^1F)4s\ ^2F^o$ resonance located at 26.21 eV (75.5 meV width), the $^2D^e \rightarrow (3p^5 3d\ ^3P)4d\ ^2F^o$ resonance located at 30.96 eV (103.6 meV width), the $^2D^e \rightarrow (3p^5 3d\ ^3D)4d\ ^2F^o$ resonance located at 31.32 eV (2.0 meV width), the $^2D^e \rightarrow (3p^5 3d\ ^3F)4d\ ^2F^o$ resonance located at 32.02 eV (46.3 meV width) and the $^2D^e \rightarrow (3p^5 3d\ ^1D)4d\ ^2F^o$ resonance located at 32.63 eV (38.5 meV width). The largest and the strongest $^2D^e \rightarrow\ ^2F^o$ resonance is the $^2D^e \rightarrow 3p^5(3d^2\ ^3F)\ ^2F^o$ resonance located [figure 5.1(b)] at 29.29 eV (257.7 meV width). In fact all those giant resonances listed above and seen in figure 5.1(b) are the lowest and strongest members of the Rydberg series associated with the $3p$ photoexcitation, that start from photon energy 23.0 eV, and continue to the higher energy region [figure 5.1(b)] with higher principal quantum number. As examples of those series of Rydberg resonance, we have [$(3p^5 nd\ )$ 3d $^2P^o$, $^2F^o$] and [$(3p^5 n's\ ^3P^o)$ $3d\ ^2P^o$, $^2F^o$] with $n \geq 3$ and $n' \geq 4$ in figure 5.1(b).

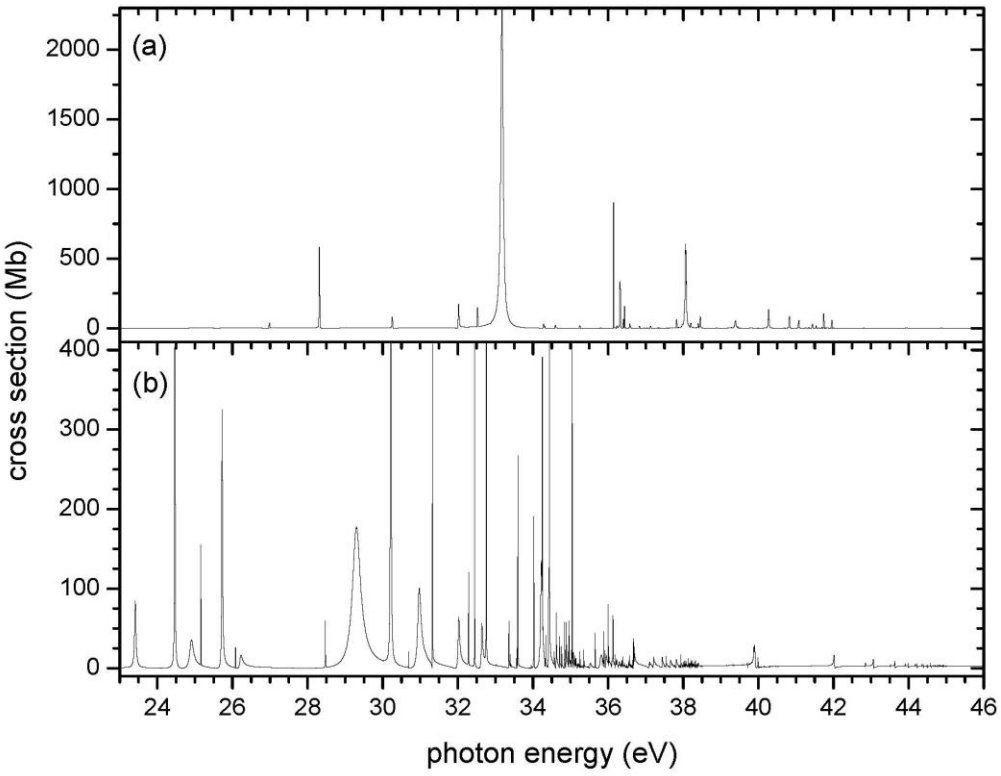

Figure 5.1: Calculated non-relativistic photoionization cross sections of Ca^{+} from 23.0 to 41.0 eV: (a) initial $^2S^e$ ground state showing the strongest resonance $^2S^e \rightarrow (3p^5 3d\ ^1P)4s\ ^2P^o$ at energy 33.18 eV and (b) initial $^2D^e$ excited (metastable) state showing the strongest resonance $^2D^e \rightarrow 3p^5(3d^2\ ^3F)\ ^2F^o$ at energy 29.20 eV. Note the complexity of $^2D^e$ excited state resonance structure compared to $^2S^e$ ground state photoionization cross sections spectrum.

Those series of Rydberg resonances interfere with direct photoionization continua $3s^2 3p^6\ ^1S^e$ (εf, εp), and converge to photon energy 35.37eV to excited Ca^{+2} state $3s^2 3p^5 3d\ ^3P^o$ for ground state photoionization, and the upper limit of both series is the

excited target Ca^{+2} ($3p^5 3d\ ^1P^o$) state at energy 44.97 eV (44.71 from experiment [89]). For excited state photoionization, in the region above 35.18 eV [figure 5.1(b)], the photon energy is high enough to produce, through resonance excitation followed by autoionization, both ground and excited states of Ca^{+2} including $3s^2 3p^6\ ^1S^e$, $3s^2 3p^5 3d\ ^3P^o$, $3s^2 3p^5 3d\ ^3F^o$, etc., i.e., ionization plus excitation; the continuum cross sections (direct process) comprise $3s^2 3p^6\ ^1S^e$ (εf, εp), $3s^2 3p^5 3d\ ^3P^o$ (εd, εs), $3s^2 3p^5 3d\ ^3F^o$ (εd, εs), and so forth.

In figure 5.2 we present cross sections from the excited (metastable) $^2D^e$ state of Ca^+ corresponding to all three allowed symmetries in the nonrelativistic regime: $^2D^e \rightarrow\ ^2F^o$, $^2D^e \rightarrow\ ^2D^o$ and $^2D^e \rightarrow\ ^2P^o$ [figures 5.2(a), 5.2(b) and 5.2(c) respectively] for photon energy from 23.0 to 46 eV. It is noteworthy that up to photon energy 35.37 eV, the Ca^+ photoionization cross section is only composed of the ejection of the 3*d* electron, leading to the ground state of the target $Ca^{+2}\ 3s^2 3p^6\ ^1S^e$; consequently only two of those three symmetries ($^2D^e \rightarrow\ ^2F^o$ and $^2D^e \rightarrow\ ^2P^o$) are possible in this range of energy. However for photon energy above 35.37 eV, all those three possibilities ($^2D^e \rightarrow\ ^2F^o$, $^2D^e \rightarrow\ ^2D^o$ and $^2D^e \rightarrow\ ^2P^o$) are allowed, as seen in figure 5.2.

The photoelectron angular distributions asymmetry parameter beta (β) dependence on energy is presented in figure 5.3 for both the excited $[Ne]3s^2 3p^6 3d\ ^2D^e$ and the ground $[Ne]3s^2 3p^6 4s\ ^2S^e$ states of Ca^+ ions. Figure 5.3(a) shows the asymmetry parameter β for the ground $[Ne]3s^2 3p^6 4s\ ^2S^e$ state, and as we see there is no energy-dependence here since $\beta = 2$. This can be understood by the fact, in non-relativistic calculations (LS coupling approach), $\beta = 2$ for $s \rightarrow p$ transition; the variation of β with

energy requires at least two outgoing channels with differing energy dependences to interfere with one another [85], and the photoionization of [Ne]$3s^2 3p^6 4s\ {}^2S^e$ state leads to

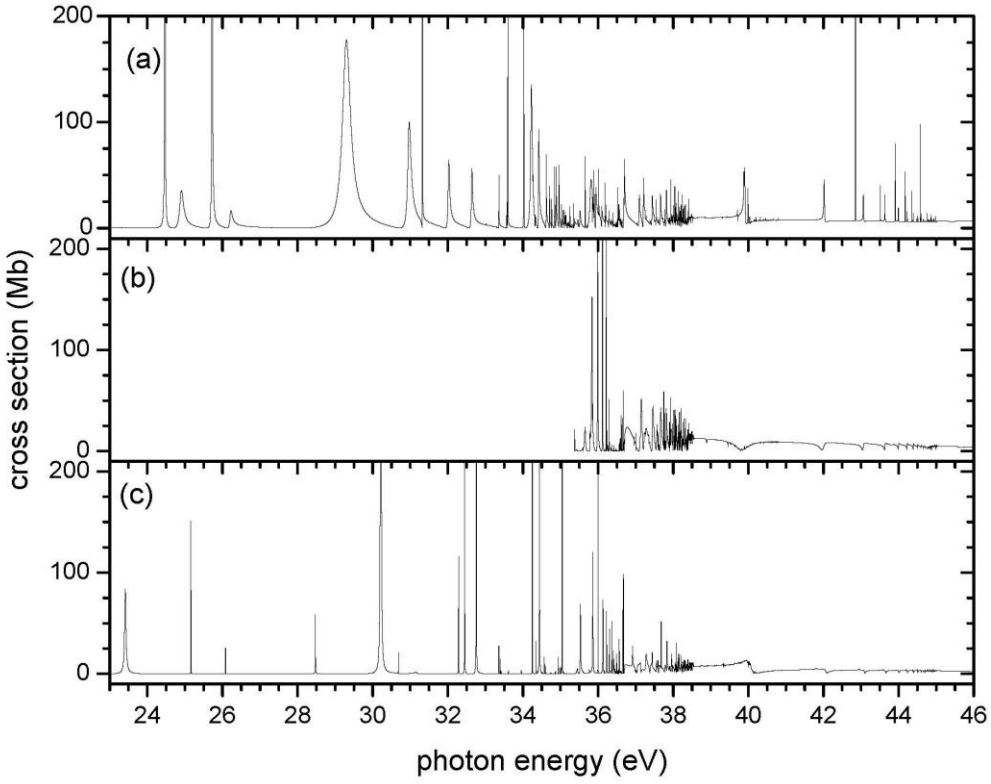

Figure 5.2: Calculated non-relativistic photoionization cross section for the Ca^+ excited (metastable) [Ne]$3s^2 3p^6 3d\ {}^2D^e$ initial state for photon energy from 23.0 to 46.0 eV showing individual cross sections corresponding to all three allow transitions from the ${}^2D^e$ initial state: (a) ${}^2D^e \rightarrow {}^2F^o$, (b) ${}^2D^e \rightarrow {}^2D^o$ and (c) ${}^2D^e \rightarrow {}^2P^o$. Note the transition ${}^2D^e \rightarrow {}^2D^o$ only occurs at photon energy above 35.37 eV, where the photon energy is high enough to produce both ground and excited states of Ca^{+2} including $3s^2 3p^6\ {}^1S^e$, $3s^2 3p^5 3d\ {}^3P^o$, $3s^2 3p^5 3d\ {}^3F^o$, etc.

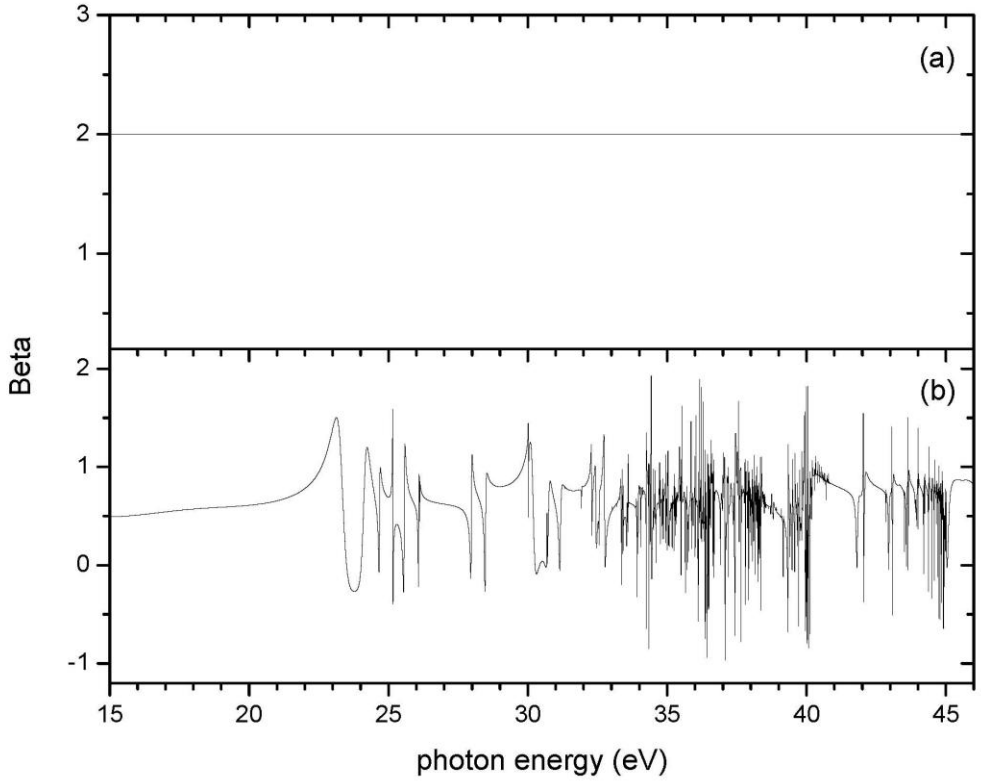

Figure 5.3: Calculated Ca^+ asymmetry parameter beta (p) curves for photon energy from 15.0 to 45.0 eV: (a) initial $^2S^e$ ground state showing $\beta = 2$ for $s \rightarrow p$ transition and (b) initial $^2D^e$ excited state showing β energy dependence for $d \rightarrow p$ and $d \rightarrow f$ transitions.

one final state only, [($3s^2 3p^6$ $^1S^e$) εp $^2P^o$]. The asymmetry parameter β dependence on energy can be clearly seen in figure 5.3(b) for the photoionization of the excited (metastable) [Ne]$3s^2 3p^6 3d$ $^2D^e$ of Ca^+. In this non-relativistic calculations the Photoionization of the $^2D^e$ state involves two transitions ($d \rightarrow p$ and $d \rightarrow f$) leading to final states [($3s^2 3p^6$ $^1S^e$) εp $^2P^o$] and [($3s^2 3p^6$ $^1S^e$) εf $^2F^o$]; since we have at least two

channels, β is energy-dependent [figure 5.3(b)]. Note that if the matrix element for the $d \rightarrow p$ transition vanishes, we would have a constant $\beta = 0.8$. This is quite close to the background value of β seen in figure 5.3(b), indication that the matrix element for the $3d \rightarrow \varepsilon f$ transition is much larger than $3d \rightarrow \varepsilon p$.

5.2.2. Relativistic (Breit-Pauli) Calculations

With the introduction of the spin-orbit interaction in our calculations through the use of the Breit-Pauli *R*-matrix method along with other relativistic effects, the initial states of the Ca^+ ion are characterized as the ground $[Ne]3s^2 3p^6 4s\ ^2S^e_{1/2}$ state, the first excited $[Ne]3s^2 3p^6 3d\ ^2D^e_{3/2}$ state and the second excited $[Ne]3s^2 3p^6 3d\ ^2D^e_{5/2}$ state. The calculated relativistic (Breit-Pauli) cross section for the photoionization of the $Ca^+\ ^2S^e_{1/2}$ initial state is shown in figure 5.4. The individual $^2S^e_{1/2} \rightarrow {}^2P^o_{3/2}$ and $^2S^e_{1/2} \rightarrow {}^2P^o_{1/2}$ cross sections are presented in figures 5.4(a) and 5.4(b) respectively, while the total is given in figure 5.4(c). As in the non-relativistic case, the photoionization spectrum is dominated by autoionizing resonances, but now we distinguish two channels in the ground $Ca^+\ ^2S^e_{1/2}$ initial state cross section: $^2S^e_{1/2} \rightarrow {}^2P^o_{3/2}$ and $^2S^e_{1/2} \rightarrow {}^2P^o_{1/2}$. Among the most important resonances in figure 5.4(a), which correspond to transition $^2S^e_{1/2} \rightarrow {}^2P^o_{3/2}$, we note four narrow and one large and strong resonances: the $^2S^e_{1/2} \rightarrow 3p^5(3d^2\ ^1D)\ ^2P^o_{3/2}$ resonance located at 27.000 eV (1.7 meV width), the $^2S^e_{1/2} \rightarrow 3p^5(4s^2\ ^1S)\ ^2P^o_{3/2}$ resonance located at 28.198 eV (2.3 meV width), the $^2S^e_{1/2} \rightarrow 3p^5(3d^2\ ^1S)\ ^2P^o_{3/2}$ resonance located at 30.169 eV (5.6 meV width), the $^2S^e_{1/2} \rightarrow 3p^5(3d^2\ ^3P)\ ^2P^o_{3/2}$ resonance located at 32.062 eV (10.9

meV width) and the $^2S^e_{1/2} \rightarrow (3p^5 3d\ ^1P)4s\ ^2P^o_{3/2}$ resonance located at 33.226 eV (72.2 meV width).

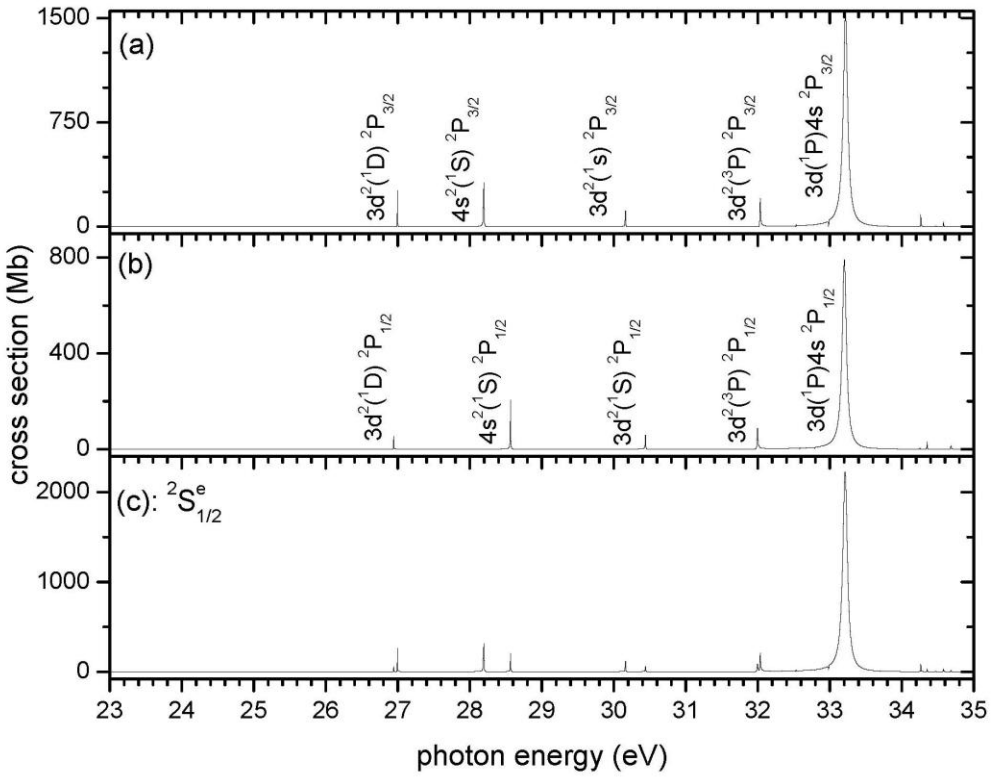

Figure 5.4: Calculated Breit-Pauli photoionization cross sections of the ground $^2S^e_{1/2}$ state of Ca^+ from 23.0 to 35.0 eV showing, (a) the partial cross section to the j=3/2 final state, (b) the partial cross section to the j=1/2 final state, and (c) the total $^2S^e_{1/2}$ cross section, all dominated by the $^2S^e \rightarrow (3p^5 3d\ ^1P)4s\ ^2P^o$ resonance at 33.22 eV. For simplicity $3p^5$ is omitted from each of the resonance designations.

Similarly from figure 5.4(b) for the $^2S^e_{1/2} \rightarrow {}^2P^o_{1/2}$ channel, we find the analogous: the $^2S^e_{1/2} \rightarrow 3p^5(3d^2\ ^1D)\ ^2P^o_{1/2}$ resonance located at 26.947 eV (2.1 meV width), the $^2S^e_{1/2} \rightarrow 3p^5(4s^2\ ^1S)\ ^2P^o_{1/2}$ resonance located at 28.569 eV (1.8 meV width), the $^2S^e_{1/2} \rightarrow 3p^5(3d^2\ ^1S)\ ^2P^o_{1/2}$ resonance located at 30.447 eV (5.3 meV width), the $^2S^e_{1/2} \rightarrow 3p^5(3d^2\ ^3P)\ ^2P^o_{1/2}$ resonance located at 32.022 eV (12.3 meV width) and the $^2S^e_{1/2} \rightarrow (3p^5 3d\ ^1P)4s\ ^2P^o_{1/2}$ resonance located at 33.210 eV (69.7 meV width).

Dominating the $^2S^e_{1/2}$ cross section, however, are clearly the giant $3p \rightarrow 3d$ resonances (see above) identified as $^2S^e_{1/2} \rightarrow (3p^5 3d\ ^1P)4s\ ^2P^o_{3/2}$ in figure 5.4(a) and $^2S^e_{1/2} \rightarrow (3p^5 3d\ ^1P)4s\ ^2P^o_{1/2}$ in figure 5.4(b); their positions and widths are 33.22 eV and 72.2 meV, and 33.20 eV and 69.7 meV, respectively. Although the relativistic interactions cause a splitting of these two resonances, the splitting is so much smaller than the widths that it is unobservable; thus they are equivalent to the single non-relativistic resonance, $^2S^e \rightarrow (3p^5 3d\ ^1P)4s\ ^2P^o$, and was observed in the photoionization of excited $[Ne]3s^2 3p^6 4s\ ^2S^e_{1/2}$ in Sc^{+2} [9-11,93] and excited $[Ne]3s^2 3p^6 4s\ ^2S^e_{1/2}$ of Ti^{+3} (see subsection 4.2.1. above). From our calculations (the present work), this giant resonance is located at 33.30 eV [figure 5.4(c)], and the experimental results [93,98] show it at 33.19 eV; i.e. , an excellent agreement between theory and experiment. We also note excellent agreement in the magnitude of this resonance which is about 2200 Mb both from experimental data [93,98] and theoretical calculations (this work). From Ca^+ to Ti^{+3}, this resonance position, compared to the 4s electron threshold (11.98 eV in Ca^+, 21.86 eV in Sc^{+2} and 33.35 eV in Ti^{+3}), has changed, and decreased from 21.22 eV to 20.18 eV and 15.74 eV (this work) respectively. This tendency in the resonance position to get closer and closer

to the 4s electron threshold, as the nuclear charge Z increases, was observed in experiments [93,98] for Ca^{+} and Sc^{+2}, and should continue with higher Z potassium-like ions. The width of this resonance, on the contrary, increases from Ca^{+} to Sc^{+2} (92.0 and 147 meV) [93,98]; our calculated widths (this work) are 72.2 meV for Ca^{+}, 144 meV for Sc^{+2} and 193.0 meV for Ti^{+3}. This is in agreement with the trend in resonance width to augment as the nuclear charge Z of those ions increases. In addition, this strong spectral line, transition $^2S^e \rightarrow (3p^5 3d\ ^1P)4s\ ^2P^o$, has an oscillator strength [103] calculated (this work) to be 1.87 out of a total of 6 (3p photoexcitation); this is about 31.16 % of the total oscillator strength, an important contribution.

The Breit-Pauli results for the photoionization of the excited (metastable) $^2D^e_{3/2}$ state of Ca^{+} are presented in figure 5.5 for photon energy from 23.0 to 33.0 eV. From the $^2D^e_{3/2}$ ground state, transitions to final states with j =5/2, 3/2 and 1/2 are allowed, and these cross sections are shown in figures 5.5(a), 5.5(b) and 5.5(c) respectively; the total $^2D^e_{3/2}$ photoionization cross section is shown in figure 5.5(d). For this entire photon energy range, resonances are seen to dominate the cross section, although the direct nonresonant photoionization channel is strong enough for interference to occur and produce the asymmetric line shapes, Fano profiles, observed in the cross sections [figures 5.5(a) and 5.5(d)]. The most prominent resonance is located at 29.254 eV with 251.6 meV width, and it is identified as $^2D^e_{3/2} \rightarrow 3p^5(3d^2\ ^3F)\ ^2F^o_{5/2}$, a Δj = 1 transition. This resonance decays *via* a super-Coster-Kronig [105,106] transition ($3p^5 3d^2 \rightarrow 3p^6 + e^-$) that is also observed in the photoionization cross sections of the ground [Ne]$3s^2 3p^6 3d\ ^2D^e$ state of Sc^{+2} [9-11,19,93,107,108] and the ground [Ne]$3s^2 3p^6 3d\ ^2D^e$ state of Ti^{+3} [19,90-

95]; as long as the excitation energy is above the 3*d* ionization threshold, this channel is open and results in this broad giant resonance.

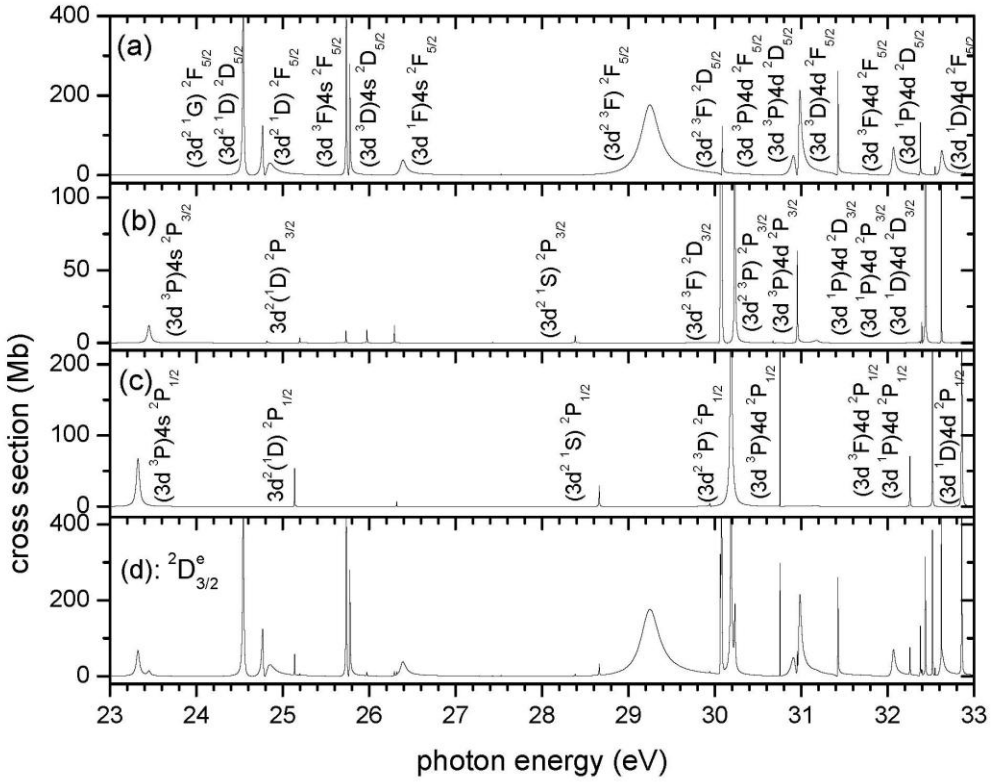

Figure 5.5: Calculated Breit-Pauli photoionization cross sections of the ground $^2D^e_{3/2}$ state of Ca^+ showing, (a) the partial cross section to the j=5/2 final state, (b) the partial cross section to the j=3/2 final state, (c) the partial cross section to the j=1/2 final state, and (d) the total $^2D^e_{3/2}$ cross section, dominated by the $3p^5(3d^2\ ^3F)\ ^2F^o_{5/2}$ resonance at 29.25 eV. For simplicity $3p^5$ is omitted from each of the resonance designations.

When the excitation energy is below the 3*d* ionization threshold, this decay channel is closed, and this is the case for K-like higher Z ions starting with V^{4+} (see section 4). Our

theoretical results show good agreement with experimental data [93,98] that place this resonance at 29.330 eV (with 320.0 meV width). We note here that, compared to the 3*d* ionization threshold, positions of this resonance were [19,93] 19.16 eV in metastable Ca^{+}, 12.38 eV in ground states Sc^{2+} and 0.22 eV in Ti^{3+}; our calculations (this work) show it at positions 19.17, 12.44 and 0.31 eV respectively. This result shows that we have reached good qualitative and quantitative agreement with experimental data [19,93] in reproducing this particularly strong and broad resonance feature, where position along the sequence get closer to the 3*d* ionization threshold as the nuclear charge Z increases.

Besides this large resonance feature described above, many other important resonance structures exist in the case of excited (metastable) $^2D^e_{3/2}$ state of Ca^{+} starting with transitions corresponding to $\Delta j = +1$ observed in figure 5.5(a): the $^2D^e_{3/2} \rightarrow 3p^5(3d^2\ ^1G)\ ^2F^o_{5/2}$ resonance located at 24.545 eV (14.2 meV width), the $^2D^e_{3/2} \rightarrow 3p^5(3d^2\ ^1D)\ ^2D^o_{5/2}$ resonance located at 24.773 eV (17.3 meV width), the $^2D^e_{3/2} \rightarrow 3p^5(3d^2\ ^1D)\ ^2F^o_{5/2}$ resonance located at 24.854 eV (119.6 meV width), the $^2D^e_{3/2} \rightarrow (3p^5 3d\ ^3F)4s\ ^2F^o_{5/2}$ resonance located at 25.737 eV (22.5 meV width), the $^2D^e_{3/2} \rightarrow (3p^5 3d\ ^3D)4s\ ^2D^o_{5/2}$ resonance located at 25.780 eV (6.1 meV width), the $^2D^e_{3/2} \rightarrow (3p^5 3d\ ^1F)4s\ ^2F^o_{5/2}$ resonance located at 26.389 eV (75.3 meV width), the $^2D^e_{3/2} \rightarrow 3p^5(3d^2\ ^3F)\ ^2D^o_{5/2}$ resonance located at 30.089 eV (0.5 meV width), the $^2D^e_{3/2} \rightarrow (3p^5 3d\ ^3P)4d\ ^2F^o_{5/2}$ resonance located at 30.930 eV (63.2 meV width), the $^2D^e_{3/2} \rightarrow (3p^5 3d\ ^3P)4d\ ^2D^o_{5/2}$ resonance located at 30.985 eV (27.8 meV width), the $^2D^e_{3/2} \rightarrow (3p^5 3d\ ^3D)4d\ ^2F^o_{5/2}$ resonance located at 31.432 eV (2.7 meV width), the $^2D^e_{3/2} \rightarrow (3p^5 3d\ ^3F)4d\ ^2F^o_{5/2}$

resonance located at 32.071 eV (38.9 meV width), the $^2D^e_{3/2} \rightarrow (3p^5 3d\ ^1P)4d\ ^2D^o_{5/2}$ resonance located at 32.383 eV (0.6 meV width), the $^2D^e_{3/2} \rightarrow (3p^5 3d\ ^1D)4d\ ^2D^o_{5/2}$ resonance located at 32.553 eV (3.7 meV width) and the $^2D^e_{3/2} \rightarrow (3p^5 3d\ ^1D)4d\ ^2F^o_{5/2}$ resonance located at 32.631 eV (42.8 meV width).

Other important resonances in the photoionization of $Ca^+\ ^2D^e_{3/2}$ are those shown in figures 5.5(b) and 5.5(c) corresponding to $\Delta j = 0$ and $\Delta j = -1$ respectively. Among them are the $^2D^e_{3/2} \rightarrow (3p^5 3d\ ^3P)4s\ ^2P^o_{1/2}$ resonance at 23.326 eV (42.8 meV width) in figure 5.5(c) (a $\Delta j = -1$ transition) and the $^2D^e_{3/2} \rightarrow (3p^5 3d\ ^3P)4s\ ^2P^o_{3/2}$ resonance seen at 23.457 eV (40.9 meV width) in figure 5.5(b). In this last case ($\Delta j = 0$) note the weakness of this resonance in terms of strength and width compared to the previous resonance, it is $\Delta j = -1$ counterpart. Completing the list of resonance features in figure 5.5(b) we have the $^2D^e_{3/2} \rightarrow 3p^5(3d^2\ ^1D)\ ^2P^o_{3/2}$ resonance at 25.202 eV (1.7 meV width), the $^2D^e_{3/2} \rightarrow 3p^5(3d^2\ ^1S)\ ^2P^o_{3/2}$ resonance at 28.388 eV (5.6 meV width), the $^2D^e_{3/2} \rightarrow 3p^5(3d^2\ ^3F)\ ^2D^o_{3/2}$ resonance at 30.081 eV (4.2 meV width), the $^2D^e_{3/2} \rightarrow 3p^5(3d^2\ ^3P)\ ^2P^o_{3/2}$ resonance at 30.243 eV (10.9 meV width), the $^2D^e_{3/2} \rightarrow (3p^5 3d\ ^3P)4d\ ^2P^o_{3/2}$ resonance at 30.968 eV (0.2 meV width), the $^2D^e_{3/2} \rightarrow (3p^5 3d\ ^1P)4d\ ^2P^o_{3/2}$ resonance at 32.439 eV (3.4 meV width) and the $^2D^e_{3/2} \rightarrow (3p^5 3d\ ^1D)4d\ ^2D^o_{3/2}$ resonance at 32.748 eV (3.5 meV width). For figure 5.5(c), following resonances features are shown: the $^2D^e_{3/2} \rightarrow 3p^5(3d^2\ ^1D)\ ^2P^o_{1/2}$ resonance at 25.141 eV (2.1 meV width), the $^2D^e_{3/2} \rightarrow 3p^5(3d^2\ ^1S)\ ^2P^o_{1/2}$ resonance at 28.666 eV (5.3 meV width), the $^2D^e_{3/2} \rightarrow 3p^5(3d^2\ ^3P)\ ^2P^o_{1/2}$ resonance at 30.201 eV

(12.3 meV width), the $^2D^e_{3/2} \rightarrow (3p^5 3d\ ^3P)4d\ ^2P^o_{1/2}$ resonance at 30.776 eV (0.2 meV width), the $^2D^e_{3/2} \rightarrow (3p^5 3d\ ^3F)4d\ ^2P^o_{1/2}$ resonance at 32.261 eV (3.2 meV width), the $^2D^e_{3/2} \rightarrow (3p^5 3d\ ^1P)4d\ ^2P^o_{1/2}$ resonance at 32.522 eV (2.3 meV width) and the $^2D^e_{3/2} \rightarrow (3p^5 3d\ ^1D)4d\ ^2P^o_{1/2}$ resonance 32.862 eV (3.9 meV width).

In figure 5.6, we present the calculated Breit-Pauli results for the corresponding photoionization cross section for the excited $^2D^e_{5/2}$ state of Ca^+ for photon energy from 23.0 to 33.0 eV, and the partial cross sections for j = 7/2, 5/2 and 3/2 final states are shown in figures 5.6(a), 5,6(b) and 5.6(c) respectively. The total photoionization cross section for the $^2D^e_{5/2}$ initial state is shown in figure 5.6(d). The strongest resonance, located at 29.328 eV in figures 5.6(a) and 5.6(d), and due to transition $^2D^e_{5/2} \rightarrow 3p^5(3d^2\ ^3F)\ ^2F^o_{7/2}$, has a width of 263.5 meV (320.0 meV experimentally [93,98]); it is of substantially the same width as the corresponding $^2D^e_{3/2}$ resonance (with 251.6 meV width) at 29.254 eV [figures 5.5(a) and 5.5(d)]. Most resonances seen in figure 5.6 for the $Ca^+\ ^2D^e_{5/2}$ cross sections have their equivalent already listed in the case of $Ca^+\ ^2D^e_{3/2}$ (see above); among are transition $^2D^e_{5/2} \rightarrow 3p^5(3d^2\ ^3F)\ ^2F^o_{5/2}$ seen at 29.238 eV (251.6 meV width) in figure 5.6(b) with $\Delta j = 0$ and $\Delta l = +1$, $^2D^e_{5/2} \rightarrow (3p^5 3d\ ^3P)4s\ ^2P^o_{3/2}$ ($\Delta j = -1$ and $\Delta l = -1$) located at 23.441 eV (40.9 meV width) in figure 5.6(c) and $^2D^e_{5/2} \rightarrow 3p^5(3d^2\ ^3P)\ ^2P^o_{3/2}$ seen at 30.226 eV (10.9 meV width) in figure 5.6(c). Another example of $\Delta j = 0$ but with $\Delta l = 0$ can be seen in figure 5.6(b) at 30.073 eV (0.5 meV width), identified as $^2D^e_{5/2} \rightarrow 3p^5(3d^2\ ^3F)\ ^2D^o_{5/2}$. In addition there are also the $^2D^e_{5/2} \rightarrow (3p^5 3d$

^{1}F)4*s* $^2F^o_{5/2}$, resonance at 26.372 eV (75.3 meV width) in figure 5.6(b) and $^2D^e_{5/2} \rightarrow$ ($3p^5 3d\ ^1$F)4*s* $^2F^o_{7/2}$ at 26.127 eV (57.7 meV width), in figure 5.6(a).

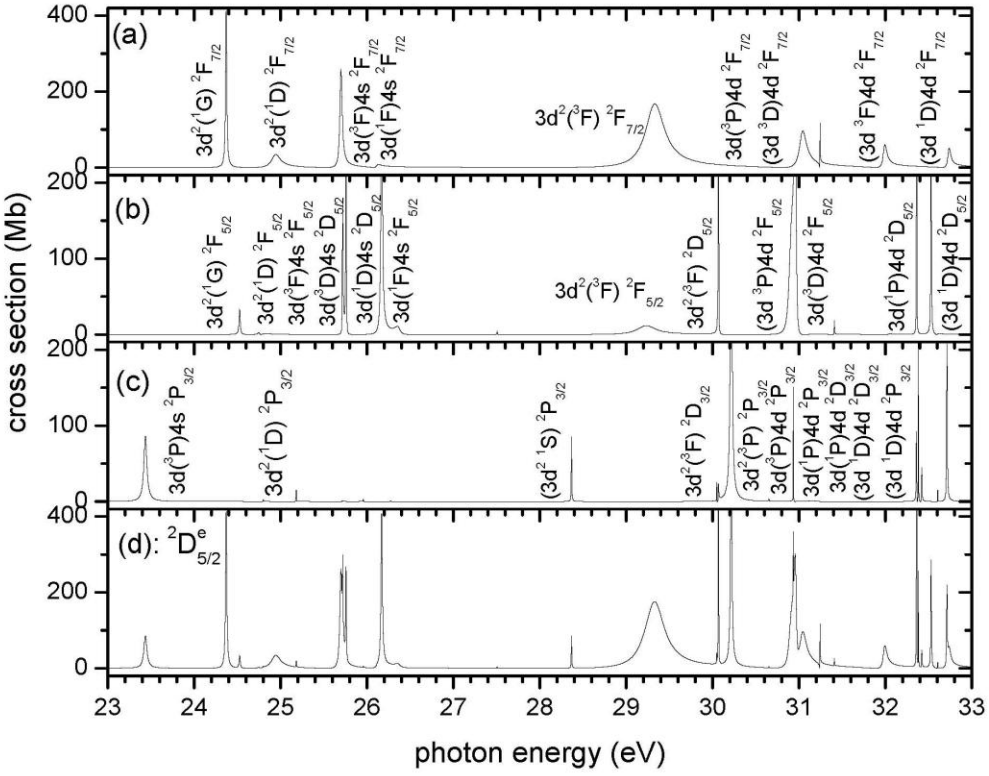

Figure 5.6: Calculated Breit-Pauli photoionization cross sections of the excited (metastable) $^2D^e_{5/2}$ state of Ca^+ showing, (a) the partial cross section to the j=7/2 final state, (b) the partial cross section to the j=5/2 final state, (c) the partial cross section to the j=3/2 final state, and (d) the total $^2D^e_{5/2}$ cross section, dominated by the $3p^5(3d^2\ ^3\text{F})\ ^2F^o_{7/2}$ resonance at 29.328 eV. For simplicity $3p^5$ is omitted from each of the resonance designations.

The fine structure splitting, between $^2D^e_{3/2}$ and $^2D^e_{5/2}$ energy levels of Ca^+ ions, which is ΔE = 0.016 eV (experimental value is 0.008 eV [89]), is also mirrored between following resonance energies: $^2D^e_{3/2} \rightarrow 3p^5(3d^2\ ^3F)\ ^2F^o_{5/2}$ at 29.254 eV in figure 5.5(a) and $^2D^e_{5/2} \rightarrow 3p^5(3d^2\ ^3F)\ ^2F^o_{5/2}$ at 29.238 eV in figure 5.6(b), $^2D^e_{3/2} \rightarrow (3p^5 3d\ ^3P)4s\ \ ^2P^o_{3/2}$ at 23.457 eV in figure 5.5(b) and $^2D^e_{5/2} \rightarrow (3p^5 3d\ ^3P)4s\ \ ^2P^o_{3/2}$ at 25.441 eV in figure 5.6(c) and $^2D^e_{3/2} \rightarrow 3p^5(3d^2\ ^3P)\ ^2P^o_{3/2}$ at 30.243 eV in figure 5.5(b) and $^2D^e_{5/2} \rightarrow 3p^5(3d^2\ ^3P)\ ^2P^o_{3/2}$ at 30.226 eV in figure 5.6(c).

A summary of positions, widths and identifications of the major resonances obtained in the relativistic Breit-Pauli calculation is given in table 5.3, along with a comparison with available experimental data [93,98]. In general the agreement is quite good, especially for the position of $3p^5 3d^2$ resonances, but our calculated widths are, in general, smaller than those from experimental data [93,98]. Note that some of the resonances listed in table 5.3 can be reached by more than one initial state in the experimental mixture, and three of them,[$3p^5(3d^2\ ^3P)\ ^2P^o_{3/2}$, $3p^5(3d^2\ ^1S)\ ^2P^o_{3/2}$ and $3p^5(3d^2\ ^1D)\ ^2P^o_{3/2}$], can be excited from all three initial states; using the example of $3p^5(3d^2\ ^3P)\ ^2P^o_{3/2}$, we clearly can illustrate the previous observation by the following three transitions: $^2D^e_{5/2} \rightarrow 3p^5(3d^2\ ^3P)\ ^2P^o_{3/2}$ at 30.226 eV in figure 5.6(c), $^2D^e_{3/2} \rightarrow 3p^5(3d^2\ ^3P)\ ^2P^o_{3/2}$ at 30.243 eV in figure 5.5(b) and $^2S^e_{1/2} \rightarrow 3p^5(3d^2\ ^3P)\ ^2P^o_{3/2}$ at 32.062 eV in figure 5.4(a). They are listed more than once for purposes of comparison with the experimental results, and they are listed at different photon arises simply because each of the three initial states has a different ionization energy so that differing photon energies are required from each

of these initial states to excite a particular resonance, i.e., the difference in the resonance energies for a given resonance state in the table is just the difference in the binding energies of the initial states of the transitions.

Table 5.3: Theoretical (relativistic Breit-Pauli) resonance energies E_{res} (eV), widths Γ (meV), experimental [93,100] resonance energies E_{res} (eV) and the corresponding transitions.

This Calculation		Transitions	Experiment
E_{res}	Γ		E_{res}
26.947	2.1	$^2S^e_{1/2} \rightarrow 3p^5(3d^2\ ^1D)\ ^2P^o_{1/2}$	
27.000	1.7	$^2S^e_{1/2} \rightarrow 3p^5(3d^2\ ^1D)\ ^2P^o_{3/2}$	
28.569	1.8	$^2S^e_{1/2} \rightarrow 3p^5(4s^2\ ^1S)\ ^2P^o_{1/2}$	28.55
28.198	2.3	$^2S^e_{1/2} \rightarrow 3p^5(4s^2\ ^1S)\ ^2P^o_{3/2}$	28.19
30.447	5.3	$^2S^e_{1/2} \rightarrow 3p^5(3d^2\ ^1S)\ ^2P^o_{1/2}$	30.25
30.169	5.6	$^2S^e_{1/2} \rightarrow 3p^5(3d^2\ ^1S)\ ^2P^o_{3/2}$	29.98
32.022	12.3	$^2S^e_{1/2} \rightarrow 3p^5(3d^2\ ^3P)\ ^2P^o_{1/2}$	
32.069	10.9	$^2S^e_{1/2} \rightarrow 3p^5(3d^2\ ^3P)\ ^2P^o_{3/2}$	
33.210	69.7	$^2S^e_{1/2} \rightarrow (3p^5 3d\ ^1P)4s\ ^2P^o_{1/2}$	33.20
33.226	72.6	$^2S^e_{1/2} \rightarrow (3p^5 3d\ ^1P)4s\ ^2P^o_{3/2}$	33.20
23.326	42.3	$^2D^e_{3/2} \rightarrow (3p^5 3d\ ^3P)4s\ ^2P^o_{1/2}$	
23.441	40.9	$^2D^e_{5/2} \rightarrow (3p^5 3d\ ^3P)4s\ ^2P^o_{3/2}$	
23.457	40.9	$^2D^e_{3/2} \rightarrow (3p^5 3d\ ^3P)4s\ ^2P^o_{3/2}$	
25.141	2.1	$^2D^e_{3/2} \rightarrow 3p^5(3d^2\ ^1D)\ ^2P^o_{1/2}$	
25.186	1.7	$^2D^e_{5/2} \rightarrow 3p^5(3d^2\ ^1D)\ ^2P^o_{3/2}$	
25.202	1.7	$^2D^e_{3/2} \rightarrow 3p^5(3d^2\ ^1D)\ ^2P^o_{3/2}$	
28.666	5.3	$^2D^e_{3/2} \rightarrow 3p^5(3d^2\ ^1S)\ ^2P^o_{1/2}$	
28.371	5.6	$^2D^e_{5/2} \rightarrow 3p^5(3d^2\ ^1S)\ ^2P^o_{3/2}$	
28.388	5.6	$^2D^e_{3/2} \rightarrow 3p^5(3d^2\ ^1S)\ ^2P^o_{3/2}$	
30.201	12.3	$^2D^e_{3/2} \rightarrow 3p^5(3d^2\ ^3P)\ ^2P^o_{1/2}$	30.20
30.226	10.9	$^2D^e_{5/2} \rightarrow 3p^5(3d^2\ ^3P)\ ^2P^o_{3/2}$	30.20

Table 5.3: (continued)

E_{res}	Γ	Transitions	E_{res}
30.968	0.2	$^2\mathrm{D}^e_{3/2} \rightarrow (3p^5 3d\ ^3\mathrm{P})4d\ ^2\mathrm{P}^o_{3/2}$	
32.261	3.2	$^2\mathrm{D}^e_{3/2} \rightarrow (3p^5 3d\ ^3\mathrm{F})4d\ ^2\mathrm{P}^o_{1/2}$	
32.522	2.3	$^2\mathrm{D}^e_{3/2} \rightarrow (3p^5 3d\ ^1\mathrm{P})4d\ ^2\mathrm{P}^o_{1/2}$	
32.422	3.4	$^2\mathrm{D}^e_{5/2} \rightarrow (3p^5 3d\ ^1\mathrm{P})4d\ ^2\mathrm{P}^o_{3/2}$	
32.439	3.4	$^2\mathrm{D}^e_{3/2} \rightarrow (3p^5 3d\ ^1\mathrm{P})4d\ ^2\mathrm{P}^o_{3/2}$	
32.862	3.9	$^2\mathrm{D}^e_{3/2} \rightarrow (3p^5 3d\ ^1\mathrm{D})4d\ ^2\mathrm{P}^o_{1/2}$	
24.545	14.2	$^2\mathrm{D}^e_{3/2} \rightarrow 3p^5(3d^2\ ^1\mathrm{G})\ ^2\mathrm{F}^o_{5/2}$	
24.528	14.2	$^2\mathrm{D}^e_{5/2} \rightarrow 3p^5(3d^2\ ^1\mathrm{G})\ ^2\mathrm{F}^o_{5/2}$	
24.374	15.4	$^2\mathrm{D}^e_{5/2} \rightarrow 3p^5(3d^2\ ^1\mathrm{G})\ ^2\mathrm{F}^o_{7/2}$	
24.773	17.7	$^2\mathrm{D}^e_{3/2} \rightarrow 3p^5(3d^2\ ^1\mathrm{D})\ ^2\mathrm{D}^o_{5/2}$	
24.756	17.7	$^2\mathrm{D}^e_{5/2} \rightarrow 3p^5(3d^2\ ^1\mathrm{D})\ ^2\mathrm{D}^o_{5/2}$	
24.854	119.6	$^2\mathrm{D}^e_{3/2} \rightarrow 3p^5(3d^2\ ^1\mathrm{D})\ ^2\mathrm{F}^o_{5/2}$	
24.837	119.6	$^2\mathrm{D}^e_{5/2} \rightarrow 3p^5(3d^2\ ^1\mathrm{D})\ ^2\mathrm{F}^o_{5/2}$	
24.941	125.1	$^2\mathrm{D}^e_{5/2} \rightarrow 3p^5(3d^2\ ^1\mathrm{D})\ ^2\mathrm{F}^o_{7/2}$	
25.737	22.5	$^2\mathrm{D}^e_{3/2} \rightarrow (3p^5 3d\ ^3\mathrm{F})4s\ ^2\mathrm{F}^o_{5/2}$	
25.721	22.5	$^2\mathrm{D}^e_{5/2} \rightarrow (3p^5 3d\ ^3\mathrm{F})4s\ ^2\mathrm{F}^o_{5/2}$	
25.703	30.7	$^2\mathrm{D}^e_{5/2} \rightarrow (3p^5 3d\ ^3\mathrm{F})4s\ ^2\mathrm{F}^o_{7/2}$	
25.780	6.1	$^2\mathrm{D}^e_{3/2} \rightarrow (3p^5 3d\ ^3\mathrm{D})4s\ ^2\mathrm{F}^o_{5/2}$	
25.763	6.1	$^2\mathrm{D}^e_{5/2} \rightarrow (3p^5 3d\ ^3\mathrm{D})4s\ ^2\mathrm{F}^o_{5/2}$	
26.389	75.3	$^2\mathrm{D}^e_{3/2} \rightarrow (3p^5 3d\ ^1\mathrm{F})4s\ ^2\mathrm{F}^o_{5/2}$	
26.021	57.8	$^2\mathrm{D}^e_{5/2} \rightarrow (3p^5 3d\ ^1\mathrm{F})4s\ ^2\mathrm{F}^o_{7/2}$	
26.372	75.3	$^2\mathrm{D}^e_{5/2} \rightarrow (3p^5 3d\ ^1\mathrm{F})4s\ ^2\mathrm{F}^o_{5/2}$	
26.174	17.6	$^2\mathrm{D}^e_{5/2} \rightarrow (3p^5 3d\ ^3\mathrm{D})4s\ ^2\mathrm{D}^o_{5/2}$	
29.254	251.6	$^2\mathrm{D}^e_{3/2} \rightarrow 3p^5(3d^2\ ^3\mathrm{F})\ ^2\mathrm{F}^o_{5/2}$	29.30

Table 5.3: (continued)

E_{res}	Γ	Transitions	E_{res}
29.328	263.5	$^2D^e_{5/2} \rightarrow 3p^5(3d^2\ ^3F)\ ^2F^o_{7/2}$	29.30
29.238	251.6	$^2D^e_{5/2} \rightarrow 3p^5(3d^2\ ^3F)\ ^2F^o_{5/2}$	29.30
30.089	0.5	$^2D^e_{3/2} \rightarrow 3p^5(3d^2\ ^3F)\ ^2D^o_{5/2}$	30.08
30.081	4.2	$^2D^e_{3/2} \rightarrow 3p^5(3d^2\ ^3F)\ ^2D^o_{3/2}$	30.08
30.073	0.5	$^2D^e_{5/2} \rightarrow 3p^5(3d^2\ ^3F)\ ^2D^o_{5/2}$	30.07
30.064	4.2	$^2D^e_{5/2} \rightarrow 3p^5(3d^2\ ^3F)\ ^2D^o_{3/2}$	30.07
30.930	63.2	$^2D^e_{3/2} \rightarrow (3p^5 3d\ ^3P)4d\ ^2F^o_{5/2}$	
30.913	63.2	$^2D^e_{5/2} \rightarrow (3p^5 3d\ ^3P)4d\ ^2F^o_{5/2}$	
31.041	96.8	$^2D^e_{5/2} \rightarrow (3p^5 3d\ ^3P)4d\ ^2F^o_{7/2}$	
30.985	27.8	$^2D^e_{3/2} \rightarrow (3p^5 3d\ ^3P)4d\ ^2D^o_{5/2}$	
31.432	2.7	$^2D^e_{3/2} \rightarrow (3p^5 3d\ ^3D)4d\ ^2F^o_{5/2}$	
31.415	2.7	$^2D^e_{5/2} \rightarrow (3p^5 3d\ ^3D)4d\ ^2F^o_{5/2}$	
31.249	0.7	$^2D^e_{5/2} \rightarrow (3p^5 3d\ ^3D)4d\ ^2F^o_{7/2}$	
32.071	38.9	$^2D^e_{3/2} \rightarrow (3p^5 3d\ ^3F)4d\ ^2F^o_{5/2}$	
31.995	51.0	$^2D^e_{5/2} \rightarrow (3p^5 3d\ ^3F)4d\ ^2F^o_{7/2}$	
32.385	0.7	$^2D^e_{3/2} \rightarrow (3p^5 3d\ ^1P)4d\ ^2D^o_{5/2}$	
32.414	1.2	$^2D^e_{3/2} \rightarrow (3p^5 3d\ ^1P)4d\ ^2D^o_{3/2}$	
32.368	0.7	$^2D^e_{5/2} \rightarrow (3p^5 3d\ ^1P)4d\ ^2D^o_{5/2}$	
30.397	1.2	$^2D^e_{5/2} \rightarrow (3p^5 3d\ ^1P)4d\ ^2D^o_{3/2}$	
32.631	42.8	$^2D^e_{3/2} \rightarrow (3p^5 3d\ ^1D)4d\ ^2F^o_{5/2}$	
32.641	40.5	$^2D^e_{5/2} \rightarrow (3p^5 3d\ ^1D)4d\ ^2F^o_{7/2}$	
32.748	3.5	$^2D^e_{3/2} \rightarrow (3p^5 3d\ ^1D)4d\ ^2D^o_{3/2}$	
32.539	3.7	$^2D^e_{5/2} \rightarrow (3p^5 3d\ ^1D)4d\ ^2D^o_{5/2}$	

Additional results to complete the Ca^+ resonance analysis are the list of line strengths and oscillator strengths for five of the major resonances from table 5.3, and this is shown in table 5.4. As expected and can be seen in table 5.4, transitions with $\Delta j = 1$ ($^2D^e_{3/2} \rightarrow 3p^5(3d^2\ ^3F)\ ^2F^o_{5/2}$, $^2D^e_{5/2} \rightarrow 3p^5(3d^2\ ^3F)\ ^2F^o_{7/2}$ and $^2S^e_{1/2} \rightarrow (3p^5 3d\ ^1P)4s\ ^2P^o_{3/2}$) have far stronger line strength and oscillator strength than transitions with $\Delta j = 0$ ($^2D^e_{5/2} \rightarrow 3p^5(3d^2\ ^3F)\ ^2F^o_{5/2}$ and $^2S^e_{1/2} \rightarrow (3p^5 3d\ ^1P)4s\ ^2P^o_{1/2}$).

Table 5.4: Ca II (Ca^+) line strength (S) and oscillator strength (f) for five of the major resonances.

Transitions	Δj	S (a.u.)	f
$^2D^e_{3/2} \rightarrow 3p^5(3d^2\ ^3F)\ ^2F^o_{5/2}$	1	3.096	0.369
$^2D^e_{5/2} \rightarrow 3p^5(3d^2\ ^3F)\ ^2F^o_{7/2}$	1	4.151	0.373
$^2S^e_{1/2} \rightarrow (3p^5 3d\ ^1P)4s\ ^2P^o_{3/2}$	1	6.095	1.241
$^2D^e_{5/2} \rightarrow 3p^5(3d^2\ ^3F)\ ^2F^o_{5/2}$	0	0.218	0.026
$^2S^e_{1/2} \rightarrow (3p^5 3d\ ^1P)4s\ ^2P^o_{1/2}$	0	1.533	0.624

To compare our theoretical calculation results to experimental data, we use results for photoionization of Ca^+ ions reported by Schippers *et al* [98] and Kjeldsen *et al* [93,100], and unlike what we were able to do in previously studied cases (see above) such as Sc^{+2} and Ti^{+3} ions, where we have obtained numerical experimental data from Schippers *et al* [9,10,19], and plotted them in one graph for comparison with our theoretical results, this was not available for Ca^+. Thus, theoretical and experimental results are shown in different figures (5.7 and 5.8). In the experiment from Kjeldsen *et al* [93,100], results were recorded (figure 5.8) with different fractions of the metastable Ca^+ ions (1.0 %, 26.0 %, 100.0 % and 0.0 %), and the photon energy range is from 28.0 to

30.5 eV. We used those different fractions of the metastable Ca^+ ions in the experimental mixture, to obtain Ca^+ total photoionization cross sections that are shown in figure 5.7; it is clear that, comparing figures 5.7 and 5.8, relatively good agreement is reached with experimental results [93,100]. However, in figures (5.7 and 5.8), we observe differences in some of the resonance cross section magnitudes; as an illustration of this, the resonance structure due to transition $^2D^e \rightarrow 3p^5(3d^2\ ^3P)\ ^2P^o$, located at 30.2 eV [figures 5.7(d) and 5.8(d)], is calculated (this work) to maximize at 550 Mb [figure 5.7(d)] while the experimental magnitude [93,100] is 275 Mb [figure 5.8(d)]. We note that despite the narrow photon energy range (2.5 eV wide), the agreement between our calculated resonance positions (figure 5.7) and the experimental positions [93,100] (figure 5.8) is excellent, and most of our cross section magnitudes seen in figure 5.7 match their experimental counterparts observed in figure 5.8, or are within the margin of error which is 15 % for the experiments considered here [93,100].

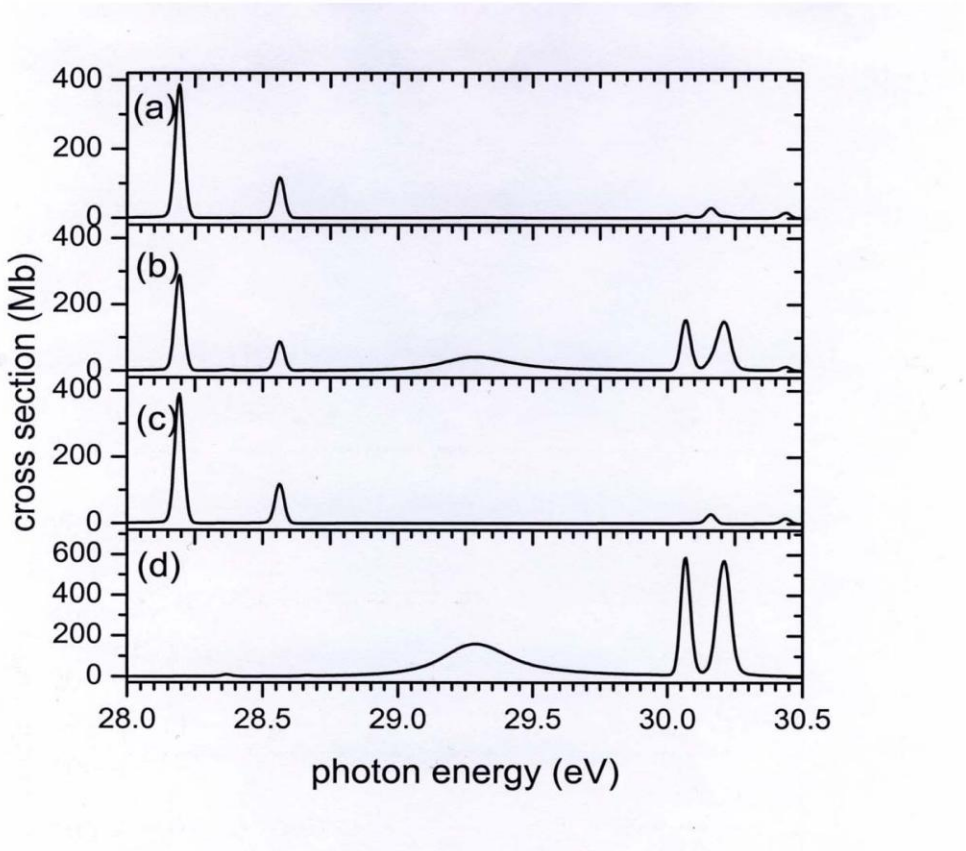

Figure 5.7: Calculated Breit-Pauli photoionization cross sections of Ca^+ ions showing, (a) 1 % of excited (metastable) $^2D^e$ and 99 % of ground $^2S^e$ states, (b) 26 % of excited (metastable) $^2D^e$ and 74 % of ground $^2S^e$ states, (c) 0 % of excited (metastable) $^2D^e$ and 100 % of ground $^2S^e$ states and (d) 100 % of excited (metastable) $^2D^e$ and 0 % of ground $^2S^e$ states.

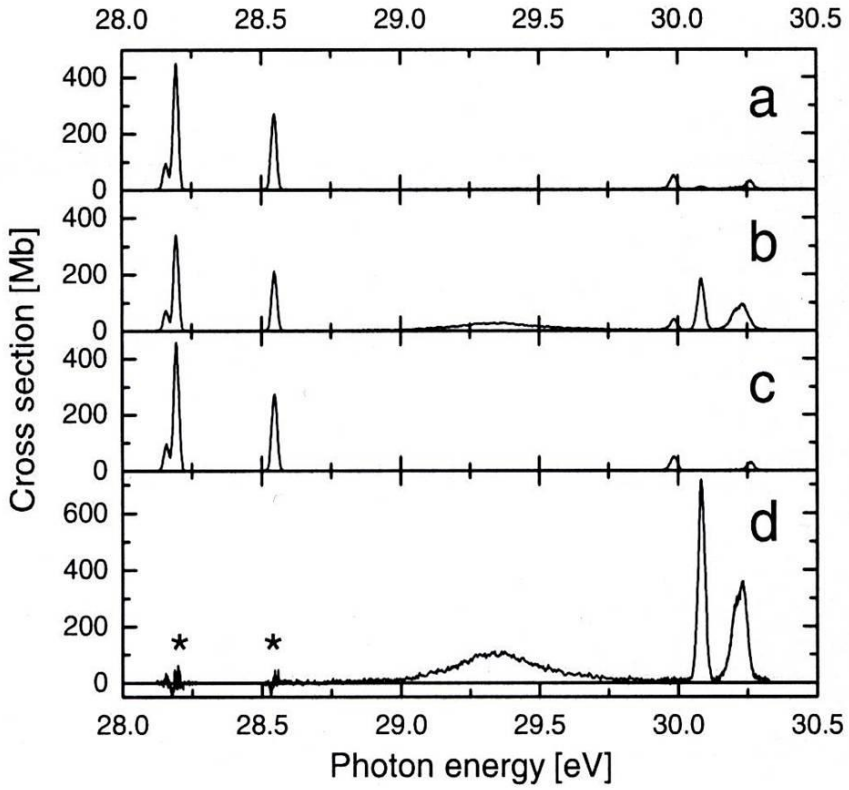

Figure 5.8: Experimental state-selective measurements of absolute photoionization cross sections for Ca^+ 3*d* and 4*s* ions by Kjeldsen *et al* [93,100]. The data correspond to fractions of metastable ions of x = 1 % (a), x = 26 % (b), x = 0 % only ground state ions (c) and x = 100 % (only metastable ions) (d), respectiviely. The upper spectra (a) and (b) are recorded directly, wheareas (c) and (d) are derived from these. The structures marked by asterisks in (d) are experimental artifacts.

5.2.3. Comparison along the Isoelectronic Sequence

It was noted in previous and current chapters that, for some members of the potassium isoelectronic sequence such as Ca^+, Sc^{+2} and Ti^{+3}, the photoionization cross section exhibited very strong resonance structures due to giant $3p \rightarrow 3d$ dipole transitions followed by autoionization to continuum states (super-Coster-Kronig processes).

Considering three K-like ions (Ca^{+}, Sc^{+2} and $Ti^{+3)}$, we distinguish two types of sequences: the 4*s* sequence and the 3*d* sequence. The 4*s* sequence is described as K-like ions which initial state has the electronic configuration $[Ne]3s^2 3p^6 4s\ ^2S^e_{1/2}$; this includes the ground state of Ca^{+} and the second excited state (third excited state relativistic ally) of Sc^{+2} and Ti^{+3}. The 3*d* sequence, meanwhile, is described with each of the two initial states $[Ne]3s^2 3p^6 3d\ ^2D^e_{3/2}$ and $[Ne]3s^2 3p^6 3d\ ^2D^e_{5/2}$; it includes the ground and first excited states of Sc^{+2} and Ti^{+3} and the first two excited states of Ca^{+}.

The 4*s* sequence comparison is shown in figure 5.9, and we focus particularly on the strongest resonance feature in those cross sections, the resonance identified as $^2S^e \rightarrow (3p^5 3d\ ^1P)4s\ ^2P^o$. Figure 5.9(a) depicts Ca^{+} photoionization, figure 5.9(b), Sc^{+2} and figure 5.9(c) Ti^{+3} ions, all in the $^2S^e_{1/2}$ initial state, and those photoionization cross sections are expressed as functions of photoelectron energies for sensible comparison. As we see, in figure 5.9, the magnitude of this resonance decreases from Ca^{+} [figure 5.9(a)] to Sc^{+2} [figure 5.9(b)] and Ti^{+3} [figure 5.9(c)] while the width increases at the same time from Ca^{+} to Ti^{+3}.

The 3*d* sequence comparison is shown in figures 5.10 and 5.11, and we again focus particularly on the strongest resonance feature in those cross sections, the $^2D^e_{3/2} \rightarrow 3p^5(3d^2\ ^3F)\ ^2F^o_{5/2}$ (figure 5.10) and $^2D^e_{5/2} \rightarrow 3p^5(3d^2\ ^3F)\ ^2F^o_{7/2}$ (figure 5.11). Figure 5.10(a) concerns Ca^{+} , figure 5.10(b) Sc^{+2} and figure 5.10(c) Ti^{+3}, all in the $^2D^e_{3/2}$ initial state, and similarly for figure 5.11, but for the $^2D^e_{5/2}$ initial state. In both figures 5.10 and 5.11 we observe the same tendency in the evolution of magnitude and width Ca^{+} to Ti^{+3}; as the nuclear charge Z increases from Ca^{+} to Ti^{+3} (Z = 20 to Z = 22), the positions of

each of the resonance associated with transitions $^2S^e \rightarrow (3p^5 3d\ ^1P)4s\ ^2P^o$ (figure 5.9), $^2D^e_{3/2} \rightarrow 3p^5(3d^2\ ^3F)\ ^2F^o_{5/2}$ (figure 5.10) and $^2D^e_{5/2} \rightarrow 3p^5(3d^2\ ^3F)\ ^2F^o_{7/2}$ (figure 5.11) move closer to the ionization threshold, the 4*s* ionization threshold for the 4*s* sequence and the 3*d* ionization threshold for the 3*d* sequence.

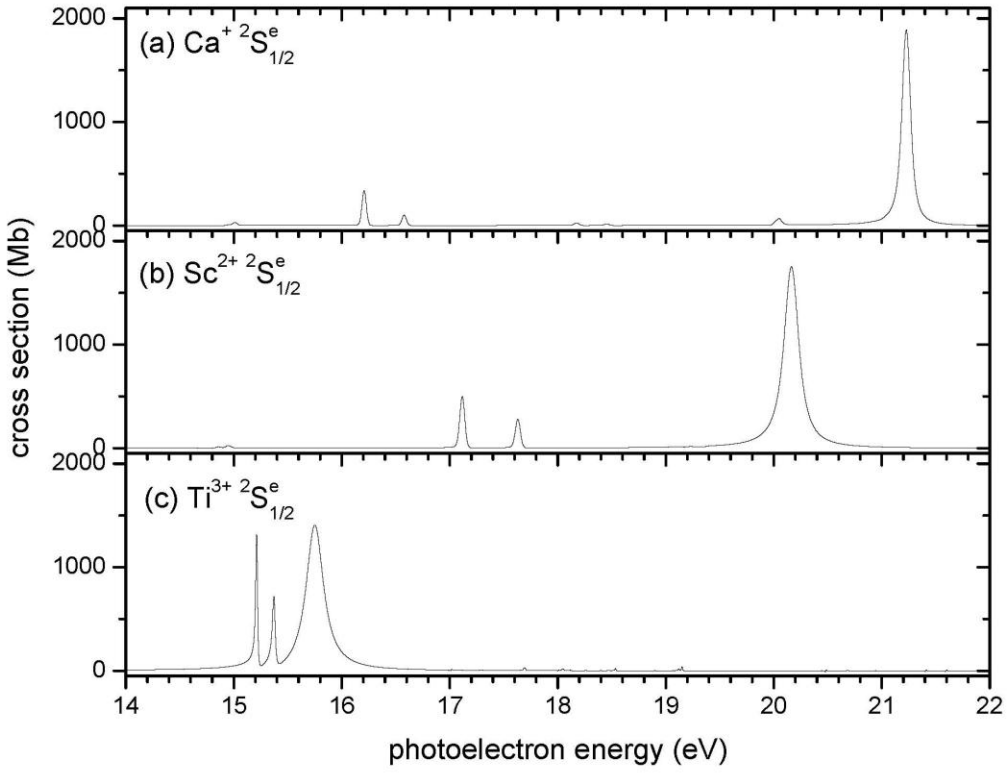

Figure 5.9: Photoionization cross sections of potassium-like ions in the $^2S^e_{1/2}$ state showing, (a) ground state Ca^+, (b) excited state Sc^{+2} and (c) excited state Ti^{+3}. Note, as we go from Ca^+ to Ti^{+3}, the strongest and largest resonance feature, due to transition $^2S^e \rightarrow (3p^5 3d\ ^1P)4s\ ^2P^o$, the width increases, the magnitude decreases, and the position moves closer to 4*s* electron ionization threshold.

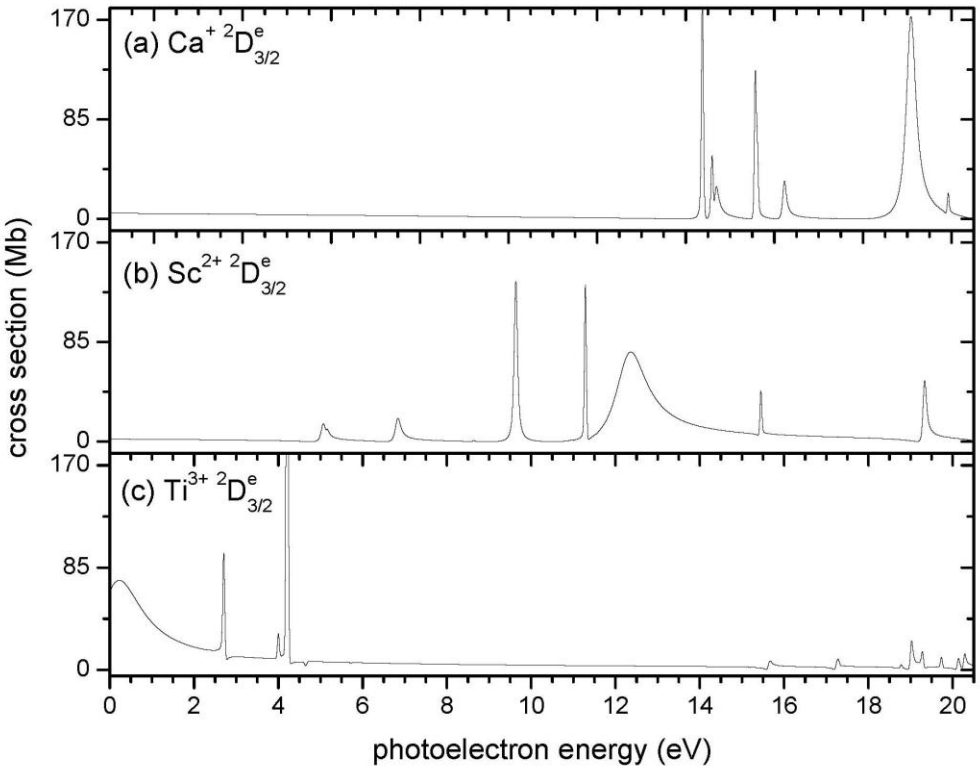

Figure 5.10: Photoionization cross sections of potassium-like ions in the $^2D^e_{3/2}$ state showing, (a) excited state Ca^+, (b) ground state Sc^{+2} and (c) ground state Ti^{+3}. Note, as we go from Ca^+ to Ti^{+3}, the strongest and largest resonance feature due to $^2D^e_{3/2} \rightarrow 3p^5(3d^2\ ^3F)\ ^2F^o_{5/2}$, the width increases, the magnitude decreases, and the position moves closer to 3*d* ionization threshold.

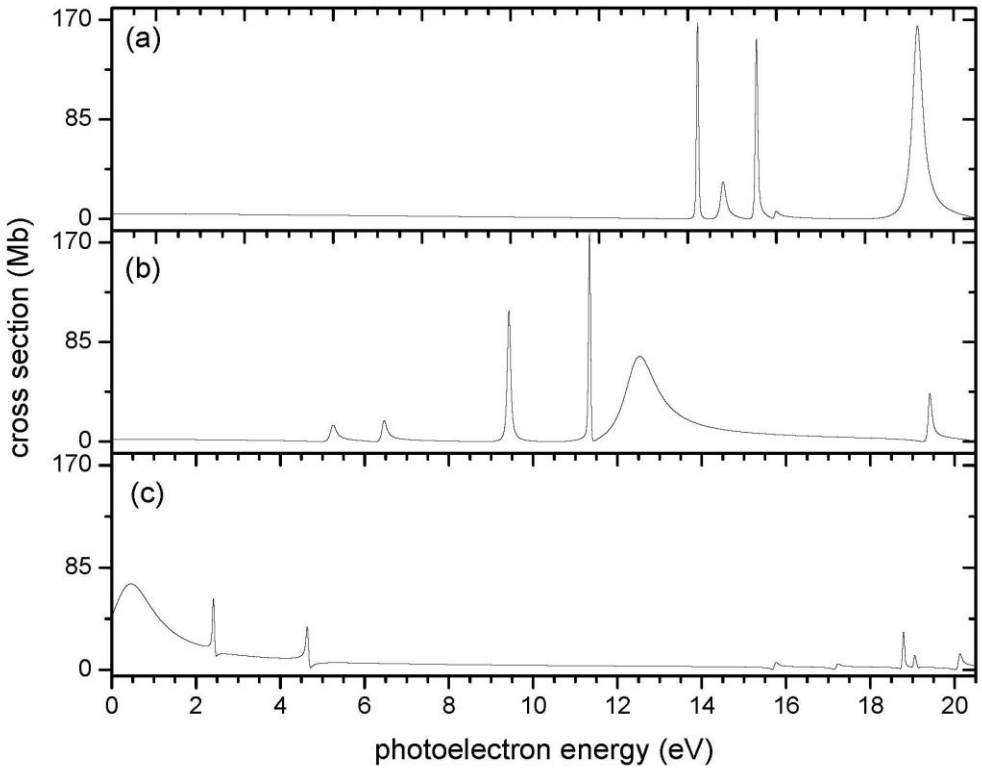

Figure 5.11: As figure 5.10 but for the ${}^2\mathrm{D}^e_{5/2}$ intitial state.

5.3. Conclusion

We have performed non-relativistic (LS-coupling) and relativistic (Breit-Pauli) photoionization cross section calculation for ground and excited states of Ca^+ ions. Our theoretical results have achieved good agreement with experimental data [93,98,100], especially in terms of positions of major resonances. The Ca^+ photoionization cross section spectra reveal the presence of giant $3p \rightarrow 3d$ resonances, and the same strong resonance structures were observed in K-like transition metals ions studied above such as Sc^{+2} (chapter 3) and Ti^{+3} (chapter 4), which indicated the desirability of a study of those strong resonance features along the isoelectronic sequence with two types of

comparisons, the 4*s* sequence and the 3*d* sequence. From this comparison, it was observed that the strongest and broadest resonance feature of each of those two sequences evolved the same way as in experiment [9,10,19,93,98,100]; as the nuclear charge Z increases from Ca^{+} to Ti^{+3}, the width increases, the magnitude decreases, and the position is closer to the ionization threshold (4*s* or 3*d*).

For the photoionization cross section calculations for Ca^{+}, we must point out that our calculated widths for resonances due to transitions $^2S^e \rightarrow (3p^5 3d\ ^1P)4s\ ^2P^o$, $^2D^e_{3/2} \rightarrow 3p^5(3d^2\ ^3F)\ ^2F^o_{5/2}$ and $^2D^e_{5/2} \rightarrow 3p^5(3d^2\ ^3F)\ ^2F^o_{7/2}$ are all smaller than their experimental counterparts [93,93,100], but this difference in width values represents the only discrepancies between the present theory and experiment [93,98,100].

CHAPTER 6.

CONCLUDING REMARKS

In this work we have performed photoionization cross section calculations for potassium-like ions including transition metal ions (Sc^{+2}, Ti^{+3}, V^{+4}, Cr^{+5}, Mn^{6+} and Fe^{7+}) and Ca^{+} ions using both non-relativistic (LS-coupling) and relativistic (Breit-Pauli) *R*-matrix methods. Our theoretical results show good agreement with available experimental data; this is the case of Ca^{+}, Sc^{+2} and Ti^{+3}. For the four other potassium-like ions (V^{+4}, Cr^{+5}, Mn^{6+} and Fe^{7+}), we were unable to confirm our theoretical results because up to date, there are no available experiment data in those cases. We also included in this work the first photoionization cross section calculation results on the excited state of Ti^{+3} ($[Ne]3s^2 3p^6 4s\ ^2S^e_{1/2}$). It is found that in the case of lower Z ($22 \geq Z \geq 20$) ions (Ca^{+}, Sc^{+2} and Ti^{+3}), the photoionization cross section spectra are dominated by the giant ($3p \rightarrow 3d$ excitation) resonances, while those of higher Z ($30 \geq Z \geq 23$) ions (V^{+4}, Cr^{+5}, Mn^{+6}, Fe^{+7}, Co^{+8}, Ni^{+9}, Cu^{+10} and Zn^{+11}) are dominated by the higher members of the Rydberg series. The giant ($3p \rightarrow 3d$ excitation) resonances have moved below the ionization threshold in this case.

Aside from the specifics of the particular ions studied herein, the results can be broadly generalized to other systems as well. It is evident that, in general, along any isoelectronic sequence, more and more of the oscillator strength will move into the discrete region, with increasing Z. Since more of the oscillator strength is in the discrete excitation region, with increasing Z, there are fewer photoelectrons produced; this is important in the modeling of astrophysical and laboratory plasmas. In addition, it is also clear that the strength and width of resonances arising from $\Delta n = 0$ transitions are far

larger than the resonances which arise from transitions between states of different principal quantum number. This will be true for atoms and ions throughout the periodic table.

Another broad generalization can be made regarding the role of relativistic interactions at relatively low Z. These interactions were seen to cause splittings and shifts of thresholds and resonance positions, and these are not limited to the particular ions studied herein. In addition, it was found that, in certain cases, the breakdown of LS coupling engendered by relativistic interactions opened photoionization channels that were absolutely forbidden within the context of LS coupling, and the cross sections of these LS-forbidden channels were not small. Clearly these phenomena too are quite general and not limited to the ions studied. Thus, for quantitative accuracy (and, in some situations, even qualitative accuracy) relativistic effects must be included in photoionization calculations of all atoms and ions with $Z \geq 20$ or so.

Finally, the experience of the present calculations has taught us that the representation of the wave function for the 3*d* electron is of crucial importance for these open 3*d*-subshell ions, owing to the fact that the effective *d*-wave potential has a double well [110]; this means that, depending upon the specific LSJ state, the 3*d* can be bound in the inner well, in the outer well, or balanced between them. Only for high enough Z that the 3*d* subshell is closed (or nearly closed) is the 3*d* bound in the inner well in all states and relatively insensitive the specific LSJ state. This will be the case for all open-shell 3*d* atoms and ions, and for the 4*d* and 5*d* transition metals as well, and great care must be taken to expand these orbitals using a large enough basis set to be able to represent them

accurately for all of the relevant LSJ states. And, the same will be true for open f-subshell atoms and ions the *f*-wave potential is also double-welled.

The fact that we were able to reproduce existing experimental photoionizaiton cross section results in cases of potassium-like ions such as Ca^{+}, Sc^{+2} and Ti^{+3} with rather good agreement (without any shift in energy positions) using the *R*-matrix computer package, is clear evidence that the *R*-matrix method includes all of the important physical effects relevant to the photoionization process, i.e., *R*-matrix is one of the best tools available to study dynamical processes involving complex atomic and ionic systems. However, far for being an end, this study is just the beginning stage of a larger effort to investigate the photoionization of complex atomic and ionic systems in general and transition metals in particular; our investigation will be extended to neutral atoms such as atomic scandium, and continue with other transition metals with higher Z and then on to other open *d*- and open *f*-subshell atoms and ions. The interest of studying the atomic scandium is explained by the fact that it is the simplest 3*d* electron atom (one single *d* electron in the outer shell), but until now there is no theoretical photoionization study to reproduce, in an accurate way, experimental results.

Despite the strength and robustness (state of the art) of the classical (Belfast) *R*-matrix computer package (codes), we note that the use of this package to deal with complex atomic and ionic system comes with some problems. For $Z > 30$, the relativistic (Breit-Pauli) method is no longer a valid approximation; this means we need to consider the fully relativistic *R*-matrix package (DARC), but DARC applications have been rare, and mostly limited to highly ionized systems, and even in this case it is employed for scattering and rarely for photoionization. Another weakness of the classical *R*-matrix is

the control of the Hamiltonian matrix size in treating complex systems; dealing with complex atoms and ions requires the use of large numbers of orbitals and pseudo-orbitals that increase the size of the Hamiltonian matrix to the point that it exceeds what can be treated with existing computational technology. It is hoped that the announced advent of the fully relativistic *B*-Splines *R*-matrix package will bring much needed improvement, and allow us to accurately study dynamical processes involving complex atoms and ions such as those open *d*- and open *f*-subshell atoms and ions.

REFERENCES

[1] *New Directions in Research With Third-Generation Soft X-Ray Synchrotron Radiation Sources*, Vol. 254, NATO Advanced Study Institute Series E: Applied Sciences, edited by A. S. Schlachter and F. J. Wuilleumier (Kluwer, Dordtecht, 1992).

[2] B. Sonntag and P. Zimmerman, Rep. Prog. Phys. **55**, 911 (1992).

[3] Z. Altun and S. T. Manson, Europhys. Lett. **33**, 17 (1996).

[4] Z. Altun and S. T. Manson, Phys. Rev. A **59**, 3576 (1999).

[5] M. Martins, J. Phys. B **35**, L223 (2002).

[6] K. Tiedtke, Ch. Gerth, M. Martins, B. Obst and P. Zimmermann, J. Phys. B **33**, L755 (2000).

[7] S. B. Whitfield, K. Kenoe, R. Wehlitz, M. O. Krause and C. D. Caldwell, Phys. Rev. A **64**, 022701 (2001).

[8] S. B. Whitfield, K. Caspary, T. Myers, M. Bjelland, R. Wehlitz, J. Jiméniz-Mier, P. Olalde-Velasco and M. O. Krause, J. Phys. B **38**, 3273 (2005).

[9] S. Schippers, A. Müller, S Ricz, M. E. Bannister, G. H. Dunn, J. Bozek, A. S. Schlachter, G. Hinojosa, C. Cisneros, A. Aguilar, A. M. Covington, M. F. Gharaibeh and R. A. Phaneuf, Phys. Rev. Lett. **89**, 193002 (2002).

[10] S. Schippers, A. Müller, S Ricz, M. E. Bannister, G. H. Dunn, A. S Schlachter, G. Hinojosa, C. Cisneros, A. Aguilar, A. M. Covington, M. F. Gharaibeh and R. A. Phaneuf, Phys. Rev. A **67**, 032702 (2003).

[11] J. Zeng, G. Zhao and J. Yuan, Phys. Rev. A **68**, 022714 (2003).

[12] Z. Altun and S. T. Manson, J. Phys. B **32**, L255 (1999).

[13] W. Eissner, M. Jones and H. Nussbaumer, Comput. Phys. Commun. **8**, 270 (1974).

[14] UK APAP Codes: http://amdpp.phys.strath.ac.uk/tamoc/code.html

[15] K. A. Berrington, W. B. Eissner and P. H. Norrington, Comput. Phys. Commun. **92**, 290 (1995).

[16] K. Berrington, L. Quigley and J. Pelan, Comput. Phys. Commun. **114**, 225 (1998).

[17] L. Quigley and K. Berrington, J. Phys. B **29** 4529 (1996).

[18] J. M. Ramirez and M. A. Bautista, J. Phys. B **35** 4139 (2002).

[19] S. Schippers, A. Müller, R. A. Phaneuf, T. van Zoest, I. Álvarez, C. Cisneros, E. D. Emmons, M. F. Gharaibeh, G. Hinojosa, A. S. Schlachter and S. W. J. Scully, J. Phys. B **37**, L209 (2004).

[20] P. G. Burke and W. D. Robb, in *Advances in Atomic and Molecular Physics* **11**, 143 (1975).

[21] P. G. Burke, C. J. Noble and V. M. Burke, in *Advances in Atomic, Molecular and optical Physics* **54**, 237 (2007).

[22] E. P. Wigner, Phys. Rev. **70**, 15 (1946).

[23] E. P. Wigner, Phys. Rev. **70**, 606 (1946).

[24] E. P. Wigner and L Eisenbud, Phys. Rev. **72**, 29 (1947).

[25] A. M. Lane and R. G. Thomas, Rev. Mol. Phys. **30**, 257 (1958).

[26] G. Breit, *Handbuch der Physik*, Vol. 4171 (Springer-Verlag, Berlin, 1959).

[27] C. Mahaux and H. A. Weidenmüller, *Shell-Model Approach to Nuclear Reactions* (North-Holland, Amsterdam, 1969).

[28] P. G. Burke, A. Hibbert and W. D. Robb, J. Phys. B **4**, 153 (1971).

[29] P. G. Burke and M. J. Seaton, in *Methods in Computational Physics* (Academic Press, New-York, 1971) Vol. 10, pp. 1-80.

[30] O. Zatsarinny, Comput. Phys. Commun. **174**, 273 (2006).

[31] P. G. Burke and K. A. Berrington, *Atomic and Molecular Processes: An R-matrix Approach* (IOP Publishing, Bristol, 1993).

[32] http://heasarcgsfc.nasa.gov/topbase//op.html.

[33] http://www.usm.uni-muenchen.de/people/ip/iron-project.html.

[34] K. A. Berrington, P. G. Burke, J. J. Chang, A. T. Chivers, W. D. Robb and K. T. Taylor, Comput. Phys. Commun. **8**, 149 (1974).

[35] K. A. Berrington, P. G. Burke, M. LeDourneuf, W. D. Robb, K. T. Taylor and Vo Ky Lan, Comput. Phys. Commun. **14**, 365 (1978).

[36] N. S. Scott and K. T. Taylor, Comput. Phys. Commun. **25**, 347 (1982).

[37] A. G. Sunderland, C. J. Noble, V. M. Burke and P. G. Burke, Comput. Phys. Commun.**143**, 311 (2002).

[38] K. G. Dyall, I. P. Grant, C. T. Johnson, F. A. Parpia and E. P. Plummer, Comput. Phys. Commun. **55**, 425 (1989).

[39] F. A. Parpia, C. Froese Fischer and I. P. Grant, Comput. Phys. Commun. **94**, 249 (1996).

[40] P. Jönsson, X. He, C. Froese Fischer and I. P. Grant, Comput. Phys. Commun. **177**, 597 (2007).

[41] P. H. Norrington and I. P. Grant, J. Phys B **20**, 4869 (1987).

[42] http://web.am.qub.ac.uk/DARC/.

[43] G. V. Marr, in *Photoionization Processes in Gases* (Academic Press, New York, 1967).

[44] P. G. Burke, in *Atomic Processes and Applications*, Ed. P. G. Burke and B. L. Moiseiwitsch (North-Holland, Amsterdam, 1976), chap 7, p. 199.

[45] A. F. Starace, in *Atomic Data Workshop: Assessment of data for photo-ionization and photo-excitation and for electron impact excitation of atomic ions*, Ed. W. Eissner and A. E. Kingston (SERC Daresbury Laboratory, 1987), p. 1-6.

[46] A. F. Starace, in *Atomic, Molecular and Optical Physics Handbook*, Ed. G. W. F. Drake (AIP Press NewYork, 1996), Chap. 24, p. 301.

[47] M. Ya. Amusia, *Atomic Photoeffect* (Plenum Press, New York, 1990).

[48] P. G. Burke and K. T. Taylor, J. Phys. B **8**, 2620 (1975).

[49] S. M. Balley, Ph. D. Thesis: *Relativistic Atomic Photoionization*, Queen's University of Belfast, Belfast, UK, (1997).

[50] A. Hibbert, Comput. Phys. Commun. **9**, 141 (1975).

[51] N. R. Badnell, J. Phys. B **19**, 3827 (1986).

[52] N. R. Badnell, J. Phys. B **30**, 1 (1997).

[53] H. Nussbaumer and P. J. Storey, Astron. Astrophys. **70**, 37 (1978).

[54] W. D. Robb, Comput. Phys. Commun. **1**, 457 (1970).

[55] J. P. A. Buttle, Phys. Rev. **160**, 79 (1967).

[56] K. A. Berrington, P. G. Burke, K. Butler, M. J. Seaton, P. J. Storey, K. T. Taylor and Yu Yan, J. Phys. B **20**, 6379 (1987).

[57] M. J. Seaton, J. Phys. B **18**, 2111 (1985).

[58] P. G. Burke and H. M. Schey, Phys. Rev. **126**, 147 (1962).

[59] P. G. Burke, D. D. McVicar and K. Smith, Proc. Phys. Soc. London **83**, 397 (1964).

[60] M. Gailitus, J. Phys. B **9**, 843 (1976).

[61] C. J. Noble and R. K. Nesbet, Comput. Phys. Commun. **33**, 399 (1984).

[62] G. Breit and H. A. Bethe, Phys. Rev. **83**, 888 (1954).

[63] R. J. W. Henry and L. Lipsky, Phys. Rev. **153**, 51 (1967).

[64] P. G. Burke and M. J. Seaton, J. Phys. B **17**, L683 (1985).

[65] L. I. Schiff, *Quantum Mechanics*, first edition (McGraw-Hill Book Co. New York, 1949,), p. 242.

[66] S. Chandrasekhar, Astrophys. J. **102**, 223 (1945).

[67] A. F. Starace, Phys. Rev. A **3**, 1242 (1971).

[68] A. F. Starace, Phys. Rev. A **8**, 1141 (1973).

[69] I. P. Grant, J. Phys. B **7**, 58 (1974).

[70] I. P. Grant and A. F. Starace, J. Phys. B **8**, 1999 (1975).

[71] E. Wigner, Z. Physik **43**, 624 (1927); C. Eckart, Rev. Mod. Phys. **2**, 305 (1930).

[72] R. D. Cowan in, *The Theory of Atomic Structure and Spectra*, Los Alamos Series in Basic and Applied Sciences (University of California Press, Berkeley, 1981), p. 307-308.

[73] U. Fano and G. Racah, *Irreducible Tensorial Sets* (New York: Academic Press, 1959).

[74] M. E. Rose, *Elementary Theory of Angular Momentum* (John Wiley and Sons Inc., New York, 1957), p. 106.

[75] C. Froese-Fischer, T. Brage and P. Jönsson, *Computational Atomic Structure: An MCHF Approach* (IOP publishing, Bristol, 1997), p. 227.

[76] W. Thomas and F. Reiche, Naturwissenschaften **13**, 627 (1925).

[77] W. Kuhn, Z. Phys. **33**, 408 (1925).

[78] H. A. Bethe and E. E. Salpeter, *Quantum mechanics of One- and Two-Electron Atoms* (Springer-Verlag, Berlin, 1957).

[79] G. Racah, Phys. Rev. **61,** 537 (1942).

[80] N. S. Scott and P. G. Burke, J. Phys. B **13**, 4299 (1980).

[81] O. Bely, D. Moores and M. J. Seaton, in *Atomic Collision Processes*, Ed. M. McDowell (North-Holland, Amsterdam, 1963), p. 304.

[82] U. Fano, Phys. Rev. **124**, 1866 (1961).

[83] U. Fano and J. W. Cooper, Phys. Rev. **137**, A1364 (1965).

[84] G. Breit and E. P. Wigner, Phys. Rev. **49,** 519 (1936).

[85] S. T. Manson, in *Many-bodyAtomic Physics*, Edited by J. J. Bolle and M. S. Pindzola (Cambridge University Press, Cambridge, 1998), chap. 7, p. 167.

[86] C. N. Yang, Phys. Rev. **74**, 764 (1948).

[87] J. Cooper and R. N. Zare, *Lectures in Theoretical Physics*, edited by S. Geltman, K. T. Mahanthappa and W. E. Britten (Gordon and Breach, New York, 1969), Vol. XI-C, pp. 317-337.

[88] M. Born and E. Wolf, *Principles of Optics* (Pergamon Press, New York, 1959) Subsection 10.8.2.

[89] NIST: http://physics.nist.gov/PhysRefData/ASD/levels_form.html

[90] S. N. Tiwary, A. E. Kingston and A. Hibbert, J. Phys. B **16**, 2457 (1983).

[91] T. W. Gorczyca, M. S. Pindzola, D. C. Griffin and N. R. Badnell, J. Phys. B **27**, 2399 (1994).

[92] A. N. Ryabtsev, S. S. Churilov and Ya É. Kononov, Opt. Spectrosc. Vol. **98**, No. 4, pp 568 (2005).

[93] H. Kjeldsen, J. Phys. B **39**, R325 (2006).

[94] D. Nikolić, T. W. Gorczyca and N. R. Badnell, Phys. Rev. A **79**, 012703 (2009).

[95] W. Eissner, N. Huu Hoa and L. Vo Ky, *ICPEAC 2009: Abstract of Papers*, *Calclulations of Photoionization on* Ti^{3+} (ICPEAC, Kalamazoo, MI, 2009).

[96] I. C. Lyon, B. Peart, K. Dolder and J. B. West, J. Phys. B **20**, 1471 (1987).

[97] J. E. Hansen and P. Quinet, J. Elec. Spec. **79**, 307 (1996).

[98] A. Müller, S. Schippers, A. M. Covington, A. Aguilar, G. Hinojosa, R. A. Phaneuf, M. M. SantAnna, A. S. Schlachter, J. D. Bozek and C. Cisneros, *ICPEAC 2001: Abstracts of Contributed Papers* (Rinton, Princeton, NJ, 2001), P52.

[99] J. B. West, H. Kjeldsen, F. Folkmann and T. Andersen, J. Phys. B **34**, 4035 (2001).

[100] H. Kjeldsen, F. Folkmann, F Innocenti, L. Zuin and J. E. Hansen, J. Phys. B **35**, L375 (2002).

[101] J. B. West, Rad. Phys. and Chem. **70**, 275 (2004).

[102] J. E. Hansen, H. Kjeldsen, F. Folkmann, M. Martins and J. B. West, J. Phys. B **40**, 293 (2007).

[103] J. Berkowitz *Photoabsorption, Photoionization, and Photoelectron Spectroscopy* (Academic Press, New York, 1979).

[104] R. F. Reilman and S. T. Manson, Astrophys. J. Suppl. Ser: **40**, 815 (1979).

[105] R. E. Dietz, E. G. Mc Rae, Y. Yafet and C. W. Caldwell, Phys. Rev. Lett. **33**, 1372 (1974).

[106] L. C. Davis and L. A. Feldkamp, Solid State Commun. **19**, 413 (1976).

[107] S. Schippers *et al*, Nucl. Instrum. Methods Phys. Res. B **205**, 297 (2003).

[108] S. Schippers, S. Kieslich, A. Müller, G. Gwinner, M. Schnell, A. Wolf, M. Bannister, A. Covington and L. B. Zhao, Phys. Rev. A **65**, 042723 (2002).

[109] A. Hibbert and J. E. Hansien, J. Phys. B **32**, 4133 (1999).

[110] A. R. P. Rau and U. Fano. Phys. Rev. **167**, 7 (1968).

APPENDIX A: STRUCTURE OF THE *R*-MATRIX PACKAGE

A.1. Inner region codes

A.1.1. Non-relativistic (LS-coupling) operations

A.1.1.1. STG1

This reads the bound orbitals generated from packages such as CIV3 or AUTOSTRUCTURE, and contained in file "radial". It generates continuum basis orbitals, and evaluates all possible bound-bound, bound-continuum and continuum-continuum integrals that could be required at the next stage of execution.

A.1.1.2. STG2

STG2 performs the N- and (N+1)-electron angular algebra, and creates the N- and (N+1)-electron Hamiltonians. It diagonalizes the N-electron Hamiltonian to regenerate the target eigen-energies (and eigen-vectors) that can be compared to those obtained during bound orbitals generation with CIV3 or AUTOSTUCTURE.

A.1.1.3. STG3

STG3 is also known as STGH, and it performs the diagonalization of (N+1)-electron Hamiltonian. It generates files H.DAT and D0X (with X varying from 0 to n)

A.1.2. Relativistic (Breit-Pauli) operations

The relativistic (Breit-Pauli) operations are switched on in phase 1 and phase 2 (STG1 and STG2). Unlike the non-relativistic operations, the STG2 doesn't perform the diagonalization of the N-electron Hamiltonian, and the CC (close coupling) expansion is forced (expanded) to be the same (in size) as the CI (configuration interaction) expansion. Between STG2 (phase 2) and STG3 (phase 3), we have to run the recoupling code (STGJK or RECUPD); this allows the use of the total angular momentum J. STGJK

recouples the N- and (N+1)-electron Hamiltonians, and diagonalizes the N-electron Hamiltonian to regenerate the target eigen-energies (and eigen-vectors).

A.2. Outer region codes

A.2.1 STGB (BOUND)

STGB reads the file H.DAT file generated by STG3, and calculates bound-state eigen-energies and eigen-vectors for the (N+1)-electron system. It generates file B0X (with X varying from 0 to n).

A.2.2. STGF (FREE)

STGF reads the file H.DAT file generated by STG3, calculates collision strengths at a user supplied set of energies, and writes them to files F0X (with X varying from 0 to n). All input energies are z**2 scaled in the residual charge, if z > 0.

A.2.3. STGBF (BOUND-FREE)

STGBF reads files D0X generated by STG3, B0X by STGB and F0X by STGF, and then calculates photoionization cross sections for transitions from a bound-state to a free-state.

A.2.4. Radiative damping (STGBF0DAMP)

This is a radiation+Auger damped photoionization code, and initial states must be fully contained in the *R*-matrix box. STGBF0DAMP reads files H.DAT and D0X generated by STG3 and B0X by STGB, and calculates photoionization cross sections.

APPENDIX B: Sc^{+2} PHOTOIONIZATION CROSS SECTION CALCULATIONS

INPUT DATA

This appendix shows sample input data for Sc^{+2} photoionization cross section calculations, details of those calculations are given in section 3.1.

B.1. DSTG1

```
S.S.   ScIV target
 &STG1A ISMITN=1 RAD='YES' RELOP='YES' &END
 &STG1B MAXLA=4 MAXLT=5 MAXC=34 MAXE=6 ISMIT(1)=42
 ISMIT(2)=43 ISMIT(3)=50 ISMIT(4)=51 ISMIT(5)=52  &END
```

B.2. DSTG2

```
S.S.  ScIV target
 &STG2A RAD='YES' RELOP='YES'  &END
 &STG2B MAXORB=13 NELC=18 NAST=16 INAST=5 IKEY=1  &END
 1 0 2 0 2 1 3 0 3 1 3 2 4 0 4 1 4 2 4 3 5 0 5 1 5 2
 24
 2 2 6 1 3 0 0 0 0 0 0 0 0
 2 2 6 2 6 3 1 1 1 1 1 1 1
 2 2 6 2 6 0 0 0 0 0 0 0 0   0
 2 2 6 1 6 1 0 0 0 0 0 0 0   0
 2 2 6 2 5 1 0 0 0 0 0 0 0   0
 2 2 6 2 5 0 1 0 0 0 0 0 0   0
 2 2 6 2 5 0 0 1 0 0 0 0 0   0
 ……
 ……
 2 2 6 1 5 2 0 0 0 0 0 0 0   0
 2 2 6 1 5 1 1 0 0 0 0 0 0   0
 1 0 0
 3 1 1
 3 3 1
 1 2 1
 3 2 1
 1 3 1
 3 1 1
 1 1 1
 1 1 1
 3 0 0
 3 2 0
 1 2 0
```

1 1 0
3 1 0
3 2 0
1 2 0
62
2 2 6 1 3 0 0 0 0 0 0 0 0
2 2 6 2 6 4 2 2 2 2 2 2 2
2 2 6 2 6 1 0 0 0 0 0 0 0 -1 1
2 2 6 2 6 0 1 0 0 0 0 0 0 0 1
2 2 6 2 6 0 0 1 0 0 0 0 0 0 1
2 2 6 2 6 0 0 0 1 0 0 0 0 0 1
2 2 6 2 6 0 0 0 0 1 0 0 0 0 1
2 2 6 2 6 0 0 0 0 0 1 0 0 0 1
2 2 6 2 6 0 0 0 0 0 0 1 0 0 1
2 2 6 2 6 0 0 0 0 0 0 0 1 0 1
……
……
2 2 6 2 4 3 0 0 0 0 0 0 0 0 11
2 2 6 2 4 2 1 0 0 0 0 0 0 0 11
2 0 0
47
2 2 6 1 3 0 0 0 0 0 0 0 0
2 2 6 2 6 4 2 2 2 2 2 2 2
2 2 6 2 6 1 0 0 0 0 0 0 0 -1 1
2 2 6 2 6 0 1 0 0 0 0 0 0 0 1
2 2 6 2 6 0 0 1 0 0 0 0 0 0 1
2 2 6 2 6 0 0 0 1 0 0 0 0 0 1
2 2 6 2 6 0 0 0 0 1 0 0 0 0 1
2 2 6 2 6 0 0 0 0 0 1 0 0 0 1
2 2 6 2 6 0 0 0 0 0 0 1 0 0 1
2 2 6 2 6 0 0 0 0 0 0 0 1 0 1
……
……
2 2 6 2 5 2 0 0 0 0 0 0 0 0 11
2 2 6 2 4 3 0 0 0 0 0 0 0 0 11
2 2 6 2 4 2 1 0 0 0 0 0 0 0 11
2 2 0
218
2 2 6 1 3 0 0 0 0 0 0 0 0
2 2 6 2 6 4 2 2 2 2 2 2 2
2 2 6 2 6 1 0 0 0 0 0 0 0 0 1
2 2 6 2 6 0 1 0 0 0 0 0 0 0 1
2 2 6 2 6 0 0 1 0 0 0 0 0 0 1
2 2 6 2 6 0 0 0 1 0 0 0 0 0 1
2 2 6 2 6 0 0 0 0 1 0 0 0 0 1
2 2 6 2 6 0 0 0 0 0 1 0 0 0 1

2 2 6 2 6 0 0 0 0 0 0 1 0 0 1
2 2 6 2 6 0 0 0 0 0 0 0 1 0 1
……
……
2 2 6 2 5 0 0 1 1 0 0 0 0 0 24
2 2 6 2 4 0 0 2 1 0 0 0 0 0 24
2 2 6 2 4 0 0 1 2 0 0 0 0 0 24
2 2 6 2 4 1 0 1 1 0 0 0 0 0 24
2 2 6 2 4 0 1 1 1 0 0 0 0 0 24
2 2 6 2 4 0 0 1 1 1 0 0 0 0 24
2 2 6 2 4 0 0 1 1 0 1 0 0 0 24
2 2 6 2 4 0 0 1 1 0 0 1 0 0 24
2 2 6 2 4 0 0 1 1 0 0 0 1 0 24
2 1 1
218
2 2 6 1 3 0 0 0 0 0 0 0 0
2 2 6 2 6 4 2 2 2 2 2 2 2
2 2 6 2 6 1 0 0 0 0 0 0 0 0 1
2 2 6 2 6 0 1 0 0 0 0 0 0 0 1
2 2 6 2 6 0 0 1 0 0 0 0 0 0 1
2 2 6 2 6 0 0 0 1 0 0 0 0 0 1
2 2 6 2 6 0 0 0 0 1 0 0 0 0 1
2 2 6 2 6 0 0 0 0 0 1 0 0 0 1
2 2 6 2 6 0 0 0 0 0 0 1 0 0 1
2 2 6 2 6 0 0 0 0 0 0 0 1 0 1
……
……
2 2 6 2 5 0 0 1 1 0 0 0 0 0 24
2 2 6 2 4 0 0 2 1 0 0 0 0 0 24
2 2 6 2 4 0 0 1 2 0 0 0 0 0 24
2 2 6 2 4 1 0 1 1 0 0 0 0 0 24
2 2 6 2 4 0 1 1 1 0 0 0 0 0 24
2 2 6 2 4 0 0 1 1 1 0 0 0 0 24
2 2 6 2 4 0 0 1 1 0 1 0 0 0 24
2 2 6 2 4 0 0 1 1 0 0 1 0 0 24
2 2 6 2 4 0 0 1 1 0 0 0 1 0 24
2 2 1
218
2 2 6 1 3 0 0 0 0 0 0 0 0
2 2 6 2 6 4 2 2 2 2 2 2 2
2 2 6 2 6 1 0 0 0 0 0 0 0 0 1
2 2 6 2 6 0 1 0 0 0 0 0 0 0 1
2 2 6 2 6 0 0 1 0 0 0 0 0 0 1
2 2 6 2 6 0 0 0 1 0 0 0 0 0 1
2 2 6 2 6 0 0 0 0 1 0 0 0 0 1
2 2 6 2 6 0 0 0 0 0 1 0 0 0 1

```
 2  2  6  2  6  0  0  0  0  0  0  1  0  0  1
 2  2  6  2  6  0  0  0  0  0  0  0  1  0  1
 ……..
 ……..
 2  2  6  2  5  0  0  1  1  0  0  0  0  0 24
 2  2  6  2  4  0  0  2  1  0  0  0  0  0 24
 2  2  6  2  4  0  0  1  2  0  0  0  0  0 24
 2  2  6  2  4  1  0  1  1  0  0  0  0  0 24
 2  2  6  2  4  0  1  1  1  0  0  0  0  0 24
 2  2  6  2  4  0  0  1  1  1  0  0  0  0 24
 2  2  6  2  4  0  0  1  1  0  1  0  0  0 24
 2  2  6  2  4  0  0  1  1  0  0  1  0  0 24
 2  2  6  2  4  0  0  1  1  0  0  0  1  0 24
2 3 1
```

B.3. DSTGJK

```
S.S. Sc IV TARGET, STGJK
 &STGJA  RAD ='YES'  &END
 &STGJB JNAST=30 IJNAST=7  &END
 0  0      1S
 0  1      3P
 2  1      3P
 4  1      3P
 0  1      3P
 2  1      3P
 4  1      3P
 4  1      3F
 6  1      3F
 8  1      3F
 4  1      1D
 2  1      3D
 4  1      3D
 6  1      3D
 6  1      1F
 2  1      1P
 2  1      1P
 2  0      3S
 2  0      3D
 4  0      3D
 6  0      3D
 2  0      3D
 4  0      3D
 6  0      3D
 4  0      1D
```

```
 4  0      1D
 0  0      3P
 2  0      3P
 4  0      3P
 2  0      1P
1  0
 3  0
 5  0
 1  1
 3  1
 5  1
 7  1
```

B.4. DSTG3

```
S.S.  ScIV target
 &STG3A RAD='YES'  &END
 &STG3B INAST=0 NAST=0  &END
```

B.5. DSTGB

```
&STGB IPRINT=2 IPERT=0 IOPT2=1 IRAD=1  &END
 0 1 0
0.5 5.5 0.025
 0 3 0
0.5 5.5 0.025
 0 5 0
0.5 5.5 0.025
 -1 -1 –1
```

B.6. DSTGF

```
&STGF IQDT=0 IMODE=0 IMESH=1 PERT='NO' LRGLAM=7 IBIGE=0
 IPRINT=3 IRAD=1 IOPT1=1 IRDEC=1 IBETA=1  &END
 &MESH1 MXE=10000 E0=0.0000 EINCR=0.00004  &END
```

B.7. DPREBF

```
&PREBF IPRINT=1 IBUT=1  &END
```

B.8. DSTGBF

```
&STGBF IPRINT=3 IBUT=1  &END
```

B.9. DSTGBF0DAMP

```
&STGF IQDT=0 IMODE=0 IMESH=1 PERT='NO' LRGLAM=5 IBIGE=0
 IPRINT=3 IOPT1=1 NTYP1=1 NTYP2I=1 NTYP2OR=1 NTYP2OF=1
 NMIN=6 IPHOTO=30 NPISYM=3 NPIEB=1   &END
 &MESH1  MXE=10000 E0=0.0000 EINCR=0.00004  &END
```